Nanocomposite Based Infrared Photothermoelectric Detectors

by

Jiaqi Wang

A thesis

presented to the University of Waterloo

in fulfillment of the

thesis requirement for the degree of

Doctor of Philosophy

in

Systems Design Engineering (Nanotechnology)

Waterloo, Ontario, Canada, 2023

Examining Committee Membership

The following served on the Examining Committee for this thesis. The decision of the Examining Committee is by majority vote.

External Examiner:	Dr. Winnie N. Ye Professor, Department of Electronics Carleton University
Supervisor:	Dr. John T.W. Yeow Professor, Systems Design Engineering University of Waterloo
Internal Member:	Dr. Nima Maftoon Assistant professor, Systems Design Engineering University of Waterloo
Internal-external Member:	Dr. William Wong Professor, Electrical and Computer Engineering University of Waterloo
Internal-external Member:	Dr. Fue-Sang Lien Professor, Mechanical and Mechatronics Engineering University of Waterloo

Author's Declaration

This thesis consists of material all of which I authored or co-authored: see Statement of Contributions included in the thesis. This is a true copy of the thesis, including any required final revisions, as accepted by my examiners.

I understand that my thesis may be made electronically available to the public.

Statement of Contributions

I list the publications where I am the first author or the co-author. As the first author, I am responsible for all the device design, fabrication, characterization, data analysis, and manuscript writing. The co-authors have provided help with polishing the papers and providing revision suggestions.

First author:

1. Jiaqi Wang et al., Two-dimensional materials applied for room-temperature thermoelectric photodetectors, 2020, *Materials Research Express*, 7, 112001.
   (This work is presented in Chapter 2.)
2. Jiaqi Wang et al., Capillary-assisted self-assembly of carbon nanotubes for the self-powered photothermoelectric detector, 2023, accepted by *Advanced Materials Technologies.*
   (This work is presented in Chapter 3.)
3. Jiaqi Wang et al., Design of room-temperature infrared photothermoelectric detectors based on CNT/PEDOT:PSS composites, 2022, *Journal of Materials Chemistry C*, 10, 15105-15113.
   (This work is presented in Chapter 4.)
4. Jiaqi Wang et al., An infrared photothermoelectric detector enabled by MXene and PEDOT:PSS composite for non-contact fingertip tracking, 2023, *Microsystems & Nanoengineering*, 9, 21.
   (This work is presented in Chapter 5.)
5. Jiaqi Wang et al., System design of large-area vertical photothermoelectric detector based on carbon nanotube forest with MXene electrodes, 2023, *Nanoscale Advances*, 5, 1133-1140.
   (This work is presented in Chapter 6.)

Co-author:

1. Zhemiao Xie et al., Flexible multi-element photothermoelectric detectors based on spray-coated graphene/polyethylenimine composite for non-destructive testing, 2023, *ACS Applied Materials & Interfaces*, 15, 4, 5921-5930.
2. Guanxuan Lu et al., Carbon-based THz microstrip antenna design: A Review, 2022, *IEEE Open Journal of Nanotechnology*, 3, 15-23.
3. Zhemiao Xie et al., Doped polyaniline/graphene composites for photothermoelectric detectors, 2022, *ACS Applied Nano Materials*, 5, 6, 7967–7973.

Abstract

In the last decade, photothermoelectric (PTE) detectors that combine photothermal and thermoelectric conversion have been demonstrated for infrared and terahertz tracking. They are advantageous in terms of facile fabrication, simple structures, room-temperature operation and self-powering capability. However, some challenges remain to be addressed, including low response performance, large-area fabrication and quick degradation. Based on the aforementioned challenges, this thesis targets optimizing current detectors and exploring new detector structures, which eventually enhance the PTE response and create possibilities for scalable manufacturing and mass production.

In this thesis, we mainly develop four innovative PTE detectors. Firstly, we propose a new PTE structure using a capillary-assisted carbon nanotube forest (CNTF). By creating different CNT growth conditions, two regions of CNTF are grown and connected by the introduction of dimethyl sulfoxide. The detectors show a quick and sensitive infrared response. Secondly, we propose flexible and Si-based PTE detectors using CNT/poly(3,4-ethylenedioxythiophene) polystyrene sulfonate (PEDOT:PSS) composite. Both detectors show quick mid-infrared responses and demonstrate non-destructive imaging tracking capacities. Thirdly, we create a vertical PTE detector using MXene/PEDOT:PSS composite and integrate the metamaterials into PTE detectors. The applications of non-contact fingertip tracking are achieved. Finally, the PTE detectors using CNTF active layer with MXene electrodes are fabricated and packed with PTFE, which enhances the stability and also indicates the non-destructive testing capacities.

Overall, this thesis proposes a systematic method of designing infrared PTE detectors mainly based on CNTs, MXene and related composites, which also provides guidelines and methodology

for developing other low-dimensional material/composite based PTE detectors. Furthermore, these detectors also pave the way toward wearable smart sensors for industrial applications.

Acknowledgements

To my best respect for my dear professor, Dr. John Yeow. He teaches me how to be a real man and how to become a better person. He is the light of my life and leads me to explore the value of life.

Professor John Yeow offers me the opportunity to enter this lab and leads me to the world of the microscopic/nanoscopic world. He is also open-minded and broadens my horizons. He provides tremendous financial support, which makes me access to quantum nanofabrication and leads me to see the world of chips and sensors. Previously, I had almost no experience with typical engineering projects or designing the whole experiment individually. To enrich my own engineering experiences, I did lots of related experiments like measurement setup and membrane synthesis initially. With lots of failure cases, I accumulated experience in membrane and device fabrication. Then I started to design some complicated experimental processes. When it was my first time seeing the orange room, it was very magical and the equipment attracted me so much. That border in Quantum-Nano Centre was like a “fortress besieged”. When I stood outside the cleanroom, I was wondering what the internal people were DOIng and how they fabricated the chips. When someday comes, could I fabricate the chips like those? The answer is yes. I got lithography, deposition, etching, wet bench, and packaging training, and worked for many hours. During the period of fabricating chips, I also learned time management, pressure management, and emotional control. Sometimes, even if one minimal error occurs, it would influence the whole process. I have to admit that I may be a careless man before I entered the cleanroom. However, it cannot be allowed because one error in one project may cause a detrimental result. As time passes by, more and more projects and personal items made me grow and see the world, but I appreciate and hug the world. Previously, I thought I did not have the gift of understanding questions, and

my professor said that everything could be trained. I became more confident than before and started to change myself. Nothing is impossible, except that you give up yourself. When my dear professor John hosted a presentation at Quantum Nano Center, I went and asked whether I could be his student. At that time, I might not be confident and always emotional. John encouraged me a lot and said that if I worked hard, I could go further. From that time, I became confident and know that I must focus on something and have a very good command of something. Now I think maybe that's the fabrication and how I think. Sometimes, fab work is tiring and makes me feel struggled and especially when I meet some issues. They are challenging to track if you do not do a test chip. However, I love these things. Exhausted and happy! Maybe in the future, I may work on other projects and other work, but the trained strategies and base strategy from these experiences will make me benefit forever.

Sometimes during my Ph.D. life, I feel sad and struggled when first refused by the journal. I feel disappointed that one good point of yours cannot be understood and recognized. Sometimes I can't think about one good idea even for a long time. After lots and lots of paper reading, the threshold reaches and one comprehensive point can be designed. At that time, I just could see the light coming and just felt a little happy. This is just one microcosm of life. With time passing by, John teaches me to keep still even if anything big happens. Just treat life like normal and everything good will come. I still believe that learning is the only way to change life for most normal people like me.

For one project, if there is no teamwork and discussion, the result must be tiny and minimal. Therefore, I would like to thank my lab buddies. I am not a talented student, but my lab buddies never blame me and are always kind and patient. Those warm-heart moments will encourage me to jump a large step to another life milestone.

Lastly, and most importantly, I would like to show my deepest gratitude to my family members for all the financial and mental support from my heart.

Jiaqi

Table of Contents

List of Figures

List of Tables

List of Abbreviations

BP	Black phosphorus
CW	Continuous wave
CVD	Chemical vapour deposition
CNT	Carbon nanotube
CNTF	Carbon nanotube forest
MWCNT	Multi-walled carbon nanotube
SWCNT	Single-walled carbon nanotube
HCNT	Helical carbon nanotube
PEDOT:PSS	Poly(3,4-ethylenedioxythiophene) polystyrene sulfonate
DMSO	Dimethyl sulfoxide
PVA	Poly (vinyl alcohol)
PTE	Photothermoelectric
IR	Infrared
NIR	Near-infrared radiation
MIR	Mid-infrared radiation
FIR	Far-infrared radiation
MWIR	Mid wavelength infrared
LWIR	Mid wavelength infrared
PTFE	Polytetrafluoroethylene
MCT	Mercury cadmium telluride
PdS	Palladium sulfide
QWIP/QWID	Quantum-well/dot infrared photodetector
SNR	Signal-to-noise
NDT	Non-destructive tracking
TCR	Temperature coefficient of resistance
RMS	Root mean square
NEP	Noise equivalent power
SNR	Signal-to-noise
SRR	Split-ring resonator

THz	Terahertz
1-/2-/3-D	One-/Two-/Three-dimensional
EBL	Electron beam lithography
SRD	Spin rinse dryer
HMDS	Hexamethyldisilazane
PPy	Polypyrrole
IoT	Internet of Things
PR	Photoresist
PL	Photolithography
GaAs	Gallium arsenide
InSb	Indium antimonide
CdS	Cadmium sulfide
EMS	Electromagnetic shielding
CMOS	Complementary metal-oxide-semiconductor

Chapter 1 Introduction

1.1.Motivation

Mid-infrared (MIR) detection has been applied for numerous applications, such as medical tracking, gas sensors, security imaging, and the Internet of Things (IoTs)[1]–[3]. Nowadays, industrial MIR detectors are mainly based on the mercury cadmium telluride (MCT, HgCdTe), palladium sulfide (PdS), and III-V quantum-well/dot infrared photodetector(QWIP/QWID)[4], [5]. However, MCT and PdS detectors suffer from the high toxicity of heavy metals, and QWIP/QWID detectors require cryogenic working conditions[6]. Although these detectors can show a respectable response in IR detection, other issues, such as high-cost fabrication and incompatible fabrication with the complementary metal-oxide-semiconductor (CMOS) technique, also hinder their further applications. Thus, the novel MIR detectors are urgent.

Photothermoelectric (PTE) detectors are a powerful tool for MIR detection beyond the limitations of bandgap[7], [8]. PTE detectors can be also designed for a simple configuration such as the asymmetric electrodes and operate at room temperature with zero bias and low power consumption[9]. Additionally, PTE detectors, dominated by Johnson-Nyquist thermal noise, suppress the shot noise and 1/f noise of detectors[10], [11]. In contrast, common IR detectors suffer from a low signal-to-noise ratio (SNR) effect and the presence of a dark current.

PTE detectors based on low-dimensional materials offer advantageous thermodynamics and optoelectrical properties[12]–[15]. Many nanomaterials have been explored for PTE detectors in the IR regime. PTE detectors based on low-dimensional materials offer advantageous thermodynamics and optoelectrical properties[12]–[15]. Many nanomaterials have been explored for PTE detectors in the IR regime. The PTE detector based on single-layer graphene achieves a

responsivity of over 10 V/W in the terahertz regime[84]. However, the fabrication of single-layer graphene is complicated, the absorption is relatively low, and the cost is high[8]. Although microporous graphene enhances the inherently poor IR absorption of single-layer graphene, their related PTE detectors show a 4 mV/W responsivity. However, it is challenging to pattern the array of microporous graphene, which limits further industrial applications[16]. Graphene fibres are also used in MIR optical communications, but the PTE detector based on them requires high bias up to 6 V and cannot achieve a self-powered response[17]. Black phosphorus (BP) is one promising PTE material with high carrier mobility, but it suffers from unstable ambient problems. Its current fabrication process depends on exfoliation, and the device is generally fabricated in one single BP flake[18], which makes it challenging to achieve large-area production.

To solve or mitigate the abovementioned issues, the main objective of this dissertation is to develop multiple IR PTE detectors based on novel low-dimensional nanomaterials and related nanocomposites. The detectors are dedicated to achieving a self-powered, sensitive, fast, and stable photoresponse and verify practical applications such as human radiation tracking and non-destructive tracking (NDT). Furthermore, some optimization strategies and prospects of IR PTE detectors will also be demonstrated. The ultimate objective is to provide a systematic methodology for the design, fabrication, characterization, and response optimization of PTE detectors.

1.2.Thesis outline

The thesis is organized in a format as described in the following paragraph.

Chapter 2 introduces the related background knowledge of infrared thermal detectors firstly. The figures of merit of PTE detectors will be also presented. Next, some basic structures will be presented according to illumination conditions and device configuration. Finally, we will present

the low-dimensional materials and engineering influential factors applied to PTE detectors.

Chapter 3 proposes the self-powered PTE detector based on the capillary-induced CNT forest (CNTF). This detector design utilizes three-dimensional space and achieves a quick response time of 40 ms.

Chapter 4 proposes and characterizes two designs of carbon nanotube/poly(3,4-ethylenedioxythiophene) polystyrene sulfonate (CNT/PEDOT:PSS) PTE detectors applied for human radiation tracking and the NDT imaging of crossing pattern.

Chapter 5 proposes the MIR PTE detectors relying on the MXene/PEDOT:PSS composite. Different engineering strategies of PTE detectors are demonstrated and the real-time fingertip tracking is verified.

Chapter 6 proposes the vertical PTE detector utilizing low-dimensional CNTF and MXenes. The CNTF act as the active layer and MXenes act as the top electrode and IR absorber.

Chapter 7 concludes the contributions and offers the prospects and optimization strategies of the infrared PTE detectors.

Chapter 2 Background

As seen in **Figure 2-1**, the IR regime covers from 10^{12} to 10^{14} Hz, which is longer than the visible regime, but shorter than millimetre waves[19]. According to different standards, the wavelength of mid-/far- infrared (MIR/FIR) regimes is usually defined as a wavelength longer than 3 μm. Currently, IR detectors have been extensively investigated across various fields, like astronomy, military, and industrial areas[20]–[22]. In this chapter, we will introduce the related background of infrared thermal detectors, including Golay cell, bolometer and pyroelectric detectors, and PTE detectors. Typically, we will present PTE detectors in detail, including the mechanism, figures of merit, basic structures, materials, and engineering influential factors.

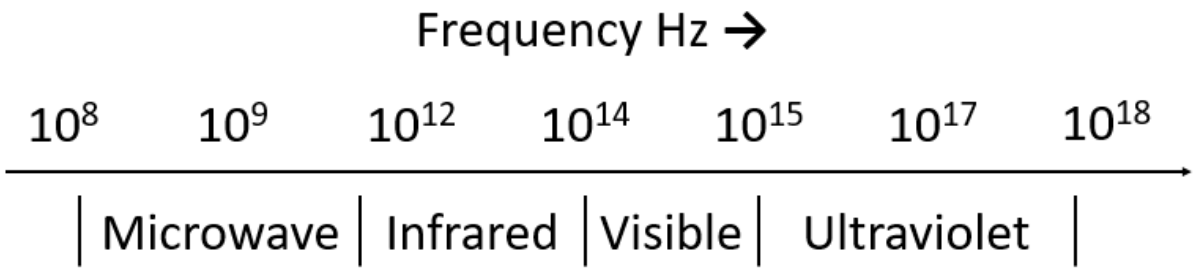

Figure 2-1. The electromagnetic spectrum.

2.1. Infrared thermal detectors

2.1.1. Golay cell

The basic structure of the pneumatic Golay cell is illustrated in **Figure 2-2**[23]. When a typical gas is exposed to infrared radiation, it absorbs the radiation and converts it into thermal energy. This causes the gas to heat up and expand, leading to the deformation of the membrane. An optical read-out system tracks this deformation, allowing the Golay cell to detect infrared radiation with

high sensitivity and broad bandwidth. However, there are still challenges that need to be addressed, such as degradation issues with the membrane and the potential for gas leaks. The Golay cell also requires a gas chamber and optical read-out system, which can make it more complex and less portable. Moreover, the response time of the Golay cell is significantly influenced by the type of gas used.

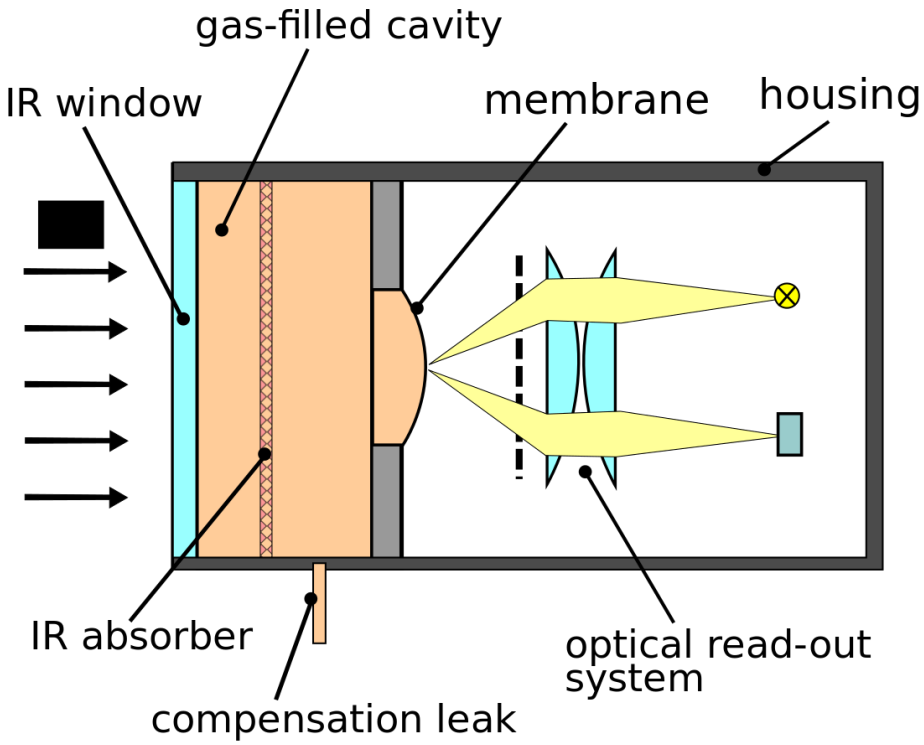

Figure 2-2. The schematic illustration of Golay cell[23].

2.1.2. Bolometer

The fundamental design of the bolometer is depicted in **Figure 2-3**. When infrared radiation is incident on the active material, it heats up and causes a significant change in resistance. By measuring the resistance difference, the absorbed radiation can be quantified. To ensure a high-

performance bolometer, the active material usually needs a high-temperature coefficient of resistance (TCR), which can be expressed as $TCR = \frac{1}{R}\frac{dR}{dT}$, where R is the resistance and T is the temperature[24],[25]. Typically, the responsivity of a bolometer can be described as $R_V = \frac{iR\alpha\eta}{G\sqrt{1+\omega^2\tau^2}}$, where α is the TCR value, η is the absorption coefficient, G characterizes the thermal conductance to the substrate, ω is the modulated frequency. τ is the response time[26]. Thus, achieving a high-performance bolometer necessitates both a material with high TCR and reduced thermal loss to the substrate. Although bolometers are relatively low power-consuming, stable, and dependable infrared thermal detectors, they have a longer response time and are insensitive to the position of illumination.

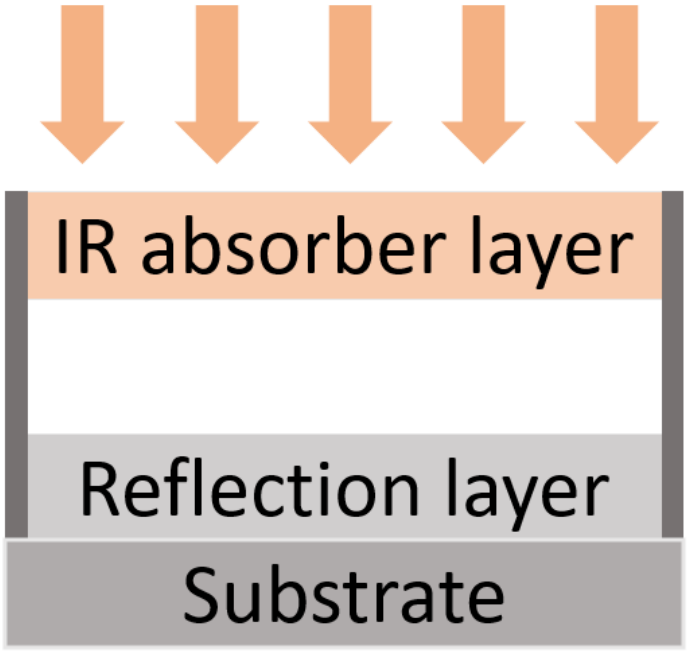

Figure 2-3. The schematic illustration of the bolometer.

2.1.3. Pyroelectric detectors

The basic layout of the pyroelectric detector is illustrated in **Figure 2-4**[27]. When it is heated by the radiation incident on the detector, the pyroelectric material undergoes a polarized structural transformation, which leads to the voltage difference between the top electrode and the bottom electrode. Pyroelectric detectors typically have simple structures, making them cost-effective since there is no need for complex measurement setups or optoelectrical components integrated into the detector. However, the effectiveness of pyroelectric detectors is heavily reliant on the quality of pyroelectric materials, and as a result, their performance can be limited by the drawbacks of these materials, such as the humidity influence and mechanical vibration[28].

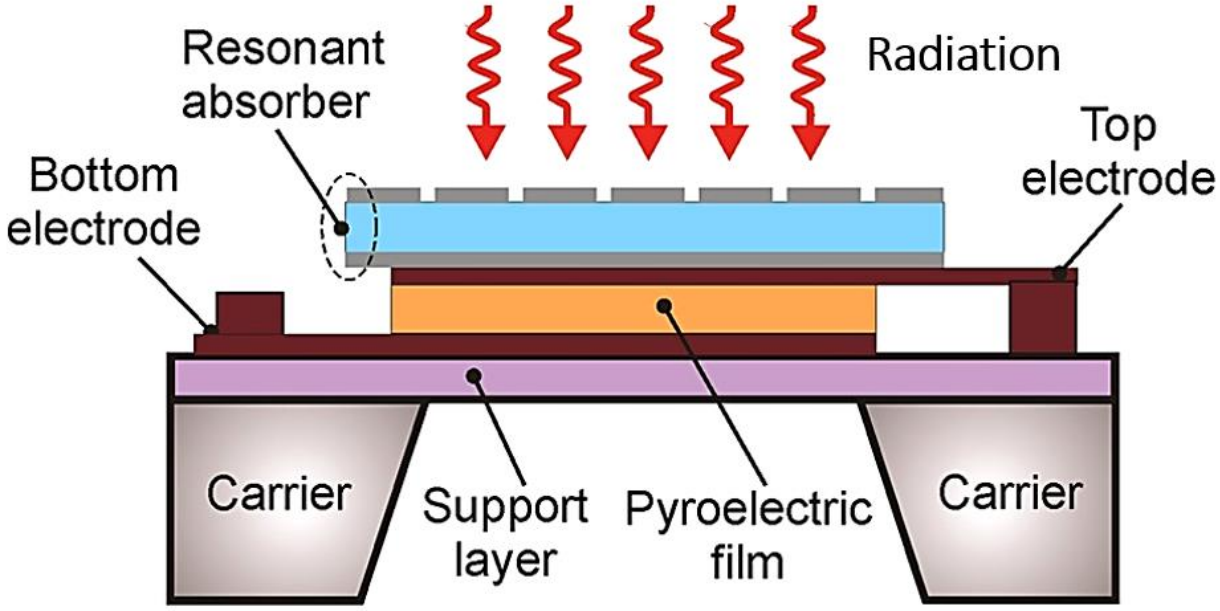

Figure 2-4. The schematic illustration of the pyroelectric detector[27].

2.1.4. PTE detectors

The PTE mechanism is usually divided into photothermal conversion and thermoelectric conversion. Photothermal conversion generally means that the light and matter interact with the molecular thermal vibration, such as semiconducting nonradiative transitions and the metallic

localized plasmonic oscillation[29]. Thermoelectric conversion refers to the generation of an electrical field due to the flow of electrons resulting from a temperature gradient.

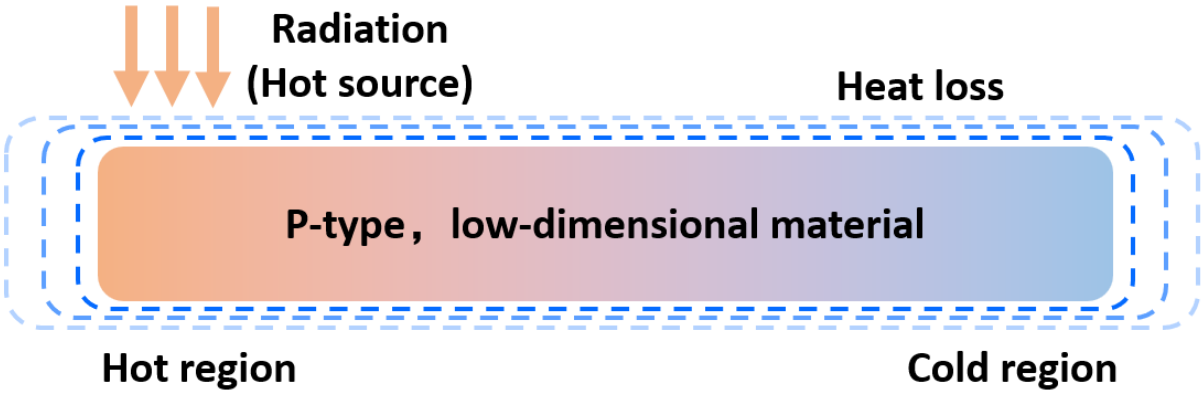

Figure 2-5. The schematic illustration of PTE mechanism.

The schematic illustration of the PTE mechanism is shown in **Figure 2-5**. In detail, when the radiation illuminates one side of P-type or N-type low-dimensional material, the temperature of both electrons and lattice will increase. As the thermal conductivity of electrons is far smaller than that of lattice, the temperature gradient of electrons is created[30]. The electrons will flow from the hot region to the cold region. The PTE voltage ΔU will be described using the equation of $\Delta U = -S \times \Delta T$, where the S means the Seebeck coefficient and ΔT means the temperature difference. Seebeck coefficient can the described as $S = \frac{8L}{h^2} m^* T (\frac{\pi}{3n})^{\frac{2}{3}}$, where L is Lorentz number, h is Plank number, m^* is the effective mass of the carrier, T is the temperature, and n is the carrier concentration[31]. The temperature difference can be described as $\Delta T = \frac{Q_{Heat} - Q_{Loss}}{C \cdot m}$, where Q_{Heat} is part of the absorbed energy to heat the device, Q_{Loss} is the thermal loss to the surroundings, C is the specific heat capacity, and m is the mass[11].

To design high-performance PTE detectors, the materials need high photothermal conversion. Choosing materials with high infrared absorption and reducing the thermal loss dissipated to the

surroundings are two viable methods. Also, they need excellent thermoelectric properties. The overall efficiency of thermoelectric materials can be characterized by the dimensionless figure of merit, $ZT = \frac{S^2\sigma T}{k} = \frac{S^2\sigma T}{k_e+k_l}$, where σ is the electrical conductivity, k is the thermal conductivity, k_e is the electronic thermal conductivity and $k_l$is the lattice thermal conductivity[32]. One viable strategy to increase the Seebeck coefficient is to utilize the electron-phonon coupling-induced phonon drag effect[33]. To achieve a higher ZT value, materials are expected to show a high Seebeck coefficient, a large electrical conductivity, and a low thermal conductivity to obtain a sufficient temperature gradient. Currently, adjusting the k_e and k_l is a feasible method for reducing thermal conductivity[34]. While the commonly used materials in thermoelectric detectors may have a relatively high ZT value, most of them have a relatively low photothermal conversion. Additionally, these detectors require additional voltages to function properly. Some strategies are improving Seebeck coefficients of nanostructures such as the energy filtering effect, the semimetal-semiconductor transition, and the carrier-pocket engineering[35]–[37].

2.2. Figures of merit of PTE detectors

2.2.1. Responsivity

The responsivity of an infrared detector is defined as the root mean square value of the rudimental component of the electrical signal of the detector to the root mean square (RMS) value of the basic component of the input radiation power, $R_V = \frac{V}{P_{in}}\ or\ R_I = \frac{I}{P_{in}}$, where R_V is responsivity, V is voltage, I is current, and P_{in} is absorbed power. The units of responsivity are V/W or A/W.

2.2.2. Noise

Noise means the undesired disturbances that reduce the received signal in the communication system. It plays an important role in evaluating the performance of an infrared thermal detector.

PTE detectors can work without any bias and thus the device noise mainly results from the thermal noise. The thermal noise or Johnson-Nyquist noise is the noise existing in the electrical circuit because of the thermal agitation of the carriers. The thermal noise level is expressed as, $V_n = \sqrt{4k_BTR\Delta f}$, where k_B is the Boltzmann constant, T is the temperature of the electronic device, R is the resistance of the whole circuit, and $\triangle f$ is the frequency bandwidth.

2.2.3. Detectivity

The detectivity of PTE detectors means the ability to detect the photon signal from the noise and can be defined $D^* = \frac{R_V\sqrt{A}}{V_n}$, where R_V is the responsivity, A is the active area, and V_n is the thermal noise.

2.2.4. Noise equivalent power

The noise equivalent power (NEP) can be defined as the illuminated incident power on the detector generating a signal output equal to the RMS noise output or the signal level where signal-to-noise (SNR) is one[1]. It can be expressed as the reciprocal of detectivity D^*, $NEP = \frac{1}{D^*}$, where the specific detectivity demonstrates the ability to detect the photon from the noise[1].

2.2.5. Response time

Response time is a key parameter that indicates the duration of the change of the detector's output signal with the imposed infrared illumination. Generally, it is defined as the time taken to rise from 10% to 90% of the final value.

Overall, a high-performance PTE detector should exhibit a significant responsivity, detectivity, a small NEP, along with a short response time.

2.3. Structural design of PTE detectors

The design concept for PTE detectors is typically inspired by thermoelectric structures and materials. Furthermore, the configuration of PTE detectors varies based on specific design requirements. Presently, the primary configurations can be categorized into asymmetric electrodes, localized illumination on the electrode-active layer interface, localized illumination on the P-N junction, and vertical structures.

2.3.1. Asymmetric electrodes

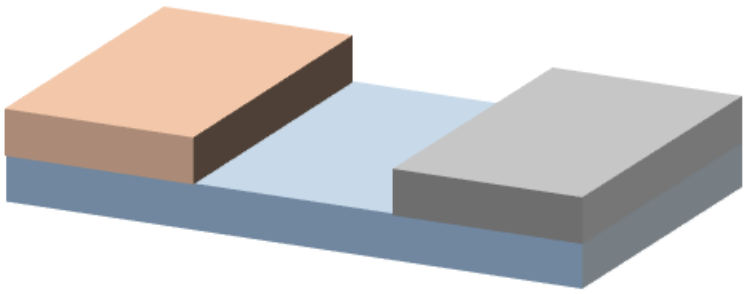

Figure 2-6. The schematic illustration of asymmetric electrode structure**.**

The asymmetric electrode structure is relatively simple, consisting of one active layer and two asymmetric electrodes (as depicted in **Figure 2-6**). Typically, the electrodes are composed of metal, such as Al, Au, and Ti, and can be various shapes, such as rectangular or triangular. With appropriate parameter designs, the electrodes can also function as antennas or metamaterials, such as bow-tie antennas and split-ring resonators (SRRs)[38], [39]. The active layer possesses excellent photothermal conversion ability and high thermoelectric conversion efficiency.

2.3.2. PTE junction

The P-N junction configuration typically consists of two electrodes and the P-N junction, which is

the central component (**Figure 2-7**). When localized illumination is directed onto the P-N junction, a notable photovoltage can be measured. The benefit of the P-N junction configuration is that it can generate a significantly larger difference in the Seebeck coefficient, thereby enhancing the photoresponse according to the relevant equation, $\Delta U = -(S_P - S_N)\Delta T$, where S_P is the Seebeck coefficient of P-type material, and S_N is the Seebeck coefficient of N-type material[40].

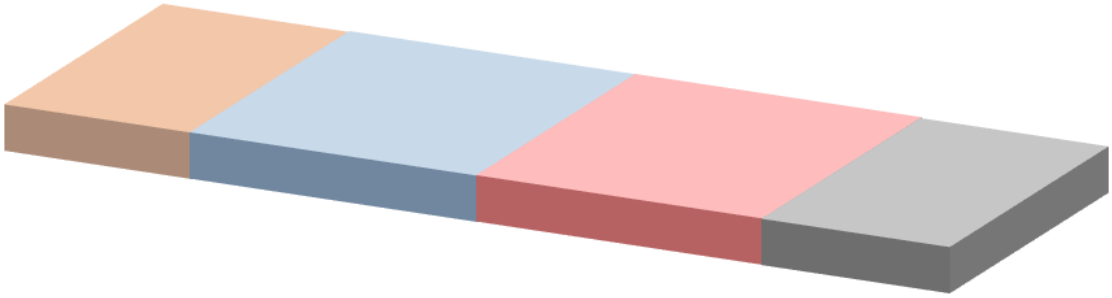

Figure 2-7. The schematic fabrication process of the PTE detector based on the P-N junction.

2.3.3. Vertical structure

The proposed sandwich configuration consists of two electrode layers and one middle active layer (**Figure 2-8**).

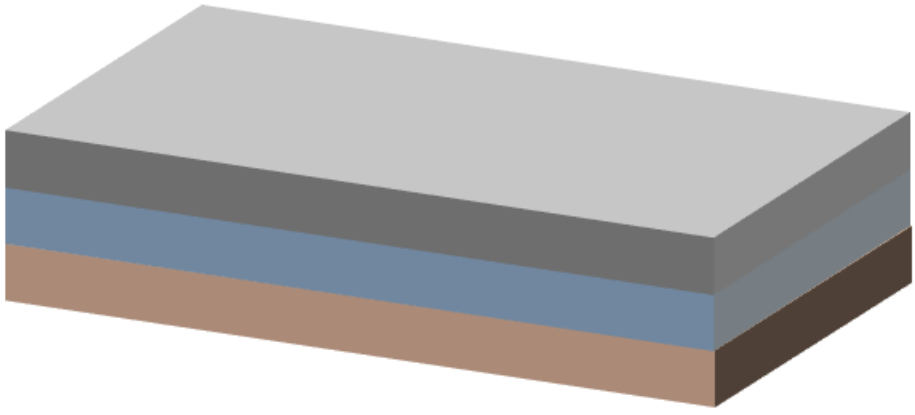

Figure 2-8. The schematic of the vertical PTE detector.

Differently, the top electrode layer can be patterned and designed as different structures to enhance light absorption. In comparison, the patterned structures show a higher detectivity than non-patterned structures. Additionally, CNTs can be designed for effective alignment to improve the polarization of electromagnetic radiation. While the P-N junction structure can also govern the alignment direction of CNTs, it requires an additional doping process. Moreover, in this structure, it is relatively easy to regulate the membrane thickness or the height of the CNTF.

2.3.4. Localized illumination on the electrode-active layer interface

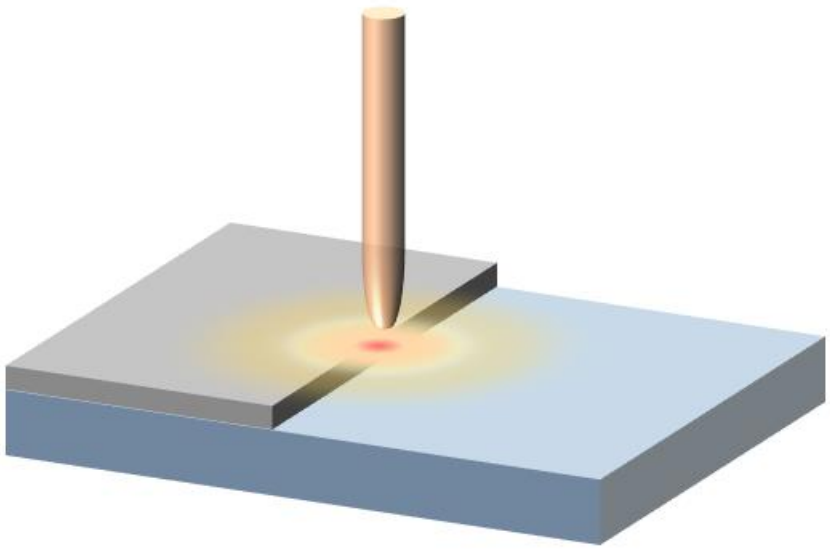

Figure 2-9. The schematic illustration of localized illumination on the interface between electrodes and the active layer.

In this configuration, the PTE mechanism occurs in the interface between metal electrodes and the active layer (**Figure 2-9**). For example, in the CNT film-Au electrodes parallel configuration, the PTE voltage can be expressed as, $V = |S_{CNT} - S_{Com}| \times \Delta T$, and $S_{Com} = \frac{\sigma_{CNT} t_{CNT} S_{CNT} + \sigma_{Metal} t_{Metal} S_{Metal}}{\sigma_{CNT} t_{CNT} + \sigma_{Metal} t_{Metal}}$, where S_{CNT}, S_{Com}, σ_{CNT},

t_{CNT}, σ_{Metal} and t_{Metal} represent the Seebeck coefficient of CNT film, the metal-CNT composite film, the conductivity and thickness of CNT film, and the conductivity and thickness of the metal electrode. When the thickness of the CNT film is far larger than that of the metal electrode, the S_{CNT} and S_{Com} have similar values, which limits the photovoltage[41]. Therefore, the current improvement of this configuration is to use a series structure.

2.4. Active layer of low-dimensional material in PTE detectors

To date, different dimensions and characteristics of PTE materials have been verified, such as one-/two-/three-dimensional nanomaterials and topological quantum materials[7], [18], [38], [42]–[55]. In this dissertation, we only discuss the CNT and MXene materials that are tightly related to my research.

2.4.1. CNT

When it refers to CNT-based PTE detectors, three types of CNTs are usually considered, including single-walled CNT (SWCNT), MWCNT, and helical CNTs (HCNT). These types have demonstrated excellent conductivity, thermal stability[56]–[58], and infrared absorption[59], [60], which are directly or indirectly related to their chirality, dimension and length[61], [62]. Currently, the related synthesis and growth of CNTs mainly come from the chemical vapour deposition (CVD) method or solution methods.

For the mainstream CVD-produced CNTs, the inherent mobility is relatively higher compared with solution-processed CNTs[63]. There are various factors that need to be taken into consideration during the synthesis of a material, including the precursor used, the temperature at which the material is synthesized, the buffer layer, and the catalyst layer. The popular precursor for growing CNTs is ethanol, which can avoid amorphous carbon[64]. The growth temperature is

usually over 600 °C. According to various back-end requirements, different temperatures will be selectively adopted to control the growth of SWCNT or MWCNT. Generally, the growth temperature of SWCNT is usually higher than that of MWCNT. The buffer layer (diffusion barrier layer) can improve the interaction between the substrate and the catalyst layer, and stop the diffusion of catalyst materials into the substrate at high temperatures. Many materials of the buffer layer have been explored, including Cr, SiO_2, Al, Al_2O_3, TiO_2, and TiN[65]. The direct deposition of the catalyst layer on the Si substrate is proved to be a negative growth method, which may produce the silicide that damages the catalyst materials[66]. It will cause changes in the CNT growth rate and growth efficiency. With high melting temperatures and low vaporation pressure, Ni, Co, and Fe are usually selected as catalyst materials, which can help carbon diffuse. For the catalyst layer, the existence of oxygen atoms may optimize the CNT growth because they can limit the agglomeration of small particles[67]. For the Fe catalyst layer, the pressure does not make sense for CNT growth, but a more uniform and dense catalyst layer helps the CNT growth[67]. The maintenance of small sizes can effectively enhance the catalyst quality and activity. Zhang et al. investigate the self-powered CNT-based PTE detectors, which achieve broadband MIR/FIR detection with a peak detectivity of 2.3×10^9 Jones at 4.3 terahertz (THz)[68]. With the introduction of CVD-grown vertical CNTs, the PTE detectors show high infrared absorption, micro-level channel control, and broadband illustration compatibility. Unfortunately, the detector still shows a relatively poor photoresponse and low energy conversion efficiency. He et al. used CVD to produce SWCNTs and transfer them to the substrate and form a horizontal SWCNT array[40]. They investigated the polarization relationship between radiation and horizontal SWCNTs based on a PTE junction structure in the infrared regime. They proved that the parallel polarization of light and the long axis of SWCNTs can show a better PTE response than vertical polarization. This

CNT PTE junction could finally achieve a response time of 80 μs and a responsivity of 1 V/W. Furthermore, the CVD-grown CNT PTE detectors could be accurately quantified and pave the way toward carbon-based optoelectrical applications.

The PTE effect of individual CNTs or pure CNT films has been reported in the last decade. Initially, the scanning photocurrent experiments found that the induced local heating in the asymmetric electrode structure cannot be explained by the photovoltaic theory in the visible regime and demonstrative PTE experiments were performed and verified, such as the illustration position dependency[69]–[71]. Realizing that the PTE detector could skip the bandgap limitation, infrared and terahertz research based on the room-temperature PTE mechanism is emerging. In 2016, Suzuki et al. investigated a passive THz camera using a single-pixel CNT film and CNT linear array[72]. In this experiment, engineering strategies of PTE asymmetric electrode structure were also investigated, such as the thickness and types of metal materials as well as the thickness of vacuum-filtered CNT films. The NEP at 0.14 THz could reach 8.4 $nWHz^{-0.5}$. A finger PTE imaging pattern of 15 cm×18 cm was observed, which lay the foundation for future medical and NDT applications. Using the same structure, the channel length and film thickness were simulated and proved[73]. The illumination penetration through the electrodes would reduce the PTE THz response and eventual imaging resolution because of the undesired thermal diffusion. Later, different Seebeck coefficients of vacuum-filtered suspended MWCNT/SWCNT films are investigated[74]. By tuning the fermi level of CNT films, the semiconducting or metal properties could be well controlled and the PTE response can be effectively enhanced. In 2021, the 2-D suspended CNT array film using the vacuum-filtered method was proven effective for PTE detectors. The advantage of this design was that this flexible device patch design could be adjusted according to the shape and size of detected objects. Li et al. studied the THz coupling direction of the metal electrode and CNT film,

and indicated that the coupling effect of the series is better than that of the parallel[41]. With the series structure, a flexible CNT film with polyimide support was also proven to pattern 3-D PTE imaging. After further optimizing the relationship between THz radiation and physical factors of CNT film, a series of multi-element CNT films combining vacuum filtration and laser ablation methods has verified the first THz spectroscopy[75], [76], where ambroxol hydrochloride and tranexamic acid indicated a specific absorption spectrum separately.

Many solution-processed CNT and polymer composites for PTE detectors have been investigated from visible to THz spectrum in the last five years[13], [77]–[79]. For the PTE mechanism using composite, it may be a trade-off method, i.e. matrix or filler only can provide excellent either photothermal or thermoelectric properties, and the combination of them is expected to achieve a neutralized or boosting PTE response. Generally, the composite consists of a polymer matrix and CNT fillers. The polymer matrix mainly provides a mechanical support network for conducting fillers and helps create some phonon scattering sites[77], [78]. The main role of CNT fillers is to offer excellent photon absorption and thermoelectric properties. In 2018, Zhang et al. reported the first CNT/polymer composite for stable and flexible infrared PTE detectors[13], which showed a maximum responsivity of 0.1 V/W and detectivity of 4.9×10^{6} Jones in the MIR regime. Although the introduction of poly (vinyl alcohol) (PVA) slightly improved the composite thermoelectric properties and mechanical properties, the high composite resistance of 81 kΩ and relatively long channel limited the PTE response. This work demonstrated the potential of PTE detectors for wearable sensors. In 2021, Jin et al. mainly investigated the PTE detectors based on polypyrrole(PPy)/HCNTs[29]. HCNTs showed a particular spiral structure and the PTE mechanism might induce the hot carriers through the tube and produce an enhanced electromagnetic absorber effect. Also, HCNTs benefited from the local arrangement of PPy, followed by electrical

enhancement. The ZT value also reached 4×10^{-3}. Their results also verified that the composite shows remarkable near-infrared (NIR) absorption and thermoelectric properties, especially a low thermal conductivity. Ultimately, they also incorporated the PTE detectors for the Internet of Things (IoT) signal controller, which was considered a low-cost green device. The natural electrical properties of HCNTs may be bad and need to be further optimized. Next, by using nanofiller HCNTs, Jin et al. chose the PEDOT:PSS as the composite matrix to improve the mechanical flexibility and thermoelectric conversion efficiency of the composite[80]. The composite could achieve an improved ZT value of 0.01 and visible/NIR absorption, which finally demonstrated a nW level power output.

2.4.2. MXene

MXenes, as a flourishing group of two-dimensional materials, was initially discovered by Yury Gogotsi's team at Drexel University in 2011[81]. This material family is composed of transition

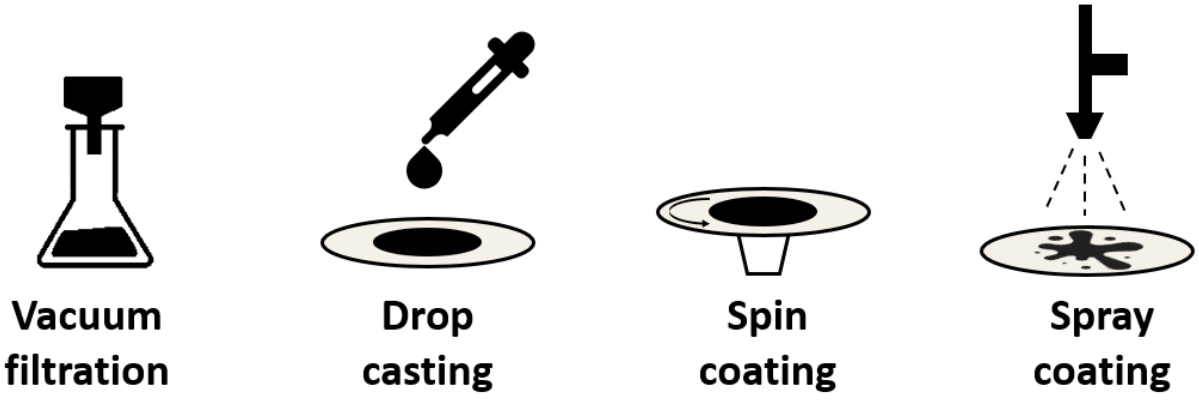

Figure 2-10. Common membrane or film preparation methods.

metal nitrides, carbides, and carbonitrides. Generally, the MXene formula is defined as $M_{n+1}X_nT_x$, where M expresses the transition metal, X indicates carbon or nitrogen sites, and T expresses the surface terminations of outer transition metal layers[82]. In the last decade, MXenes have indicated application potential in photodetectors and surface resonance sensors[83]–[85], which exhibit

advantageous optoelectrical properties, such as broadband electromagnetic absorption and surface plasma excitation[86]–[88]. The thermoelectric properties of MXene are also proven[89], [90].

For MXene membrane fabrication, various methods are also presented depending on the designed thickness and modification. The potential methods for PTE detectors may include drop casting[91], [92], spin-coating[93], [94], spray-coating[95], [96], vacuum filtration[97], [98], and printing[99], [100](**Figure 2-10**). Drop casting is a relatively facile way to fabricate a membrane, but it is challenging to control the diffusion area of the liquid. The drying process also leads to a less uniform membrane. Spin-coating can be used to fabricate thin membranes relying on the spin speed, but the final membrane may be difficult to connect and cannot form a conductive network. Spray-coating can easily control the spray area but may cause a rough surface. Vacuum filtration is one method that can obtain individual membranes without substrate. For PTE detectors, suspended devices may enhance the PTE response. The printing method can accurately pattern the shapes of the MXene membrane and achieves similar functionality to lithography. It requires a higher cost and well-dispersed printing solutions.

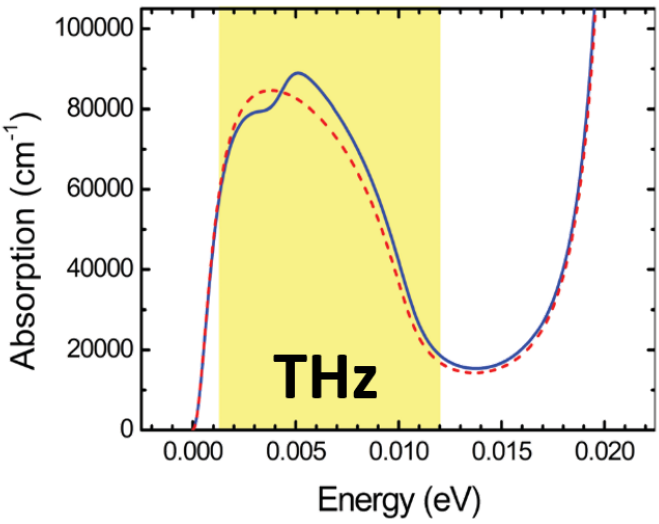

Figure 2-11. Simulated THz absorption of Ti_3C_2[101].

In 2017, Jhon performed the first-principle simulation of MXenes and put forward the application possibilities of PTE detectors or related antennas in the 0.29-2.9 THz spectrum[101]. They demonstrated that both single-layer and stacked Ti_3C_2 showed metallic electronic properties and high THz absorption coefficient up to 9×10^4 cm^{-1}(**Figure 2-11**). By using an electrode-channel-electrode configuration, the thermoelectric ZT value of n-doping stacked Ti_3C_2 could reach 0.112.

Zhou et al. investigated the detectors to demonstrate the MXene-related PTE effect[102]. With a 12.8 mW power intensity of 1064 nm wavelength, they fabricated an MXene device and showed a photovoltage of around 16 μV. In comparison, the other in-plane MWCNT/MXene heterojunction structure measured a photovoltage of 40 μV. The wrinkled surface of MXene might enhance light absorption. The doped carrier concentrations of MWCNT and MXene are 3.83×10^{20} and 3.01×10^{20} cm^{-1}, i.e. the electrical conductivity of MXene is advantageous. The carrier mobility of the MWCNT and MXene were 18.9 and 0.20 cm^2 v^{-1} s^{-1}. With a 12.8 mW power intensity of 1064 nm wavelength, the fall and decay were 768 ms and 668 ms, respectively. The electron-phonon in the junction interface might be strong and limit the response time. The PF values of MWCNT and MXene were 0.05 and 1.6 μW m^{-1} K^{-2}. The Seebeck coefficients of MWCNT and MXene were 10.0 and -5.0 μV K^{-1}. The thermoelectric properties of 2-D MXene might be decent but not competitive. According to the PTE properties of MXenes, their better roles might be electrodes. Additionally, enhancing the MXene thermoelectric properties by doping or composite methods might be also viable for future PTE detectors.

2.5. Engineering influential factors of PTE detectors

Except for the active layer of low-dimensional material, there are three main influential factors including electrodes, substrate, and illumination.

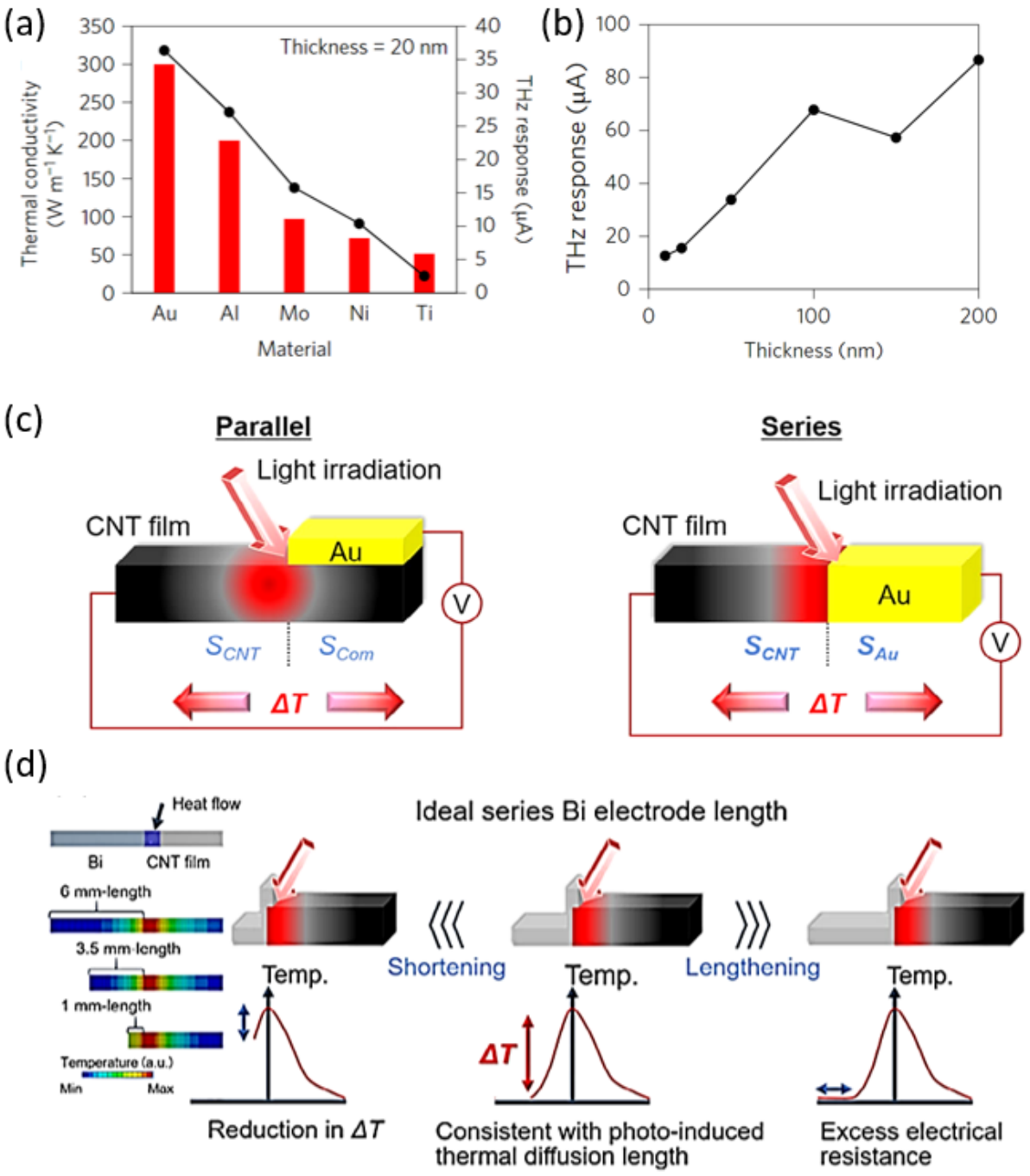

Figure 2-12. The influential factors of electrodes[41], [72].

2.5.1. Electrodes

1) **Figure 2-12 (a)** shows a tight relationship between thermal conductivity of electrode and PTE response. The metal electrodes with a higher thermal conductivity will match a higher PTE response.
2) The work functions of electrodes do not influence the PTE performance[72].
3) With a thicker electrode, the PTE response will increase[72] **Figure 2-12 (b)**. However, the PTE response also depends on the skin effect, which will affect the role of electrode, i.e. heat sink or heat source.
4) By applying a series structure instead of a parallel structure, the PTE response is 4.7 times more larger[41]. The reasons result from PTE coupling effect between metal electrodes and CNT films **Figure 2-12 (c)**.
5) The length of electrode also influences the PTE response maybe because of the heat diffusion length **Figure 2-12 (d)**. The optimized series Bi electrode length is about 3.5 mm[41]. Shorter electrode may cause reduced thermal gradient and longer electrode brings about higher electrode resistance.

2.5.2. Substrate

1) The substrate can be divided into flexible and rigid materials. Usually, rigid materials can provide more mechanical support, and the uniformity and quality of the substrate surface can be better guaranteed. Flexible materials can provide more possibilities for current wearable applications.

2) Thermal conductivity of the substrate will influence the thermal loss, and finally influence the PTE response, i.e. the substrate act as the role of the heat sink. According to the temperature difference equation, the reduced thermal loss will benefit the photothermal conversion and

finally enhance the PTE response. The suspended glass substrate will show a higher photovoltage than the glass[71] (**Figure 2-13**).

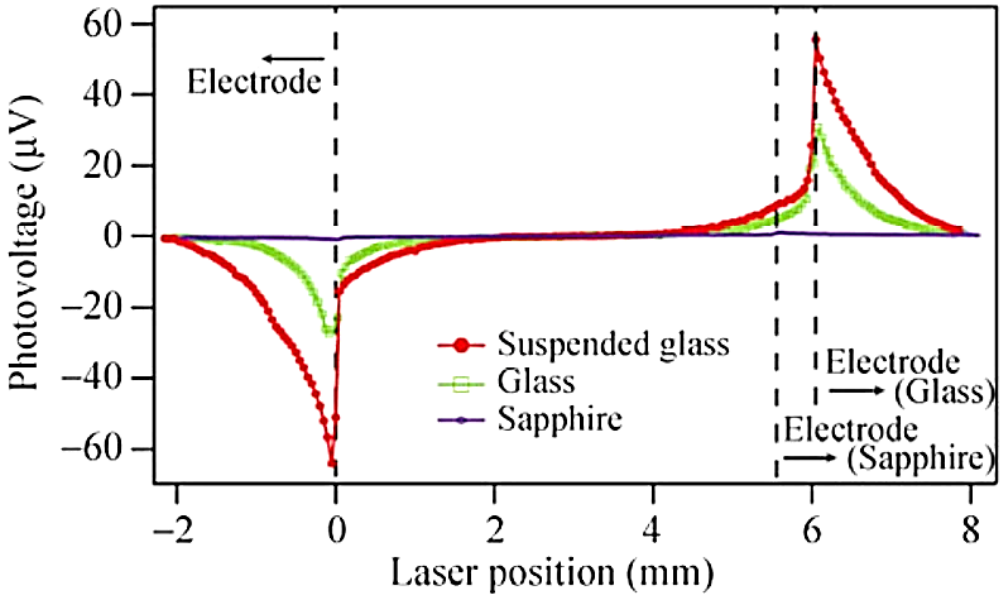

Figure 2-13. The influential factor of the substrate[71].

3) The optical properties like transparency in the visible spectrum may affect the lithography fabrication process and the accuracy of the pattern will decrease.
4) A highly-conductive substrate may cause increased noise. Although the introduction of an insulation layer may mitigate this issue, the signal-to-noise may also increase.

2.5.3. Illumination

Although the PTE effect can just happen within the internal material, the photon-induced temperature difference is relatively small and difficult to track. Therefore, to obtain a larger PTE response, the illuminated spot should be expected to fall on the interfaces, such as the interface between the active layer and electrode or the interface between two different active materials[47], [103] **(Figure 2-14)**.

The illumination position influence also depends on the illumination sources. If the source is a continuous wave, steady-state and real-time tracking will be feasible. If the source is pulsed, the time response of the PTE detector will be affected.

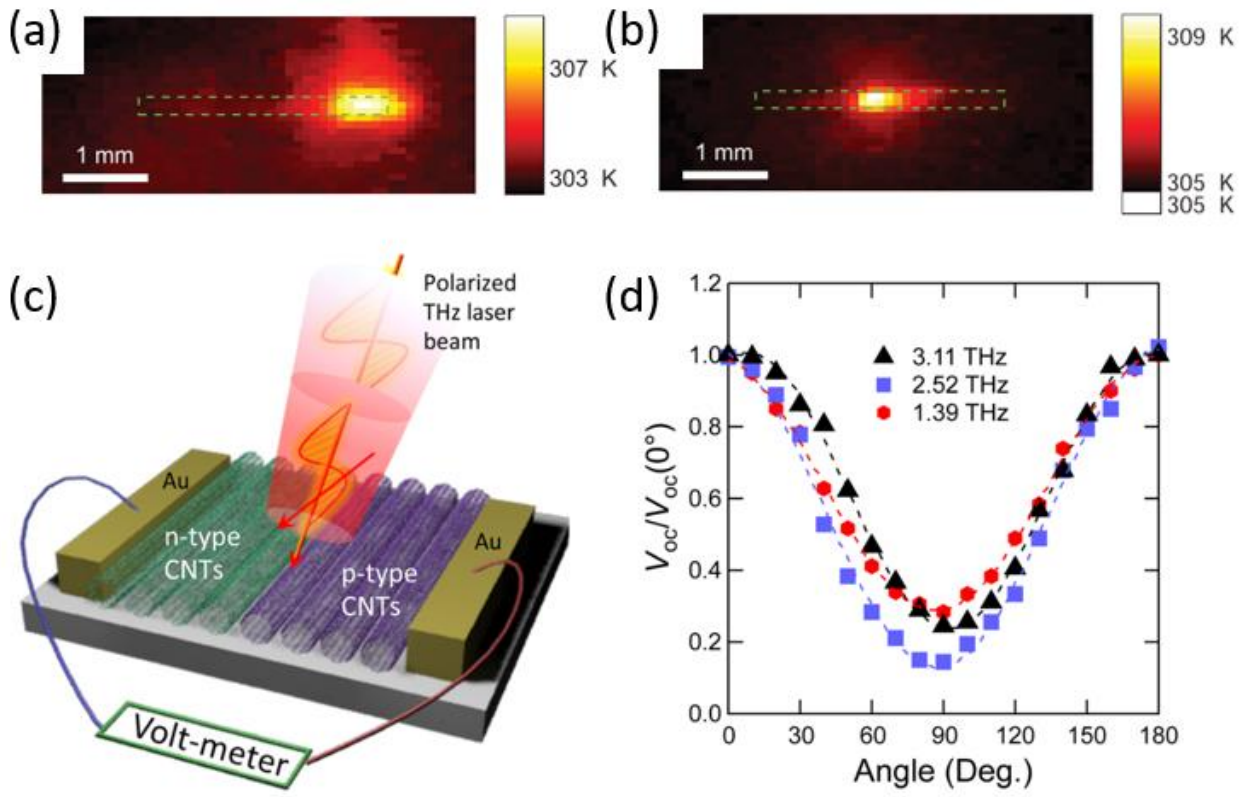

Figure 2-14. The influential factors of illumination[47], [103].

Additionally, the background measurement conditions may also influence the PTE response, such as the vacuum conditions, the background illumination and temperature.

Chapter 3 Capillary-induced CNTF junction

3.1. Background and motivation

CNTs can be regarded as an effective 1-D material for absorbing IR radiation, inherently combining free carrier-based intraband and exciton-based interband absorption processes[104], [105]. With strong metallic properties, MWCNTs can show a heat-induced photoresponse [106]. The broadband absorption ability of CNTs, combined with high-mobility carriers and fast response, open opportunities for photodetectors as well as other optoelectronic applications[68], [79], [107].

State-of-the-art PTE detectors still twist some challenges. First, mainstream sensitive PTE detectors rely on nanometer-level channel length control, which needs the expensive electron beam lithography (EBL) technique. Thus, reducing the cost is urgent for sensitive PTE detectors. Second, current PTE detectors based on thermoelectric junctions need the chemical doping dropped on one spot, finally resulting in a macroscopic film with PTE junctions[108]. For such devices, it is significantly difficult to drop micrometre-level liquid spots and achieve small-area pixel control, which further prevents the miniaturization and integration of devices. Third, in the vertical PTE detectors, metal electrodes are mostly fabricated on the top of photoactive layers, which decreases the IR absorption of active materials.

In this chapter, a high-performance scalable PTE detector driven by capillary-assisted self-assembly CNTs is presented. Lithography processes are performed before the growth of carbon nanotubes, and therefore contaminations coming from photoresists are avoided. By dropping dimethyl sulfoxide (DMSO) on the top of the whole device, the thermoelectric junction is naturally produced without any further CNT transfer. Furthermore, the PTE detectors exhibit a potential

industrial non-destructive testing (NDT) application because the components in the PTE detectors can work under a high temperature of about at least 700 °C.

3.2. Device fabrication

The PTE detectors are driven by the self-assembly CNT thermoelectric junction, fabricated followed by the procedure described as follow:

1) one prime P-type doping Si wafer was immersed in H_2O_2 and H_2SO_4 piranha solution (volume ratio 1:4) for 15 min under room temperature, and the P-type doping Si wafer was rinsed with deionized water and dried by the spin rinse dryer (SRD) machine system;
2) hexamethyldisilazane (HMDS) of 5 nm thickness was initially coated on the cleaned Si wafer at 150 °C for 15 min to enhance the adhesion between photoresist and Si wafer substrate;
3) spun coat the positive photoresist Shipley 1805 (S1805);
4) maskless aligner (MLA) photolithography method was used to pattern the insulating suspended layer and the top electrode layer, followed by a 120 °C post bake process for 90 s;
5) 40 nm Ti electrode was deposited under room temperature without bias by magnetron sputtering system, AJA Inc;
6) unfinished device was first placed immersed into remover PG solution for PMMA removal under 80 °C for 60 min and under room temperature overnight to achieve a lift-off process;
7) the device performed a soft bake process under 120 °C for 2 min to remove the water left inside the wafer;
8) MLA photolithography method employing PMGI/S1805 bilayer photoresist was used to pattern the insulating layer, followed by a 120 °C post-bake for 90 s;

9) Typically, 60 nm SiO_2 insulating layer was first deposited under room temperature without bias by AJA magnetron sputtering system to separate two electrodes and achieve a height difference between two electrodes;
10) 10 nm Cr as a catalyst buffer layer and the electrode layer was deposited, followed by a reliable lift-off process;
11) the device performed a post-bake process under 120 °C for 2 min to remove the water left inside the wafer;
12) MLA photolithography method employing PMGI/S1805 bilayer photoresist was used to pattern the electrode layer and CNT growth layer, followed by a 120 °C prebake for 90 s;
13) 2 nm Ni catalyst film was deposited by E-beam evaporation (Angstrom E-beam Deposition System) onto P-doped Si substrates at 1.5 Å/s growth rate, followed by the same aforementioned lift-off process;
14) the device was cut into the single individual device using DISCO™ dicing saw system;
15) the cold wall plasma-enhanced chemical vapour deposition (PECVD) machine with a 2" graphite heater was used to grow carbon nanotubes. Vertically aligned CNTFs were grown by PECVD reactor at 695 °C, 5 mbar system pressure, and 75 W DC plasma power in an Aixtron Black Magic™ 2 system. Acetylene (C_2H_2) and ammonia (NH_3) flowed at rates of 50 sccm and 200 sccm, respectively. For a typical 15 min and 30 min growth, the CNTF height is about 7 μm and 15 μm, respectively;
16) 10 μL DMSO solution (# 472301, purchased from Sigma-Aldrich®) is dropped cast on the top of the CNTF along with the arrow direction. By controlling the flow direction of the DMSO solution, the alignment direction of the whole CNTF can be controlled, and the CNT forest will fall towards the top electrode to form an ultrashort suspended 'CNT bridge';

17) the device is dried at a 100 ˚C hotplate to evaporate DMSO and enhance the charging CNT network;

18) the device can be connected to the external circuit by using conductive silvery epoxy (MG Chemicals 8331D Silver Conductive Epoxy) for further performance measurement.

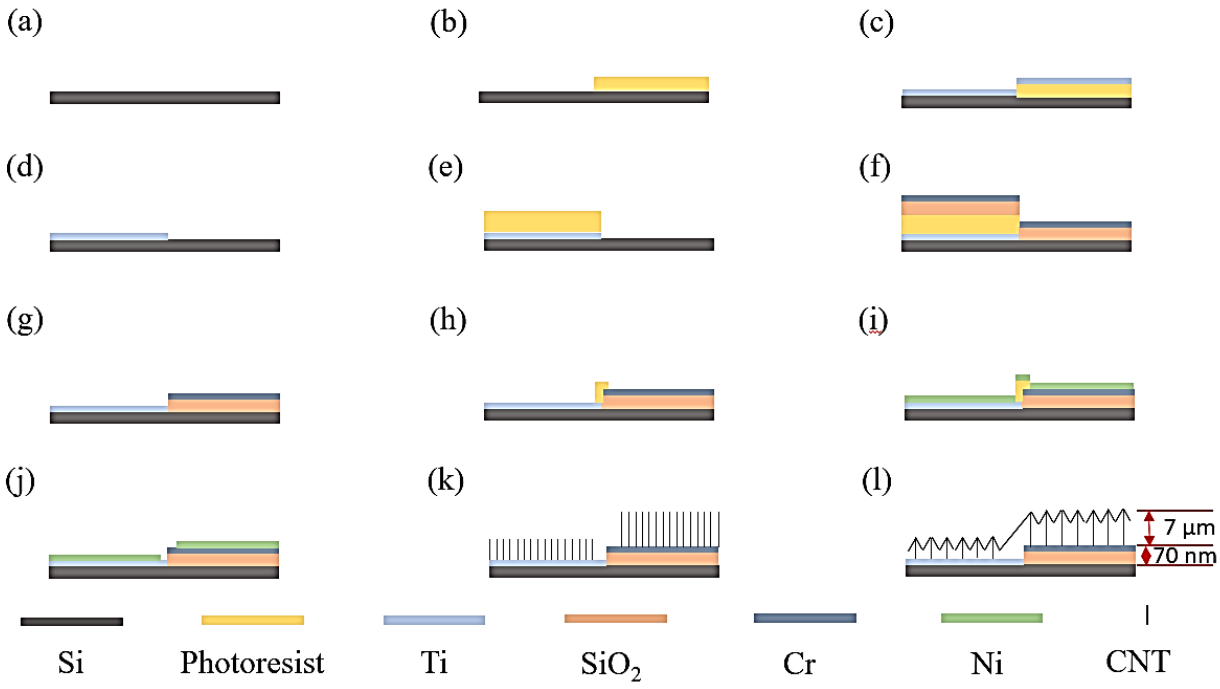

Figure 3-1. (a) Prepare a prime wafer precleaned by a piranha solution. (b) Spin-coat UV photoresist (PR), photolithography (PL) and development. (c) Deposit Ti electrode. (d) Remove PR. (e) Spin-coat UV PR, PL and development. (f) Deposit SiO_2 insulating layer and Cr electrode. (g) Remove PR. (h) Spin-coat UV PR, PL, and development. (i) Remove PR. (j) Deposit Ni catalyst layer. (k) Grow CNTs. (l) Drop DMSO. The illustration is not drawn according to the scale.

The fabrication process of the device is shown in **Figure 3-1.** As a plasma-enhanced method is used to grow CNTs, some gaps exist among the vertical CNTs. When the liquid enters the gaps,

the capillary forces induce the liquid into the buffer layer or even the electrode layer and Si substrate. Although the metal surface is hydrophobic, the repeated drop-casting along with the flowing direction control of the liquid assists the CNTs soak among the interspaces. The existence of DMSO may help optimize the energy filtering effect, thus leading to an enhanced thermoelectric performance[109]. DMSO also can induce a non-overlapped CNT thermoelectric junction. According to previous experimental results, an increased overlapped area of the thermoelectric junction will significantly reduce the PTE performance[40]. Thus, our device without overlapped junction will not cause a thermal loss in the junction area. Previously, researchers mainly focus on the aligned CNTs in parallel or perpendicular to the illumination[40], [108], and few papers refer to the capillary force-driven self-assembly CNT clusters. Additionally, pristine aligned CNTs show a strong polarization sensitivity ranging from a broad spectrum with low noise. However, they are mechanically unstable and easily broken. Their polarization sensitivity also provides challenges for the shape or area design of PTE detectors. Therefore, the CNT cluster is used to satisfy global IR illumination requirements.

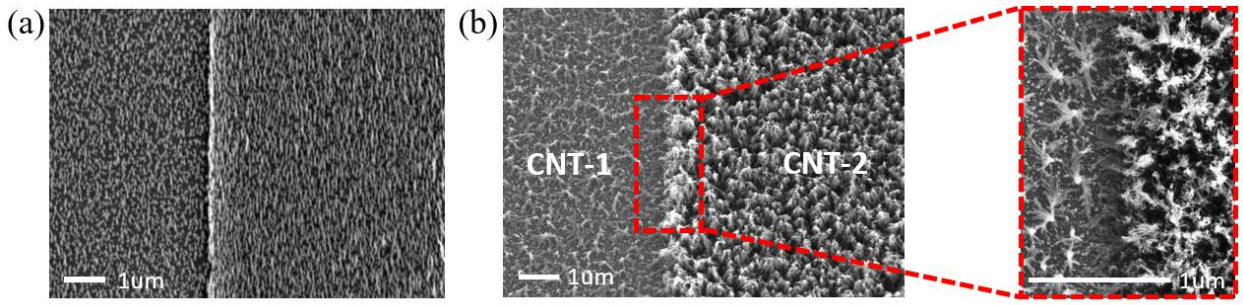

Figure 3-2. SEM image of (a) vertical CNTs and (b) CNT cluster addressed by DMSO. The enlarged red part of the CNT bridge.

In our configuration, the CNT channel addressed by DMSO acts as a bridge to connect two asymmetric height-difference electrodes and create the circuit (**Figure 3-2)**, where Ti and Cr are

selected as electrodes because they can endure high temperatures up to 700 ºC, which can enable future industrial applications. Furthermore, this configuration can benefit the miniaturization and integration of PTE sensors.

3.3. Photoresponse measurement

Given the IR response mechanism of our detector, the pyroelectric mechanism can be excluded because of its general typical capacitor configuration and pyroelectric material. The bolometric and photoconductive mechanism needs external bias, but our detector works under zero bias. As for the photovoltaic mechanism, the relatively low photon energy in the MIR regimes is difficult to induce photocarriers. When electromagnetic radiation illuminates the device, the CNTs will absorb the photon energy and the temperature of CNTs will increase. The temperature difference of the CNT-1 area and CNT-2 area is tested with the incident power intensity of 2.1×10^4 μWmm^{-2} (**Table 3-1**), which demonstrates our detector is dominated by the PTE mechanism. Due to the different growth conditions, the dimensions and lengths of CNTs are various, which will show

Table 3-1. The temperature is measured by an IR thermometer and related figures of merit.

Blackbody Radiation Temperature (K)	Ambient And Intial Temperature (K)	Temperature Difference (K)	Photovoltage (μV)	Seebeck Coefficient Difference (μV/K)
773	295.6	4.7	65.7	13.9
973	295.7	6.3	87.6	13.9
1173	295.6	8.5	120.1	14.1

different Seebeck coefficients[110]. For the CNT clusters, it is challenging to measure the Seebeck coefficient because their metal buffer layer may cause a short circuit of the measurement setup. Given that the skin depth of the metal electrode Ti is over 37 nm in the 100 terahertz (THz, 3.0 μm) regime (**Table 3-2**), the Ti electrode of 40 nm is highly IR reflective as a heat-sink role. The thickness of the Cr electrode is about 10 nm, which is under the skin depth of Cr in the THz regime.

Table 3-2. The data of bulk resistivity and relative permeability from https://www.rfcafe.com/references/calculators/skin-depth-calculator.htm

Metal material	**Bulk resistivity@20ºC (μΩ×cm or Ω×10^{-6}cm)**	**Relative Permeability μ/μ0**	**Skin depth at**		
			1 THz (nm)	**10 THz (nm)**	**100 THz (nm)**
Chromium (Cr)	13.2	1	183	58	18
Titanium (Ti)	54	1	370	117	37

Thus, the Cr electrode will act as the heat source combined with the top CNTs[38], [73]. The CNT-2 area and Cr electrode will form the CNT-Cr composite. Here, the Seebeck coefficient difference is evaluated $\Delta S = \frac{V_p}{\Delta T}$, where V_p is the photovoltage of the detector, ΔT is the temperature difference. The calculated Seebeck coefficient difference is 14.0 μVK^{-1}, which can be further optimized by changing the concentration of DMSO and physical parameters of CNTs.

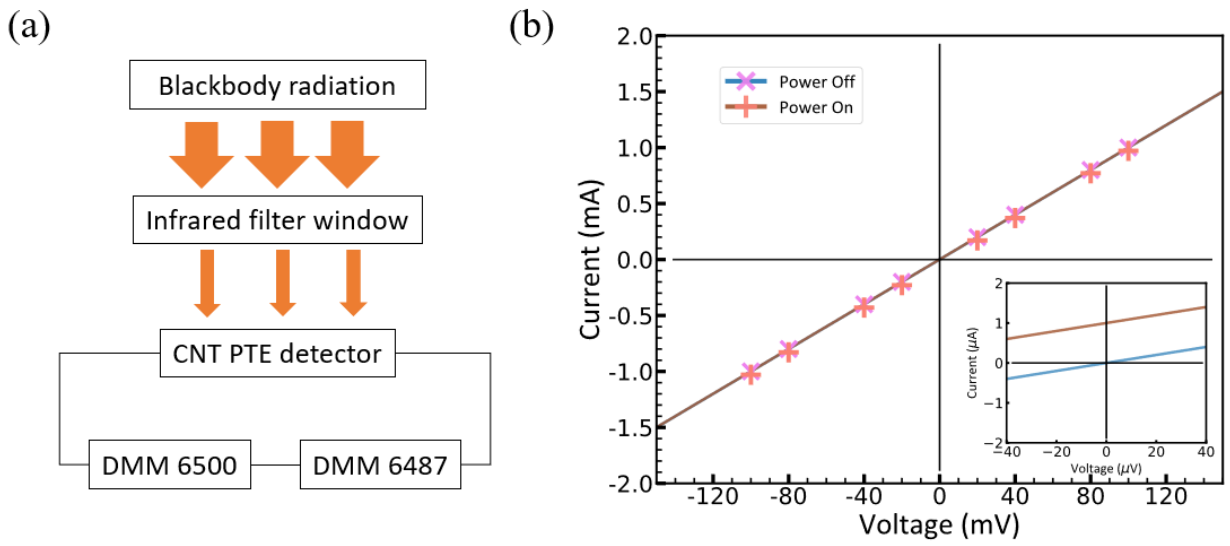

Figure 3-3. (a) The instrument of photoresponse measurement of the CNT PTE detector. (b) I-V curve of single-pixel CNT PTE device.

During the measurement, the detector was irradiated by the filtered continuous-wave (CW) IR waves with about 2.1×10^{4} μWmm^{-2} input power, and the photocurrent was directly recorded using the DMM6500 current-time module (**Figure 3-3 (a)**). **Figure 3-3 (b)** showed the current-voltage (I-V) curve performance of the PTE detector under dark or radiated conditions. The I-V measurement would be performed at room temperature and ambient atmospheric conditions. The blackbody temperature was set at 1173 K. The linear characteristic could demonstrate that both electrodes and CNTs form Ohmic contact in a large imposed voltage range from -120 mV to 120 mV. Additionally, the thermoelectric junction of CNT interfaces did not generate the rectification effect because the PECVD-grown CNT might consist of many semiconducting and metallic CNTs, which might activate the metallic properties of CNTs[40]. The PTE current could be observed without any external bias. These results illustrated that PTE detectors could be used as IR energy harvesters or further applied for collecting waste energy.

Response time is also an important parameter for evaluating PTE detectors, including rising and fall time, which can be defined as the period when the PTE current increases from 10% to 90% on the rising time of or the falling times of one pulse amplitude, respectively[111].

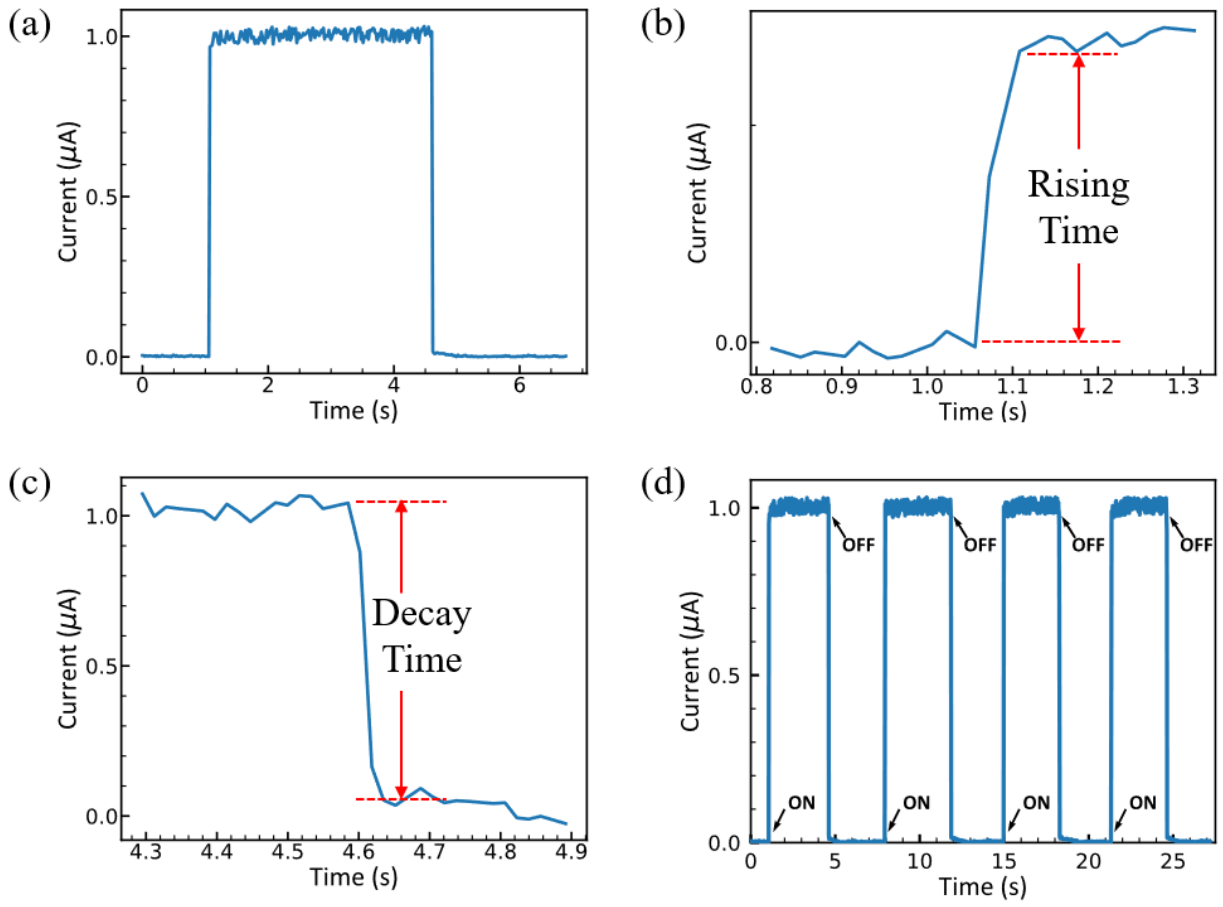

Figure 3-4. (a) The response time of the CNT PTE detector, where (b) and (c) express the rising and decay time, respectively (d) Reproducible time response. The current changes with time.

During the on-off curve measurement, one thick aluminum foam is put between the IR-filtered window and CNT PTE detector. When the blackbody radiation is the on status, the DMM6500 machine would record the photocurrent of the off status. When the foam is removed quickly, the photocurrent would increase and be recorded as the on-status photocurrent. Our detector exhibited a rise time of 40 ms and a falling time of 60 ms without external bias, substantiating the real-time

IR signal tracking capacities (**Figure 3-4 (a)-(c)**). **Figure 3-4 (d)** shows a reproducible current response with resolved time. Such a fast response speed may originate from the localized eletromagnetic field enhancement induced by the nanometre level height difference. Additionally, the thermoelectric junction is created by no-overlapped conductive CNTs, which may reduce thermal loss. Furthermore, the experimental model can be applied to other nanowire-based systems designs, which is expected to further optimize the performance of PTE detector arrays.

In the view of practical applications, specific detectivity is also one property used to evaluate the performance of the PTE detector, which is characterized as the capacity to track the weak signals compared with the noises and can be represented as, $D^* = \frac{R_V\sqrt{A_d}}{V_n}$ [112]. R_v is the responsivity of the device and is expressed as $R_V = \frac{V}{P_{in}}$, where V is the photovoltage and P_{in} is the total incident radiation power. V_n is the mean root square of the noise voltage and is defined as $V_n = \sqrt{4k_BTR}$, where k_B is Boltzmann constant, T is temperature, and R is device resistance[72]. For the PTE detector, the thermal Johnson-Nyquist noise dominates. The total incident power is calculated by the integral of spectral radiant emittance with a wavelength of over 1.5 μm because the cut-off wavelength of the infrared window is 1.5 μm. In the measurement, it is assumed that all incident is absorbed by the detector, and thus the practical responsivity or detectivity should be larger than the calculated value. With different blackbody radiation temperatures, **Figure 3-5 (a)** shows the zero-bias PTE response under broad illumination. The detectivity can reach a 10^8 level Jones when the black-body radiation is set up from 573 K to 1173 K, which matches a center wavelength from 5.06 μm to 2.47 μm, which demonstrates that our device can satisfy the demands for IR broadband detection. Such a broadband detection capacity matches the intrinsic properties of IR thermal detectors.

The blackbody power intensity versus responsivity and NEP is characterized in **Figure 3-5 (b)**, showing a roughly linear relationship. According to Stephan-Bolzmann's law, the

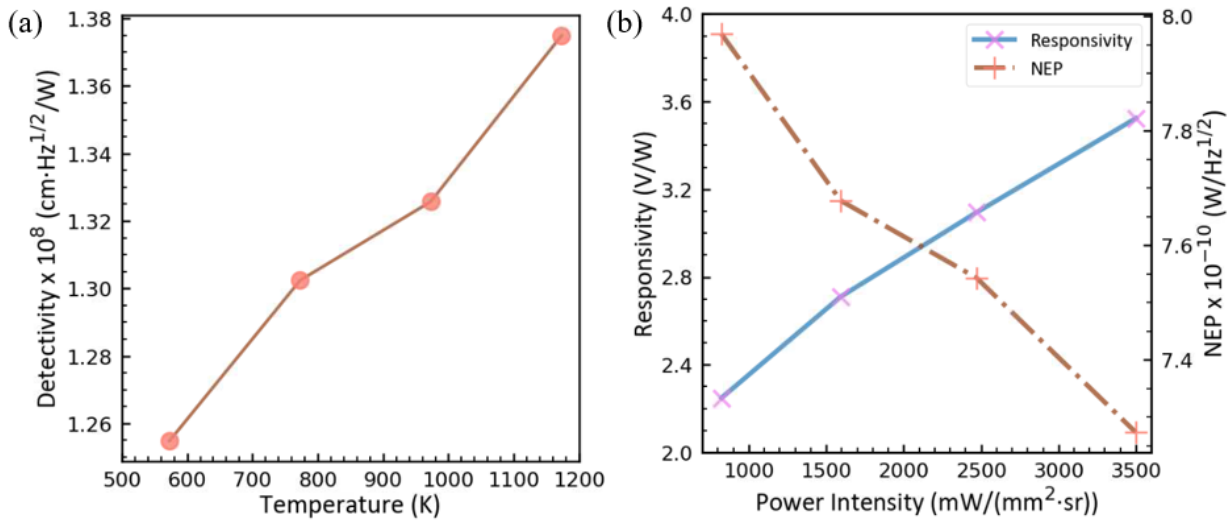

Figure 3-5. (a)The detectivity dependence on different black-body radiation temperatures. The inset picture is the peak spectral intensity with varying black-body temperatures. (b) The responsivity and NEP change with different power intensities.

blackbody power intensity should be proportional to the fourth power of the temperature. This linear contributes to two reasons. Firstly, the significant temperature difference between the device system and the surrounding temperature may cause thermal losses. If the detector is placed under a high-level vacuum system, the PTE current is expected to reach a higher level because of the reduced thermal losses[47]. Secondly, with a higher blackbody temperature, the peak wavelength will change. This detector using the novel thermal junction may show typical absorption for different wavelengths.

3.4. Stability

Long-term stability is also a key figure of merit in evaluating the performance of PTE detectors. Normally, the performance of IR detectors can be affected because they directly contact air and

can be moist and metamorphic, eventually resulting in degeneration under ambient conditions. Thus, the PTE response of the device is tested every seven days. After 56 days, the detector still demonstrated a highly advantageous reproducibility and matches well with the original experimental results, indicating excellent stability and durability in the air. The continuous high photoresponse contributes to the oxidization of the endpoints of CNTs, i.e., the addition of DMSO has oxidized one side of CNTs and prevents the further photoresponse degradation of CNT-based PTE detectors (**Figure 3-6**).

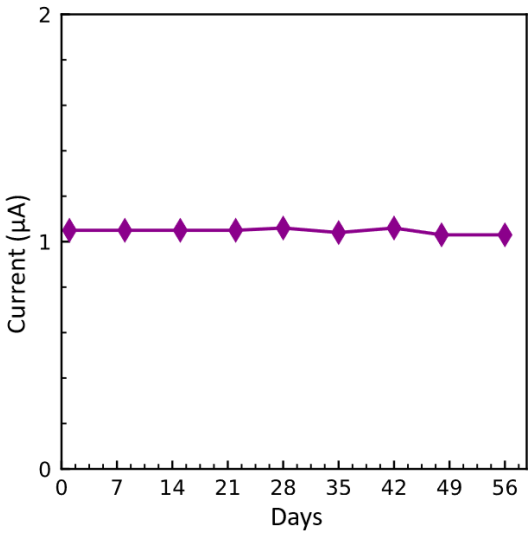

Figure 3-6. The durability test of the CNT PTE detector. The total test time is 56 days with a 7-day period.

3.5. Conclusion

This chapter proposes a scalable PTE detector design utilizing self-assembly CNT thermoelectric junction among microscopic CNT components, providing high-performance and stable IR photoresponse. Typically, the detector shows the broadband MIR response and stable photoresponse within two months. During this design, the naturally grown CNTs act as an active

element of the PTE detector. It opens significant opportunities for large-area IR detection integrated with CNTs, and also offers new design sights for other Si-based sensors.

Chapter 4 Nanocomposite component optimization in PTE detectors

4.1. Background and motivation

Infrared optoelectronic materials and devices are hot topics for next-generation smart scalable IoT applications such as medical imaging, remote sensing, and fitness tracking[72], [113]. However, current tracking technologies are relatively costly and difficult to achieve real-time monitoring—these issues stimulate global researchers to explore novel portable sensors[114]. In the last decade, PTE detectors based on the photothermal and thermoelectric effects attract much attention because they can detect electromagnetic radiation in a broad wavelength range. For human body emission, the electromagnetic regime covers mid-wavelength infrared (MWIR) and long-wavelength infrared (LWIR) with a peak wavelength of 9.3 μm[31], in which PTE-based detectors can function well. Also, PTE detectors have simple device configuration[26], long-term ambient stability[10], and relatively easy array integration[31], which suits building up health monitoring applications.

With the recent progress of low-dimensional materials and composites, PTE conversion materials have been explored, including graphene[8], black phosphorous[38], CNTs[108], silicon ribbons[115], and topological quantum materials[116]. As the two-dimensional star material, monolayer graphene possesses the zero-band gap enabling broadband optical absorption and high carrier mobility enhancing the photoresponse[117]. The as-fabricated graphene-based PTE detectors can achieve a detectivity of 4.6×10^5 Jones in a broadband range[8]. However, high-quality single-layer graphene has a high price and complex massive fabrication. As for black phosphorus-based devices, the poor ambient stability seriously limits their further applications[38]. Silicon-based devices are low-cost, but they only can detect visible spectrum[115]. Topological insulators are also explored as high-performance broadband PTE detectors[116], but expensive

and laborious epitaxial growth fabrication limits their applications. In contrast, CNTs are competitive PTE materials and the 1-D detector array has been fabricated for far-infrared imaging with noise equivalent power (NEP) less than 1 $nWHz^{-1/2}$ [26]. However, pure CNT film detectors are unstable under deformation because the Van der Waals interaction between adjacent CNTs is weak[104]. Herein, solution-processable poly (3,4-ethylene dioxythiophene) polystyrene sulfonate (PEDOT:PSS) has been demonstrated as an advantageous thermoelectric material and the capability of IR absorption[118], [119]. As the composite matrix, the addition of PEDOT:PSS can significantly enhance the photo responsivity and mechanical stability of as-fabricated detectors[120]. Based on the equation $U=-S\times\Delta T$, where U is thermoelectric-driven photovoltage, S is Seebeck coefficient, and $\triangle T$ is the absolute temperature difference, a higher photovoltage means a higher Seebeck coefficient and larger temperature difference[121]. The combination of CNTs and PEDOT:PSS may enlarge the Seebeck coefficient and temperature difference Furthermore, remarkable progress has been made on CNT/PEDOT:PSS composites in the field of thermoelectric devices[122]–[127].

In this chapter, two structures of PTE detectors based on CNT and PEDOT:PSS composite are proposed. The flexible membrane based on the single-walled carbon nanotube (SWCNT)/PEDOT:PSS composite was fabricated for monitoring ocular gestures. An optimized photoresponse was obtained in 20 wt% SWCNT loading, and a peak detectivity of 1.9×10^{7} Jones was achieved. Finally, the ocular monitoring experiments can clearly distinguish the blinking cycles and times. The Si-based PTE detector was verified for the NDT technique. The photocurrent was found the highest with 30 min CNT growth. A crossing pattern was roughly mapped likewise. The above results prove that the PTE detectors based on SWCNT/PEDOT:PSS composite are a profitable choice for MWIR detection and hold potential for health monitoring applications.

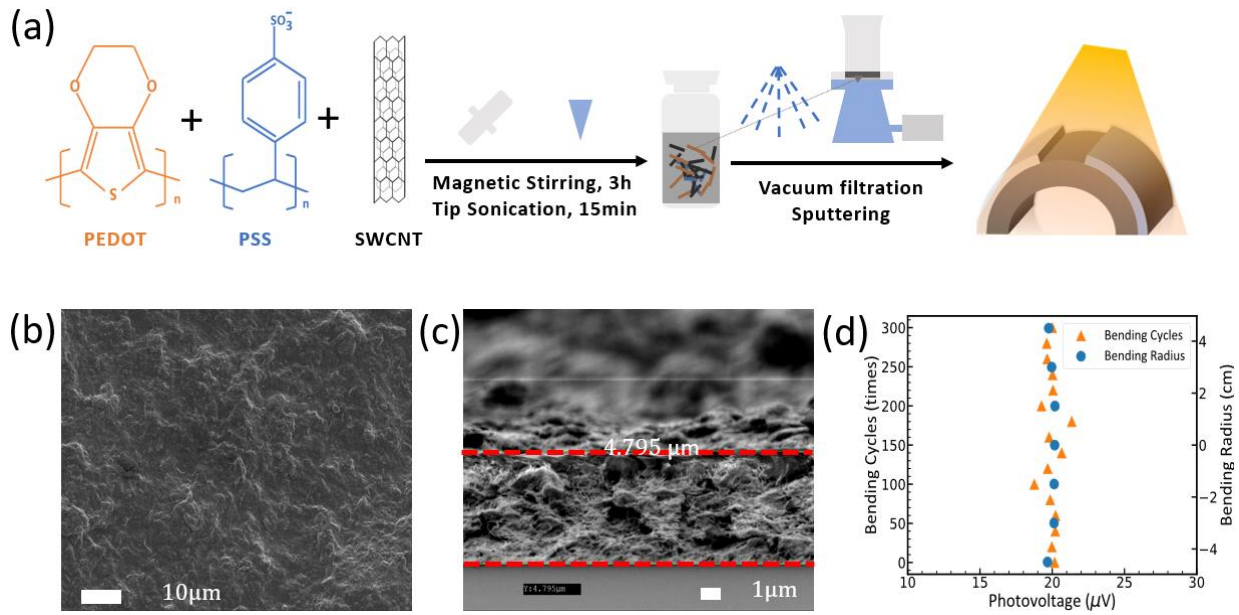

Figure 4-1. (a) Fabrication process of the flexible and free-standing SWCNT/PEDOT:PSS film and schematic device configuration under illumination. SEM pictures of 20 wt% CNT/PEDOT:PSS composite in the (b) top view and (c) cross-section view. As seen from the above SEM pictures, CNTs are well dispersed and embedded within the polymer. The 20 wt% SWCNT/PEDOT:PSS composite is porous. (d) The relationship between photovoltage and the bending cycles/radius.

4.2. Suspended PTE detectors based on SWCNT/PEDOT:PSS composite

A total of 1 mL solution is dropped onto the membrane in the vacuum filtration assembly (# Z290467, purchased from Sigma-Aldrich®). With the vacuum pump (125 W) opening, the free-standing and flexible thin film can be fabricated overnight. The relatively low-cost asymmetric Al (200 nm) and Ti (120 nm) electrodes is sputtered onto two sides of the membrane by a square shadow mask pattern (AJA Orion twin-chamber magnetron sputter system). Wires were connected to electrodes via epoxy silvery glue and Kapton tape.

As seen in **Figure 4-1**, the details of the fabrication process and schematic structure of

SWCNT/PEDOT:PSS infrared detectors are given. It is worth noting that 15 min tip sonication is used to make the solution disperse evenly. Longer sonication time may shorter the length of SWCNTs, resulting in reduced percolation path and decreased device performance[128]. The top-view and cross-section morphology of the SWCNT/PEDOT:PSS film is characterized by using SEM where the well-dispersed surface can be observed (**Figure 4-1 (b)**). From the cross-section view, a porous structure can be seen on account of mixing core-shell PEDOT:PSS and SWCNTs (**Figure 4-1 (c)**). Hexagonal SWCNTs network composed of sp^2 hybridized carbon atoms is a particular conjugated polyenes structure. In such a structure, numerous delocalized π-bond networks are relatively facile to produce because electrons will move more actively among different unhybridized orbitals[117]. When SWCNTs are inserted into π-bonded conjugated PEDOT:PSS polymer, the interaction between SWCNT and polymer chains changes carrier density and creates more free delocalized carriers in PEDOT chains[129]. For the PTE mechanism, more delocalized carriers mean a larger temperature gradient change because lattice vibration usually remains unaffected, but photon-induced hot carriers are more easily changed[130]. The percolating path formation of the SWCNT network in the polymer matrix also contributes to photon absorption and conductivity enhancement. Additionally, it is assumed that the as-produced pores build up extra phonon scattering centers where electronic transportation is almost unaffected but lattice thermal conductivity is decreased [131]. Based on the above theories, the PTE conversion can be improved by mixing SWCNTs and PEDOT:PSS.

Flexibility is an important parameter for next-generation optoelectronic devices when employed in the wearable monitoring system. **Figure 4-1 (d)** demonstrates the stable photovoltage performance of our SWCNT/PEDOT:PSS detector after bending different radii and cycles under blackbody radiation. This means that no apparent changes are observed in the photovoltage

performance even after 300 cycles of bending at a 4.5 cm radius. This phenomenon can be attributed to the stable interaction between SWCNT filler and the polymer matrix.

4.3. Si-based PTE detectors based on CNT forest/PEDOT:PSS composite

(1) Prepared a 4-inch single-polished high-resistance prime silicon wafer. (2) Used RCA-1 to reduce organic impurities and RCA-2 to reduce metallic contaminations. (3) Performed 2 min O_2 plasma cleaning process. (4) HMDS coating. (5) Spun-coat PMGI and S1805 at one side of Si wafer. The first step of this recipe was a 100 ramp-up for 5.0 s. Second, the 1000 rpm/s ramp-up and 5000 rpm speed are used for 60.0 s. Third, the spin-coating speed dropped down at 500 rpm/s. The thickness of S1805 is about 600 nm. (6) Exposed the electrode pattern using maskless lithography (MLA). With a dose test, the dose value was selected 89 mJ/cm^2 and defocus value is -2. (7) Used MF-319 to develop for 60 s, rinse using DI wafer, and N_2 drying. (8) Deposited 165 nm metal Cr. (9) Lift-off process. (10) Repeated (3)-(5) steps and deposit 20 nm metal Ni catalyst layer. (11) Lift-off process. (12) Grew CNTs using PECVD at 700 °C. The gas ratio of C_2H_2 and NH_3 is 50:200. (13) Drop-cast 10 μL PEDOT:PSS on the top of each CNT forest. A stable CNT forest/PEDOT:PSS composite structure forms. (14) Fabricate PET deposition mask using laser ablation method. (15) Deposited the top gold electrode of 100 nm thickness.

The vertical structure of an oriented CNT-based PTE detector is much advantageous to fabricating on Si substrate. The vertical structure can save space and offer opportunities for device miniaturization. In this fabrication process, the metal Cr is first used to act as the bottom electrodes and buffer layer for CNT growth. It can endure a high temperature of 700 °C. Then Ni catalyst layer was adopted for large-area CNTF growth. By controlling the growth time, the CNT length

can be controlled, and the CNT concentration of the composite can be adjusted (**Figure 4-2**).

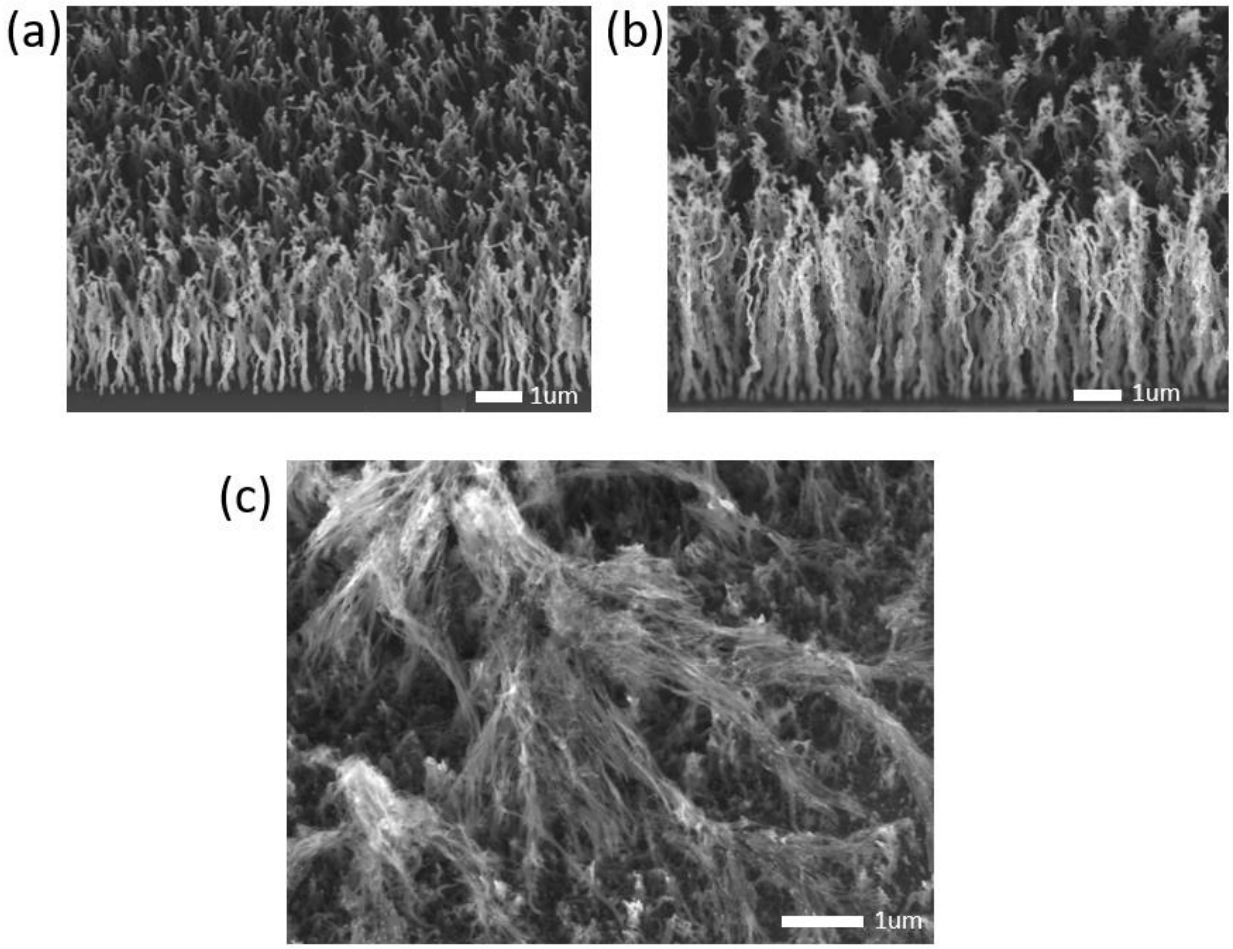

Figure 4-2. The CNT SEM with growth time of (a) 15 min, (b) 30 min, and (c) 45 min.

The CNT growth using PECVD shows a relatively large gap and it is difficult to create a top electrode layer and form a conductive plate path (**Figure 4-3**).

The addition of PEDOT:PSS can help fill in the gap (**Figure 4-3 i**), and simultaneously does not damage the CNT forest structure. The choice of Al electrodes originates from the low infrared absorption suppression. Additionally, the vertical structure reduces the channel length and achieves a fast PTE conversion. The channel length is approximately equal to the height of CNTF or a little larger than CNF height. The thickness of top Al electrodes is 20 nm, which is smaller

than skin depth in the infrared region. Thus, the Al electrodes play a heat-source role. When the infrared radiation illuminates on the top, a vertical temperature difference will be formed. According to the thermoelectric theory, top electrodes show a higher temperature, and bottom electrodes will show a lower temperature. Thus, the photo-induced current will flow from the top electrodes to the bottom electrodes.

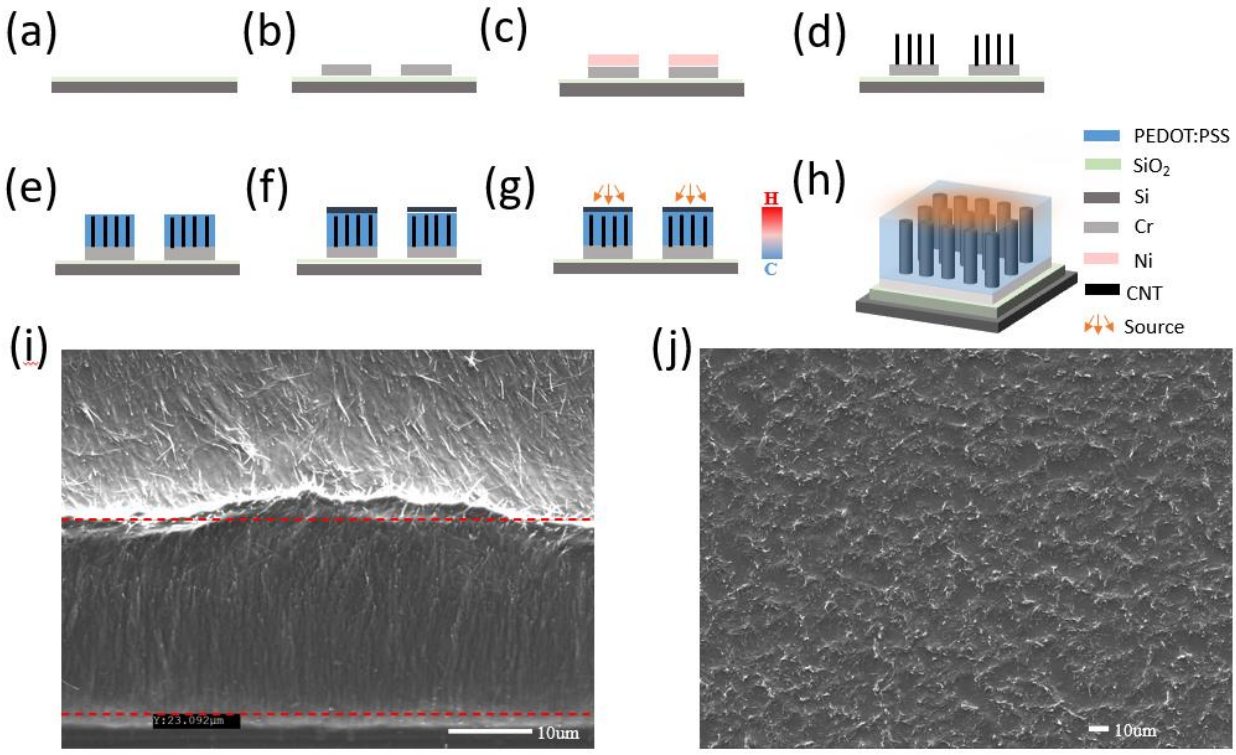

Figure 4-3. (a) Deposit SiO_2 on Si substrate. (b) Pattern bottom Cr electrodes. (c) Deposit Ni catalyst layer. (d) Grow CNT forest. (e) Drop PEDOT:PSS and dry naturally. (f) Deposit Al electrodes. (g) 2D schematic PTE detector model. (h) 3-D schematic PTE detector model. (i) Side-view of CNTF/PEDOT:PSS layer. (j) Top-view of CNTF/PEDOT:PSS layer.

4.4. Photoresponse measurement

The current-voltage (I-V) curve with and without blackbody radiation was measured (**Figures 4-**

4 (a) and **(b)**). The linear behaviour demonstrates that both of our devices have good Ohmic contact, and the device resistance of the suspended and Si-based detector was calculated as 100 Ω and 60 Ω, respectively. As a PTE detector, several figures of merit require to be highlighted.

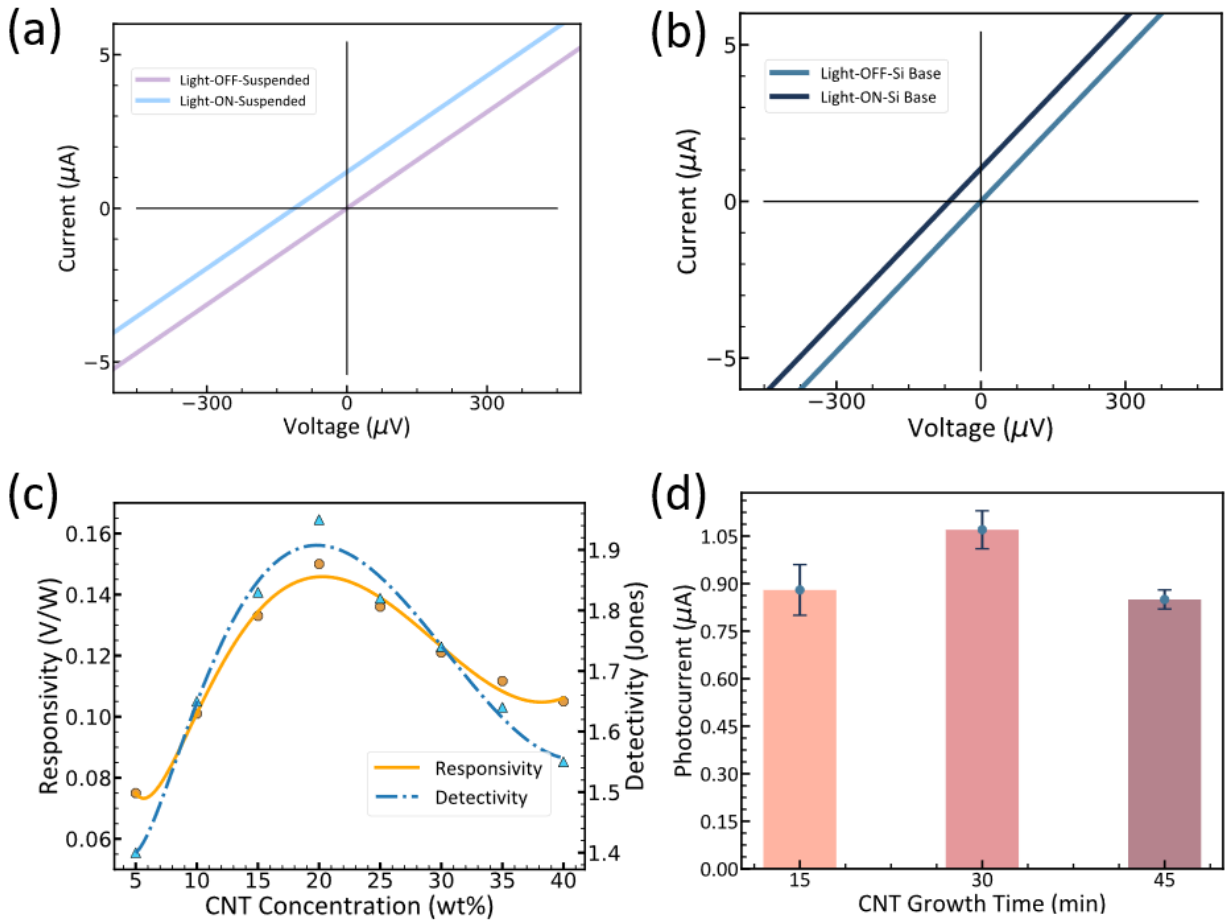

Figure 4-4. I-V curve for (a) SWCNT/PEDOT:PSS detector and (b) CNTF/PEDOT:PSS detector. (c) The responsivity and detectivity change with the CNT concentration. (d) The photocurrent changes with the CNT growth time.

Photoresponsivity that quantifies the detector sensitivity can be denoted as $R_V=V_{ph}/P_{in}$, where V_{ph} is the photoinduced voltage, and P_{in} is the incident power[26]. In a PTE detector operating at zero bias, the dark noise is mainly limited by the Johnson-Nyquist noise $V_n=(4k_BTR)^{0.5}$[10]. Therefore, the specific detectivity used to detect the smallest photonic signals can be denoted as

$D^*=R_V(A_d)^{0.5}/V_n$, where A_d is the photoactive area, $k_B=1.9\times10^{-23}$ $J\cdot K^{-1}$ is the Boltzmann constant, T is the ambient absolute temperature, and R is the channel resistance[132]. By increasing the CNT loading from 5 wt% to 20 wt%, the detectivity increases by about 30 % under the same blackbody illumination (**Figure 4-4 (c)**). The main reason can be ascribed to the reduced resistances of the PTE detector (**Figure 4-5**). Responsivity has a similar upward trend to detectivity.

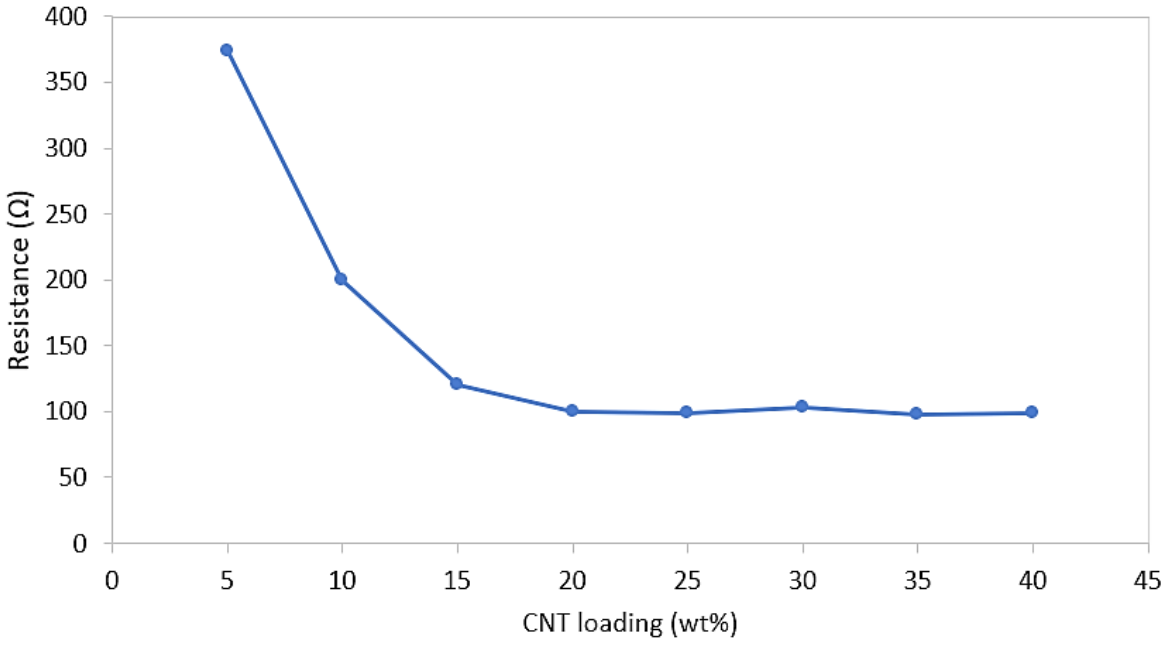

Figure 4-5. The device resistances of the SWCNT/PEDOT:PSS composite at different CNT loadings. The electrodes are 200 nm Al and 120 nm Ti.

For this phenomenon, the reason may be that increasing CNT loading results in stronger photon absorption and enhanced thermoelectric efficiency because of the energy-dependent scattering mechanism, i.e. energy filtering and tunnelling effect[133], [134]. When the CNT loading increases from 20 wt% to 40 wt%, both detectivity and responsivity decrease. With higher CNT loadings, the percolating path and porosity degree of the composite may be improved, and carrier concentrations become higher. Depending on our measured Seebeck coefficients of different SWCNT loadings, the trend of Seebeck coefficients matches our responsivity results. As a result,

the thermoelectric conversion efficiency decreases[135]. For the Si-based detectors, the CNT concentration is quantified using growth time using PECVD (**Figure 4-4 (d)**). In comparison, the detector of 30 min CNT growth matches a higher photoresponse. The detector of 15 min CNT growth may show a lower CNT concentration and the absorption does not reach a saturation status. Although the detector of 45 min CNT growth shows a much higher CNT concentration, the CNTF loses the vertical orientation and falls, which may reduce the IR absorption.

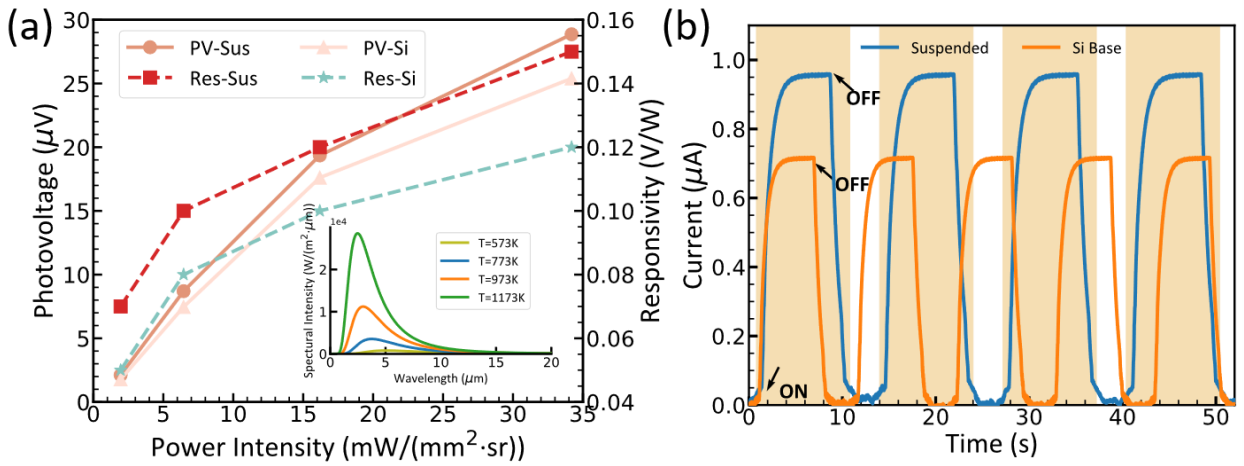

Figure 4-6. (a) Photovoltage and responsivity under different blackbody power intensity. The inset picture shows the spectral power intensities change with various wavelengths under different temperatures. (b) The photocurrent varies with blackbody radiation on and off. The blue line expresses the flexible suspended detector, but the red line expresses the Si-based detector. The current on/off ratio for suspended detector and Si-based detector is 2.0×10^4 and 5.7×10^4, respectively.

Source power intensity also affects the photovoltage and responsivity performance of PTE detectors. **Figure 4-6 (a)** shows the photodetector responses under various radiation conditions, and the photovoltage and responsivity have a similar upward trend. When the temperature of blackbody radiation was set at 573 K, 773 K, 973 K and 1173 K, the power intensity received by our detectors increases from 2.0 mW/(sr·mm^2) to 34.0 mW/(sr·mm^2). With higher power intensities, the illumination induces more hot carriers within the composite, resulting in higher

photovoltages and responsivities[107]. Response time, as another crucial figure of merit, is used to evaluate the speed of a detector. Periodical blackbody radiation was globally illuminated on the PTE detector, and real-time photocurrent was measured. As seen in **Figure 4-6 (b),** the stable photoresponses of the suspended detector are reproducible, and the maximum photocurrent of the free-standing SWCNT/PEDOT:PSS PTE detector can reach 0.95 μA. Furthermore, the rise time and decay time were measured as 0.788 s and 0.376 s, respectively. In comparison, the Si-based PTE detector showed a faster rise and decay time of 0.652 s and 0.353s, respectively, which may result from the enhanced channel length and effective IR absorption. Our detector can show a relatively fast speed, which provides opportunities for further optoelectrical applications.

4.5. Non-contact monitoring of ocular blinking

Based on reported clinical and prodromal cases in coronavirus disease 2019 (COVID-19), 11.2% have been demonstrated oculi-related symptoms[136]. Therefore, an urgent demand for real-time ocular tracking is increasing for precautionary measurement. Generally, the ocular sensors mainly monitor temperature changes or motion variations such as the blinking period[137], [138]. Thermal radiation of eyeballs covers the MWIR regime, and frequently used infrared tomography (IRT) can offer accurate temperature results with high resolution[139]. However, IRT is costly and cannot achieve portable real-time monitoring. For motion tracking, the primary goal is to optimize the algorithm and achieve accurate locating and tracking of eyeball[140]. Such design just begins, and the accuracy is relatively low. Compared with these techniques, the emerging PTE detectors come into play at room temperature and self-powered working conditions.

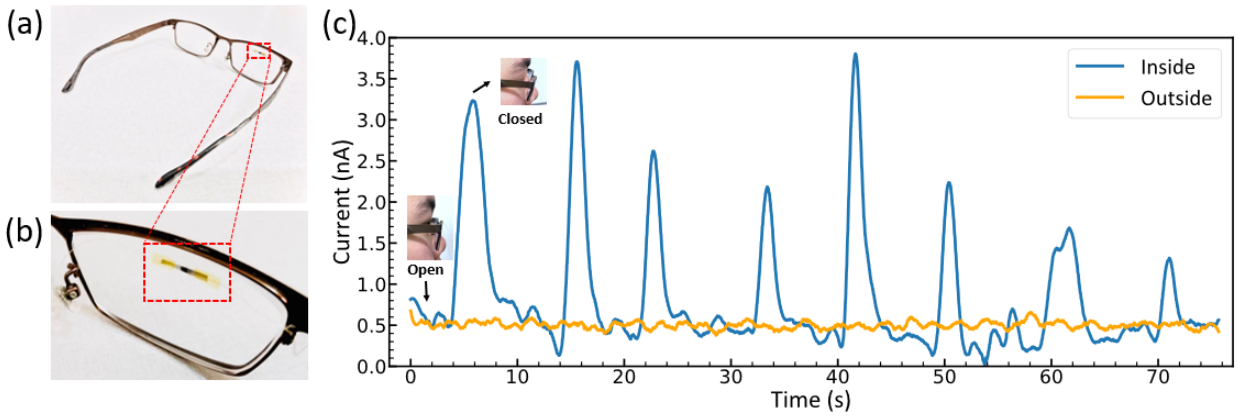

Figure 4-7. (a) The SWCNT/PEDOT:PSS detector is placed onto eyeglasses. (b) Enlarged device onto the eyeglasses lens. (c) Real-time tracking of ocular gestures. The inset pictures are the open or closed status of the eye.

Our SWCNT/PEDOT:PSS PTE detector enabled two potential modes of ocular gesture recognition, including blinking times and periods. As seen in **Figure 4-7,** a photocurrent up to 3.5 nA was observed when our device was placed on the inner side of eyeglasses 8-10 mm away from the eyes. In contrast, the device placed on the outer side cannot detect the blinking signals. It is analyzed that eyeglasses' polymer materials may shield the near-wavelength and mid-wavelength electromagnetic waves, making few MWIR waves reach the device[141], [142]. Moreover, the thickness of lenses is about 3-5 mm, and increasing the distance between eye and device also reduces the response. Additionally, the blinking number of seven within one minute can be obviously seen.

When the eye is closed, the photocurrent is significantly higher. It is assumed that two reasons contribute to this phenomenon. Firstly, the emissivity of the black eyeball is intrinsically weak due to the black colour, which leads to the reduction of MWIR irradiation when the eye is open[143]. Secondly, the thickness of the eyelid of different individuals varies from 2 mm to 4 mm[144]. The reduced distance between detector and eye may lead to a higher current response.

4.6. Non-destructive tracking imaging

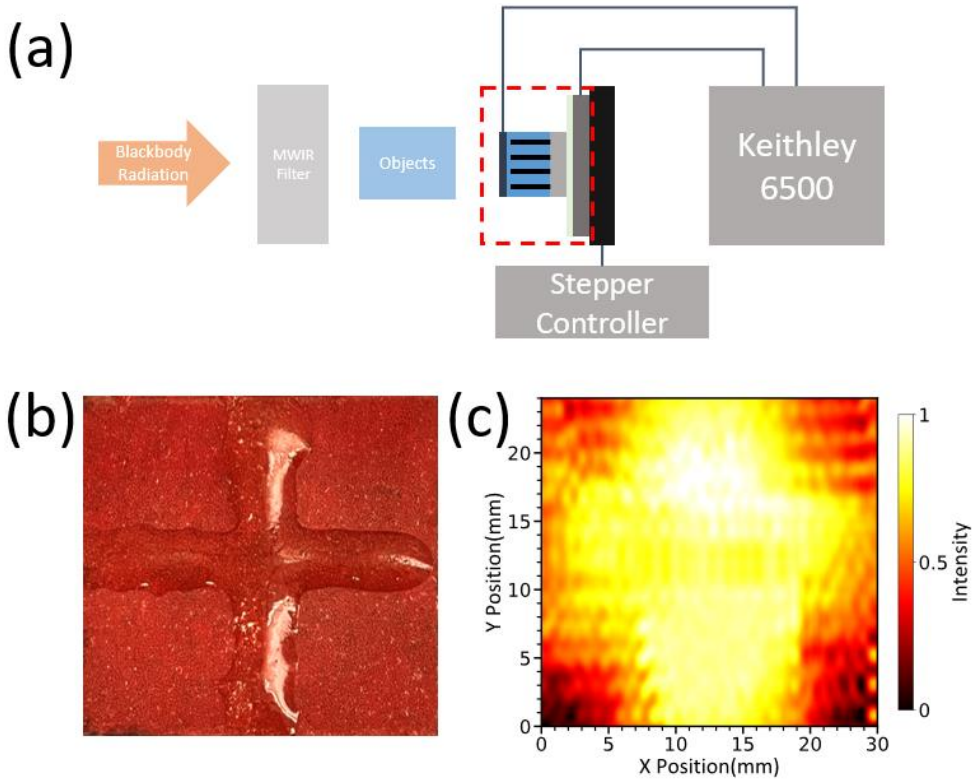

Figure 4-8. (a) NDT system set-up. The red box is the Si-based PTE detector. (b) The crossing photograph. c Photocurrent mapping of the crossing.

NDT experiments are performed to image one crossing glue pattern. **Figure 4-8** illustrates our design of the tracking system. After filtering electromagnetic waves of other regimes, the MWIR blackbody radiation illustrates the objects. The paper and glue have different MWIR absorption, and thus the PTE detector will measure different IR signals. Using the stepper controller, the detectors can move with a 500 μm x- or y-axis step. By mapping the IR current, a crossing pattern of 30 mm×25 mm can be obtained. This experiment can verify the viability of our Si-based PTE detector.

4.7. Stability

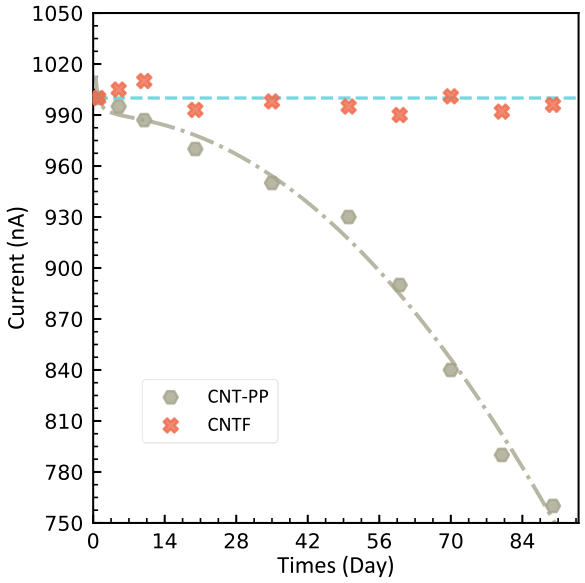

Figure 4-9. Ambient environment stability of suspended SWCNT/PEDOT:PSS composite and Si-based CNTF/PEDOT:PSS PTE detector.

The long-term stability of a detector is crucial to evaluating the device's performance. Given that oxide and water will interact with photodetectors, the stability in the ambient environment is challenging to remain. We tested our suspended device under ambient conditions for over 90 days (**Figure 4-9**). After air exposure for 84 days, our suspended device only has a ~5 % response degeneration, which may originate from the oxidization effects in the ambient conditions. The membrane cracked after 97 days possibly because of residual tension[145]. In comparison, there is no degradation of our Si-based detectors. The performance of both detectors demonstrates that our devices are advantageous in realistic applications.

4.8. Conclusion

This chapter proves two room-temperature PTE detectors for different applications. The non-contact ocular gesture is monitored using the suspended PTE detector based on SWCNT/PEDOT:PSS composite. Stable photoresponse under extreme bending conditions is

tested because of the strong π-π interaction between SWCNTs and PEDOT:PSS. A peak detectivity of 1.9×10^{7} $cmHz^{1/2}W^{-1}$ without bias is achieved under a blackbody radiation source. When the detector is placed onto the eyeglasses about 8-10 mm away from the eyes, a photocurrent variation of 3.5 nA can be observed. The NDT is measured using the CNTF/PEDOT:PSS detectors. The best photocurrent performance can be achieved with a 30 min CNT growth, which may result from the optimized vertical channel length. A photocurrent mapping of the crossing is roughly illustrated. Likewise, both these two detectors achieve relatively long-term stability. Furthermore, the PTE detectors hold huge potential for augmented reality or virtual reality applications, environment management or potential wireless communication on the IoT.

Overall, the performance of proposed PTE detector is competitive and remarkable. Considering the nature of the PTE mechanism, the detectors can be optimized by configuring intricate optical structures, such as antenna integration, plasmonic structure or light absorber[11], [14]. From the viewpoint of thermal physics, the thermal decay length that expresses the thermal dissipation along with the channel is various. If the channel length can be designed similarly or equivalent to the thermal decay length, thermal losses will be tremendously reduced from the internal lattice and the ambient environment[10]. Because mixed metallic and semiconducting CNTs are adopted, the decay length of electron and phonon transport may differ much. Thereupon, the macroscopic tunability measurement of the film is equally important. Additionally, optimizing thermoelectric composite materials towards "Electronic crystal, phonon glass" without reducing photon absorption can also help the device design[146]. For example, given that carriers and phonons of PEDOT:PSS have different transportation speeds, tailoring chain length and crystalline degree of PEDOT:PSS can build up a higher thermoelectric figure of merit[147]. These points are beyond the scope of the current work and will be further investigated.

Chapter 5 The introduction of MXene combined with bottom-up strategy

5.1. Background and motivation

MIR, (2.5-25 μm) detectors that can convert MIR radiation into electrical signals have been employed in many fields[148], such as in digital imaging[149], wearable devices[150], and energy harvesting fields[132], [151]. Presently, commercial MIR detectors mainly adopt traditional mercury cadmium telluride (MCT)[152], gallium arsenide (GaAs)[153], indium antimonide (InSb)[154], or other quantum materials[155], [156]. However, most of these detectors generally suffer from issues such as material toxicity, cryogenic operating condition requirements, strong bandgap dependence, and high-cost fabrication processes[26]. In contrast, PTE detectors combining photothermal and thermoelectric conversion can avoid bandgap dependence and achieve broadband infrared detection at room temperature without external bias[11]. Previously, cadmium sulfide (CdS) crystals[157] or GaAs semiconductors[158] were selected as traditional materials. Unfortunately, their PTE responses are relatively weak, and thus novel PTE materials are urgently needed.

In the last decade, a wide range of PTE materials has been comprehensively reported, such as CNTs[74], [159], graphene[160], [161], and black phosphorus[162]. With high carrier mobility and scalable detection, the emergence of these low-dimensional materials provides guidelines for the miniaturization of on-chip design. However, there are still some significant limitations. For single-layer graphene materials, their gapless band structures endow them with excellent optical properties, but their fabrication processes are comparatively complex and costly[12], [163]. Black phosphorus also shows competitive PTE performance, but its unstable chemical properties make it challenging to use for practical applications[18], [164]. Various CNTs, including single-walled

CNTs, multi-walled CNTs, and CNT-based composites, have been demonstrated to be PTE materials with advantageous photoresponses[71], [104], [108], [159]. However, the armchair or zig-zag directions of CNTs entail complex growth methods and accurate control, which hinders their further development[165]. Our group has summarized the recent progress of PTE materials and proposed the potential of using MXenes for PTE detectors[166].

Composites based on a polymer matrix and low-dimensional nanofillers are advantageous because of their facile fabrication processes. For the matrix, PEDOT:PSS has been verified to have the highest thermoelectric conversion efficiency, with ZT=0.42[119]. It has also been used with other low-dimensional materials to act as an excellent PTE-active composite matrix[167], [168]. In 2016, it was indicated that pristine MXene and MXene-polymer composite films produced an excellent electromagnetic shielding (EMS) effect, demonstrating their photon absorption ability[169]. Furthermore, as a state-of-the-art EMS material, multiple reflection and absorption mechanisms convert the absorbed photons into thermal energy inside the MXene material. Then, in 2017, inspired by the abovementioned electromagnetic wave absorption, Li et al. substantiated MXene's light-to-heat conversion ability of 100%[170]. In 2020, Guan et al. studied the thermoelectric properties of MXene and polymer composite membranes[171]. By incorporating the n-type $Ti_3C_2T_x$ into PEDOT:PSS, the Seebeck coefficient of the composite increased from 23 to 57.3 μV/K[171]. Therefore, MXene and polymer composite materials should be ideal candidates for broadband PTE detectors.

In this chapter, a scalable sensitive MIR PTE detector utilizing an MXene/PEDOT:PSS composite is proposed. Due to the strong absorption and multiple reflection mechanism of MXene, the PTE performance is also enhanced. A broadband photoresponse with a varying spectral range from 2.5 μm to 25 μm and a peak responsivity of 0.12 V/W at 4.5 μm are measured for the MXene-

based PTE detector. Many PTE engineering strategies and optimization methods are investigated, such as electrode choices and vacuum conditions. Also, a complementary SRR metamaterial is integrated into the composite PTE detector. The detector shows a photocurrent enhancement and characteristic noncontact fingertip radiation response measurements, which offers the potential for future realistic health monitoring.

5.2. Device Fabrication

First, 0.1 g of Ti_3C_2 powder is weighed and the powder is added to 6.0 mL organic solvent DMSO. Then, the solution will be operated under magnetron stirring of 1000 rpm for 3 hrs, bath sonication for 60 min, and centrifugation of 1500 rpm for 10 min, followed by the separation of supernatant and sediment. Next, add deionized water (DI) water and centrifuge the mixed solution, and repeat this process for four rounds. The supernatant is separated into another vial. Next, PEDOT:PSS and DMSO solution are added into the vial overnight to obtain the $Ti_3C_2T_x$/PEDOT:PSS mixed solution, followed by magnetic stirring overnight. The composite solution can remain stable for about two days.

The ITO-coated glasses of 10 mm*10 mm are cleaned by using acetone, isopropanol (IPA), and DI water in bath sonication each for 15 min, followed by N_2 drying. Then, the glasses are put on the hotplate at 100 °C for 30 min to dehydrate the surface. Next, spin coat 0.2 mL PEDOT:PSS solution on the ITO layer, followed by baking at 100 °C for 2 min. After the PEDOT:PSS membrane is dried and formed. 0.05 mL $Ti_3C_2T_x$/PEDOT:PSS solution is dropped onto the PEDOT:PSS layer to dry. Finally, the electrodes were then prepared by the sputtering process method on the MXene/PEDOT:PSS film from Al/Au (10 nm/100 nm) layers using a shadow mask. Wires are bonded on the surface of ITO and gold.

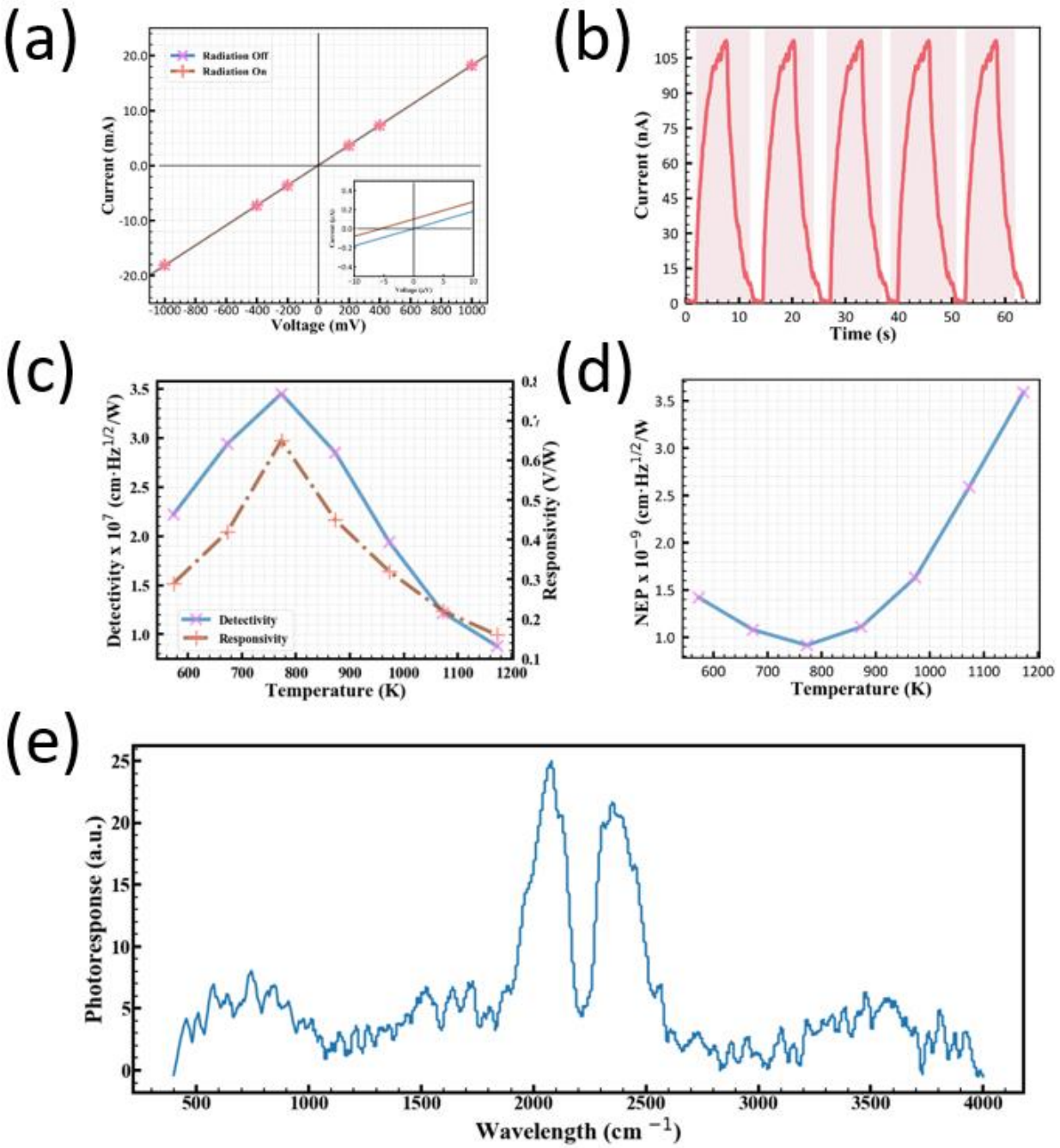

Figure 5-1. (a) I-V characteristics. (b) Response time. (c) Detectivity and responsivity of the detector under different blackbody radiation. (d) NEP dependence on the blackbody radiation temperature. (e) FTIR photocurrent measurement.

5.3. Optoelectrical measurement

The current-voltage (I-V) curves with or without blackbody infrared radiation are presented. The photocurrent is characterized at a blackbody temperature of 773 K without an external bias (**Figure 5-1 (a)**). The linear performance validates the ohmic contact between different layers. With the blackbody temperature at 773 K, when the irradiation is at on or off status, temporal responses exhibit excellent reproducibility for the composite PTE detector placed on the glass substrate (**Figure 5-1 (b)**). The detectivity that characterizes the ability of photon identification from ambient noise is expressed as $D^* = (\frac{V}{P_i})(\frac{\sqrt{s}}{V_t}) = R_V(\frac{\sqrt{s}}{V_t})$, where V represents the photovoltage, P_i is the incident irradiation power, s is the active area, V_t is the thermal noise, and R_V expresses the responsivity[132]. The responsivity and detectivity that correlate with different blackbody radiation temperatures are shown in **Figure 5-1 (c)**. As the blackbody temperature increases from 573 K to 773 K, the photon power density increases simultaneously. The detectivity and responsivity demonstrate a 50% increase. However, the subsequent increase in blackbody temperature causes a reduction in both detectivity and responsivity. The detectivity is ~10^7 Jones, with a peak value of 3.5×10^7 Jones at 2060 cm^{-1}. The enhanced detectivity may contribute to the high infrared absorption and suppressed hot-carrier relaxation of the composite in this regime. NEP is another term for characterizing the sensitivity of the PTE detector and can be defined as $NEP = \frac{\sqrt{A\triangle f}}{D^*}$, where A is the photoactive area and $\triangle f$ is the bandwidth. As seen from **Figure 5-1 (d)**, the NEP first shows an increasing and then decreasing trend, which suits the changing trend of detectivity. This change may partly originate from different absorption spectra. The room-temperature FTIR photocurrent spectrum of the Ti_3C_2/PEDOT:PSS composite is plotted in **Figure 5-1 (e)**. In the PTE mechanism, the thermal Johnson-Nyquist noise level does not correlate with the spectrum. Additionally, hot-carrier-assisted PTE conversion may exist in this vertical MXene composite detector. Due to the small electron thermal conductivity, the electron temperature will

increase faster than the phonon temperature, and thus nonequilibrium temperature transfer may occur. The electron temperature difference induces electron flow. Furthermore, electron flow results in the generation of electron–hole pairs and strong interactions among electrons. The energy absorbed by the MXene composite warms up the carriers. In the two-dimensional material system, the interaction between electrons and phonons is significantly suppressed, and thus, the hot carriers mainly facilitate the PTE conversion. By optimizing the material design, this vertical detector's response time may be significantly enhanced.

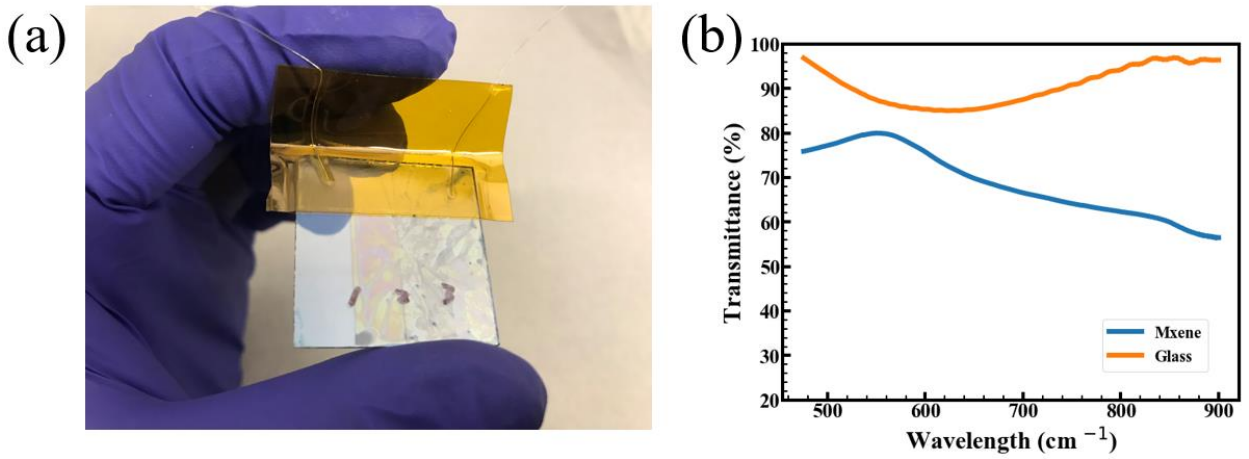

Figure 5-2. (a) Photographic imaging of semi-transparent PTE detector based on ITO/(Ti_3C_2/PEDOT:PSS)@PEDOT:PSS/ITO. (b) UV-Vis spectrum during 475-900 nm regime.

Additionally, a thin semitransparent Ti_3C_2/PEDOT:PSS film can be obtained by utilizing the spin-coating method. By combining two transparent ITO electrodes and a spin-coated composite thin film, the whole device is configured as ITO/(Ti_3C_2/PEDOT:PSS)@PEDOT:PSS/ITO. The photographic image and UV–Vis transmittance spectrum are shown in **Figure 5-2**. In a low-dimensional material system, flake agglomeration is a major issue, which causes nonuniformity and further hinders transparency enhancement. A reasonable mitigation solution is lowering the speed of spin coating. Additionally, additional substrate cleaning steps, such as ozone addressing,

are beneficial.

5.4. PTE engineering strategies

As the micro/nanofiller in this composite, the MXene flake size may affect the optoelectrical properties and even the PTE effect. As shown in **Figure 5-3**, tip sonication can cut the MXene

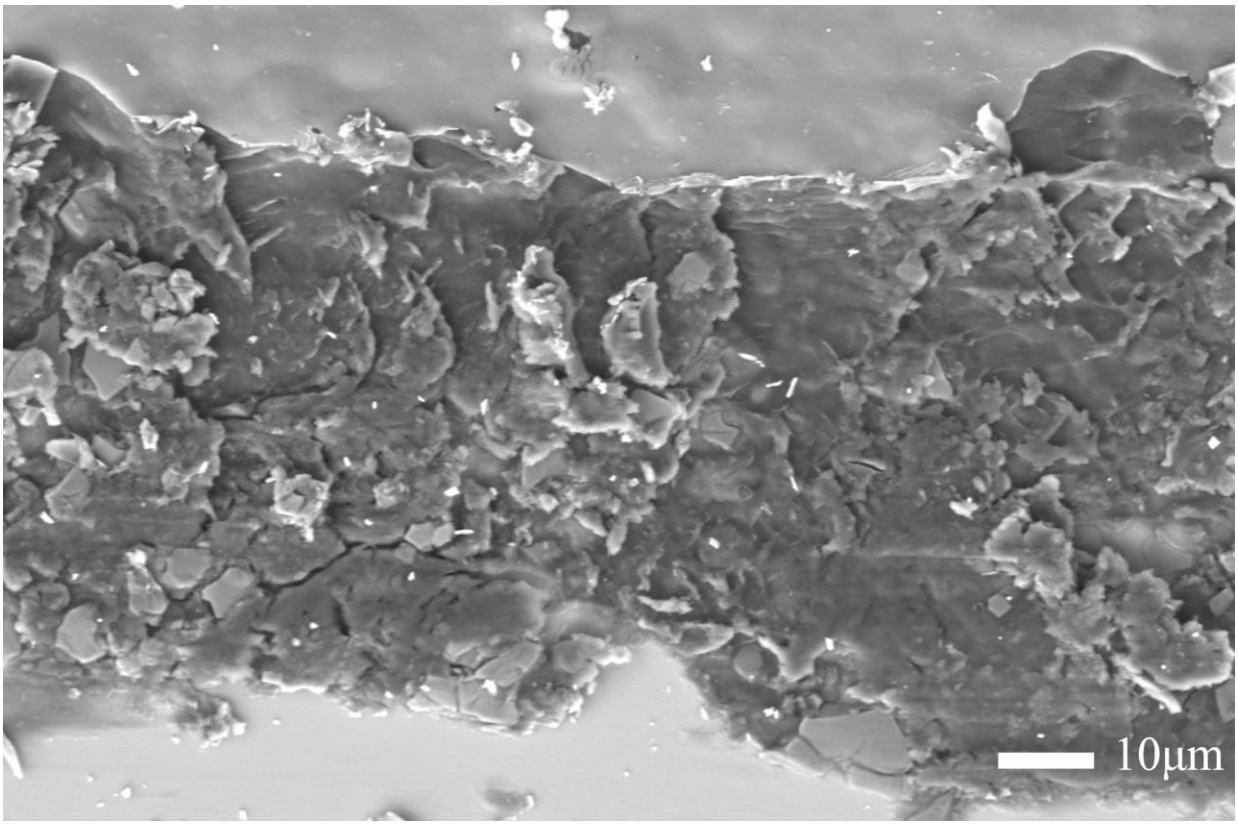

Figure 5-3. MXene flake pieces.

flake into small pieces. According to the modified sonication time, the MXene size also changes, which matches previous research results[171]. With increasing sonication time, the MXene size decreases, and conductive path damage occurs between MXene and the polymer (**Figure 5-4 (a)**). Although the conductive network is easier to form, the resistivity inevitably increases. Overall, excellent thermoelectric properties or PTE effects originate from proper MXene size, PEDOT:PSS

concentration, and their coupling effect[171]. However, high sonication power may cause

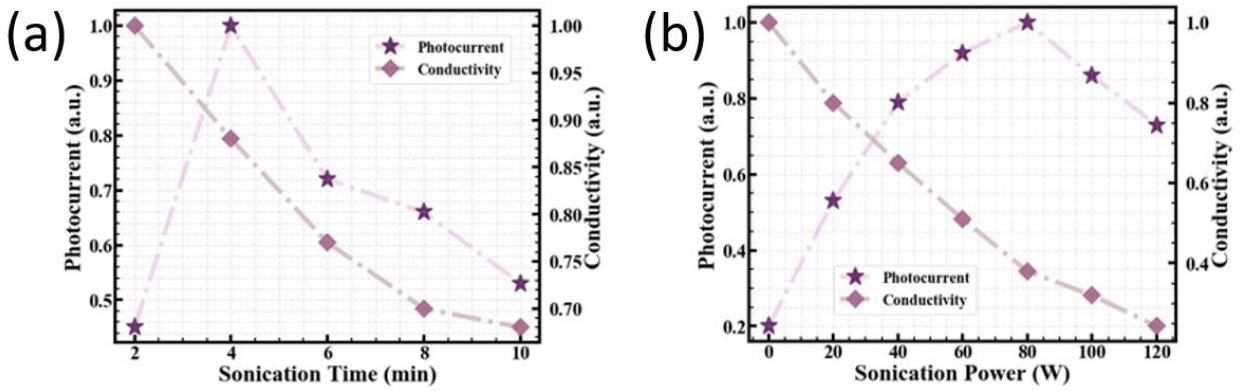

Figure 5-4. (a) Sonication time. (b) Sonication power.

localized thermal accumulation, damaging the bonding interaction between PEDOT and PSS and further hindering the conductivity and PTE response (**Figure 5-4 (b)**).

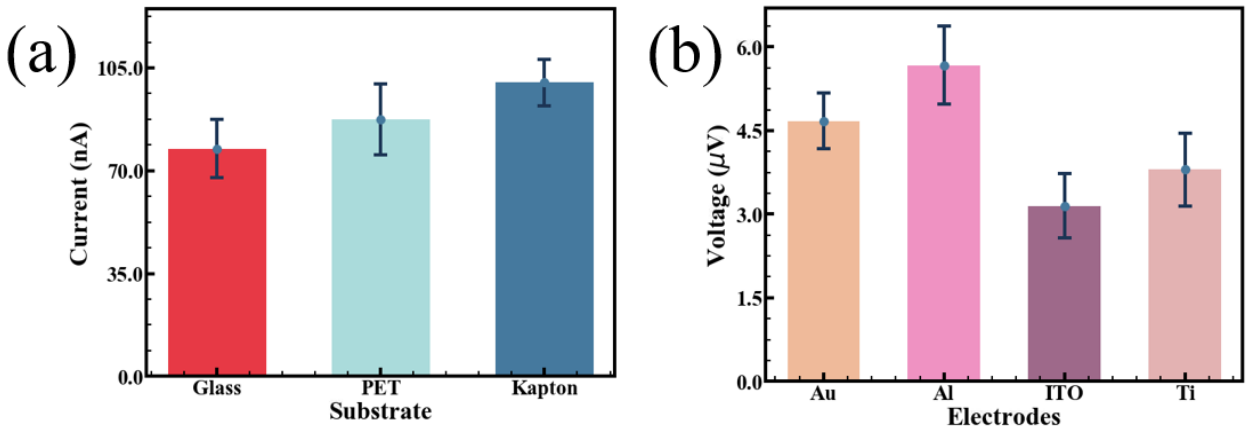

Figure 5-5. (a) Substrate. (b) Electrode.

The substrate experiment was also carried out at room temperature, and the top of the substrate was selected as the ITO/(MXene/PEDOT:PSS)/PEDOT:PSS/ITO structure. Notably, thermal dissipation occurs between the active layer and substrate, and thus, the thermal conductivity of the substrate is critical. As seen in **Figure 5-5 (a)**, polyimide shows the highest response in the

substrate-based device because it shows the lowest thermal conductivity (k=0.12 W/mK) compared with glass (k=1.05 W/mK) and polyethylene terephthalate (PET, k=0.3 W/mK).

Four top electrode materials are prepared, including ITO, Al, Ti, and Au. In this optimization design, the thickness of the electrode is controlled down to 20 nm. The reason for selecting this value refers to the skin limit. The electrode thickness of 20 nm is smaller than the skin limit in the infrared spectrum. The photoresponse ranking of these matched materials is Al>Au≈Ti>ITO (**Figure 5-5 (b)**), which matches the previous results[68]. Al shows the best photoresponse, but the Al electrode is prone to oxidization, which influences the conductivity and even the PTE response. Although gold shows a relatively weaker photoresponse than Al, it can be

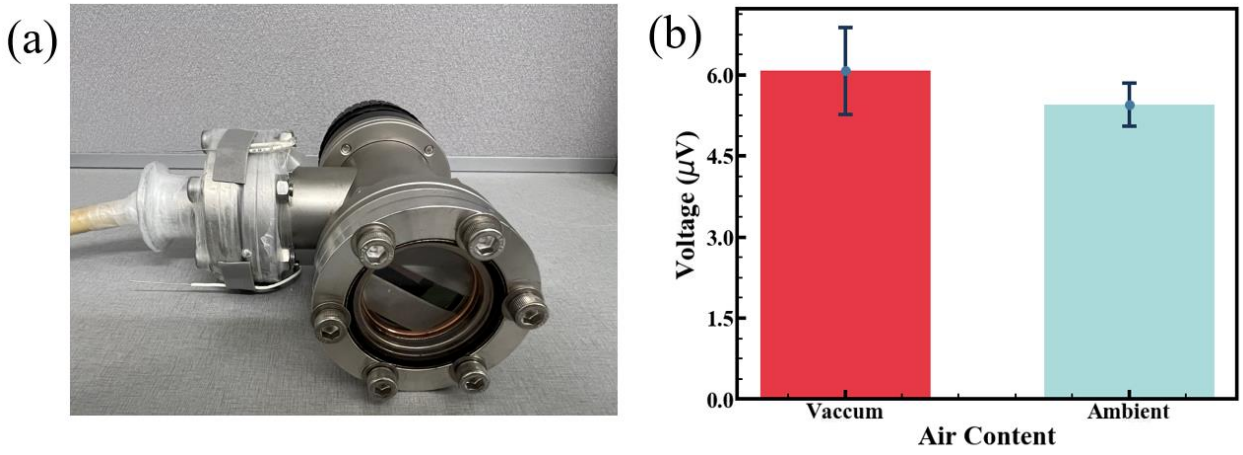

Figure 5-6. (a) Detector inside the vacuum chamber. (b) Vacuum conditions.

designed as a metamaterial[172]. Ti can demonstrate better adhesion with the substrate and photoactive layer because the photoactive layer $Ti_3C_2T_x$ is also an enriched Ti-element material. In contrast, ITO can provide transparent properties, which benefits other wearable devices or the Internet of Things (IoT). Therefore, a trade-off is required when electrode materials are adopted.

Given that the PTE effect is a thermal-based mechanism, the influence of ambient air contents

is investigated on the detector photoresponse. The detector is installed inside the chamber and near the window (**Figure 5-6 (a)**). The blackbody radiation source is set up at 773 K and approximately 20 cm away from the detector. As seen in **Figure 5-6 (b)**, the photocurrent increases by 20%, and only a small variation in the response time appears. This may originate from the reduced thermal loss to the environment, i.e., more energy can be converted from light energy into heat, which improves the first-step conversion efficiency of the PTE effect. This vacuum-enhanced photoresponse helps maintain long-term stability. Furthermore, allowing for the configuration of the PTE detector and controlling the vacuum conditions of different components, such as electrodes and channels, may benefit the performance of the PTE detector.

Furthermore, E-beam and magnetic sputtering are adopted as two methods to deposit 20 nm

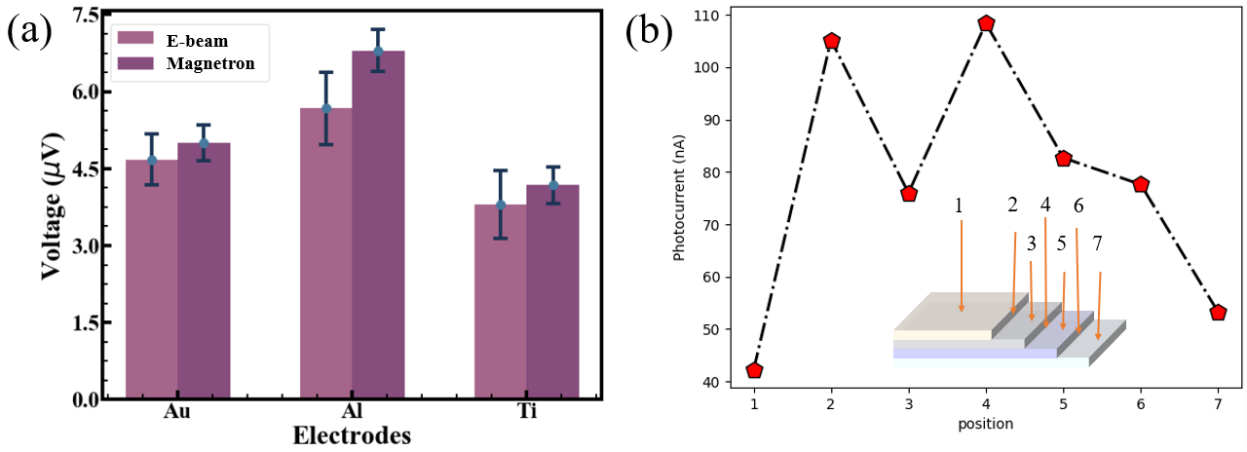

Figure 5-7. (a) Electrode deposition methods. (b) Illumination position.

electrodes (**Figure 5-7 (a)**). The device using sputtering strategies shows approximately 5%-15% higher performance than that using E-beam deposition. Generally, magnetic sputtering can demonstrate a higher uniformity and film density than E-beams, which further affects the mechanical, electrical, and thermal contacts[173], eventually improving the performance of PTE detectors.

Additionally, the illumination position dependence on the PTE response is studied. This experiment was performed under ambient conditions at room temperature. The results can be understood according to previous research theory[8], [104]. Within the PTE configuration, the PTE response induced by radiation at different positions is given by PTE=$(S_1-S_2)(T_1-T_2)$, where S_1 or S_2 represents the Seebeck coefficients of adjacent layers, and T_1 or T_2 represents the real-time temperature. **Figure 5-7 (b)** shows the photocurrent performance at different positions. The results show that the PTE response mainly occurs at the interface. The difference in Seebeck coefficients between adjacent material interfaces plays an important role in the PTE response. The interfaces between PEDOT:PSS and the composite show approximately 30.0 μV/K and a 0.1 K temperature difference, resulting in a 3.0 μV photovoltage. The photovoltage between the two interfaces exhibits an evident reduction.

5.5. Metamaterial Fabrication and design

Metamaterial design, as a method of improving electromagnetic absorption, can play an important role in designing PTE detectors. For the PTE detector integrated with metamaterial, the fabrication process is listed below. (1) A glass slide of 102 mm*83.2 mm is cleaned by piranha wetbench (H_2SO_4:H_2O_2=4:1) for 15 min. DI water rinsed the surface and N_2 is used for drying; (2) acetone, IPA, and DI water are used to clean the surface, followed by hotplate prebaking at 150 °C for 10 min; (3) after it cooled down, use ozone system to address the surface; (4) spin-coat PMGI at 5000 rpm and ramp down at 500 rpm/s, followed by Fisher oven prebaking at 150 °C for 25 min; (5) spin-coat Shirpley1805 at 5000 rpm and ramp down at 500 rpm/s, followed by Fisher oven prebaking at 115 °C for 25 min; (6) MLA is used for creating the metamaterials pattern with a dose of 82 mJ/cm^2, followed by the immersion of the MF-319 development solution for 70 s; (7) 10 nm Ti/80 nm gold is deposited by Angstrom E-beam, and lift-off process is carried out using

acetone with gentle sonication, followed by IPA cleaning and gentle N_2 drying; (8) spin-coat Shirpley1811 at 5000 rpm and ramp down at 500 rpm/s, followed by Fisher oven prebaking at 115 °C for 25 min. This photoresist is used for creating an insulator interface to prevent the short-circuit phenomenon. (9) MLA is used for creating the Al electrode pattern with a dose of 82 mJ/cm^2, followed by the immersion of the MF-319 development solution for 70 s; (10) spin-coat PEDOT:PSS at 6000rpm and ramp down at 500 rpm/s, followed by 30°C baking for 60min in the fume hood; (11) drop-cast MXene/PEDOT:PSS solution of 100μL at room temperature overnight

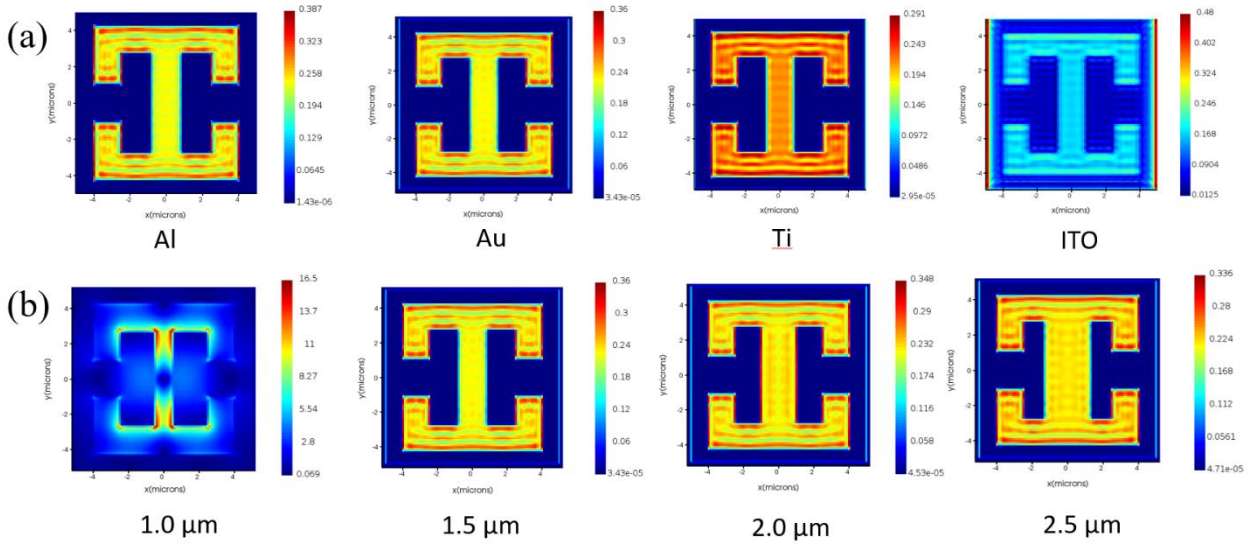

Figure 5-8. (a) Electromagnetic simulation results using Al, Au, Ti, and ITO. (b) Electromagnetic simulation results with different hole sizes of 1.0, 1.5, 2.0, and 2.5 μm. The metamaterial adopts gold.

in the fume hood. The high temperature will cause the formation of bubbles between the active layer and glass, and thus set up the room temperature for drying the thin film; (12) the Al electrode of 150 nm is deposited using the PET mask fabricated by laser cutting machine; (13) put the array device into the acetone for 5min and use IPA for cleaning the surface; (14) wire-bond aluminum wires to the gold and Al pad using conductive silvery glue. The array circuit is completed by the

laser-induced mask fabrication technique that is reported by Ref. [31].

Different metamaterials are simulated, including Al, Au, Ti, and ITO **(Figure 5-8 (a))**. All the electromagnetic field intensities using these four materials improve. Thus, in specific applications,

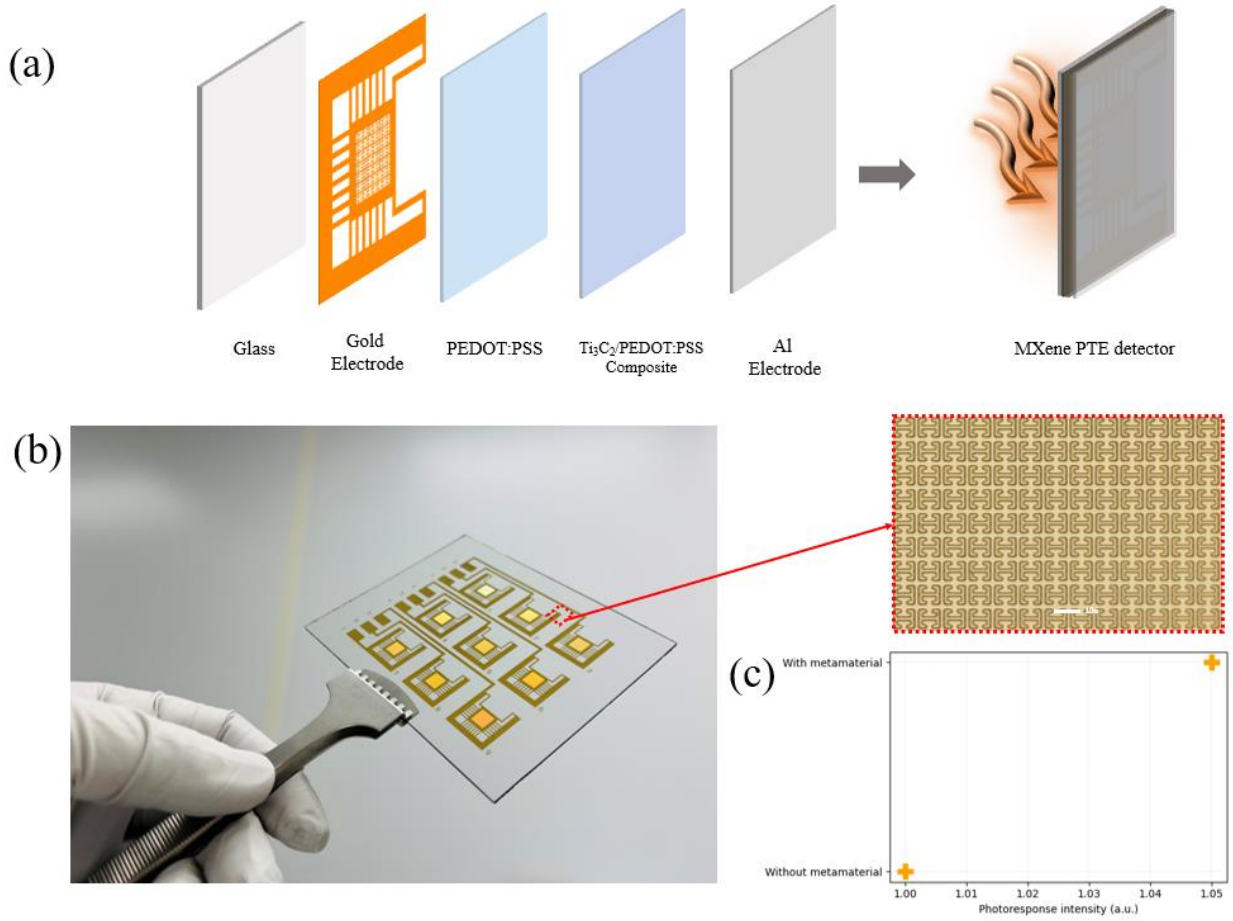

Figure 5-9. (a) The fabrication process of the PTE detector integrated with metamaterial design. (b) Optical imaging of metamaterials on glass. The red square is the enlarged photographic metamaterial imaging. c Photocurrent enhancement with or without metamaterial.

There are other factors to consider, such as fabrication processes that are compatible with typical metal materials. Additionally, Al and Ti may be easily oxidized, but they are inexpensive. The price of Au is expensive, but its conductivity is higher than others. ITO can show high

transparency. By using the gold metamaterial, different channel sizes are also simulated, including 1.0 μm, 1.5 μm, 2.0 μm, and 2.5 μm. A simulated electromagnetic enhancement can be seen in **Figure 5-8 (b)**. Although the metamaterial with a 1.0 μm channel size shows the strongest field enhancement, maskless alignment (MLA) usually shows a round edge, and pattern resolution degrades considerably. Thus, a channel width of 1.5 μm is selected. Given that the micrometre-level pattern is challenging to fabricate after depositing MXene/PEDOT:PSS film, a bottom-up strategy is used to fabricate this PTE detector (**Figure 5-9 (a)**), and the blackbody radiation will illuminate from the glass direction. Next, the fabrication process of the metamaterial is presented. A gold metamaterial structure is fabricated on the top of the glass substrate by MLA, E-beam deposition, and a lift-off process. Then, PEDOT:PSS is spin-coated to improve the adhesion between the gold electrode and MXene composite. Next, the MXene/PEDOT:PSS composite is drop-cast on each pixel. Finally, Al electrodes are deposited, followed by aluminum wire bonding. Using this fabrication strategy, the metamaterial surface can be protected, and the PTE detector can achieve long-term stability. As seen from **Figure 5-9 (c)**, the measured responsivity can show a 5% enhancement by integrating this metamaterial structure.

5.6. Non-contact fingertip signal tracking

Pandemic respiratory syndrome coronavirus 2 has had severe effects around the world. The causative agent of coronavirus disease can spread via respiratory droplets and close contacts, such as through elevator buttons or restroom faucets[174]. Therefore, noncontact finger-sensing devices are urgently needed to prevent the spread of this novel coronavirus. Compared to direct contact sensors, self-powered novel infrared sensors can be controlled in a noncontact way through infrared response changes, thus avoiding mechanical touch and bacterial transmission. Importantly, infrared sensors can efficiently utilize human passive radiation to collect information and achieve

relatively long-distance signal control, which would be a potential control method in advanced

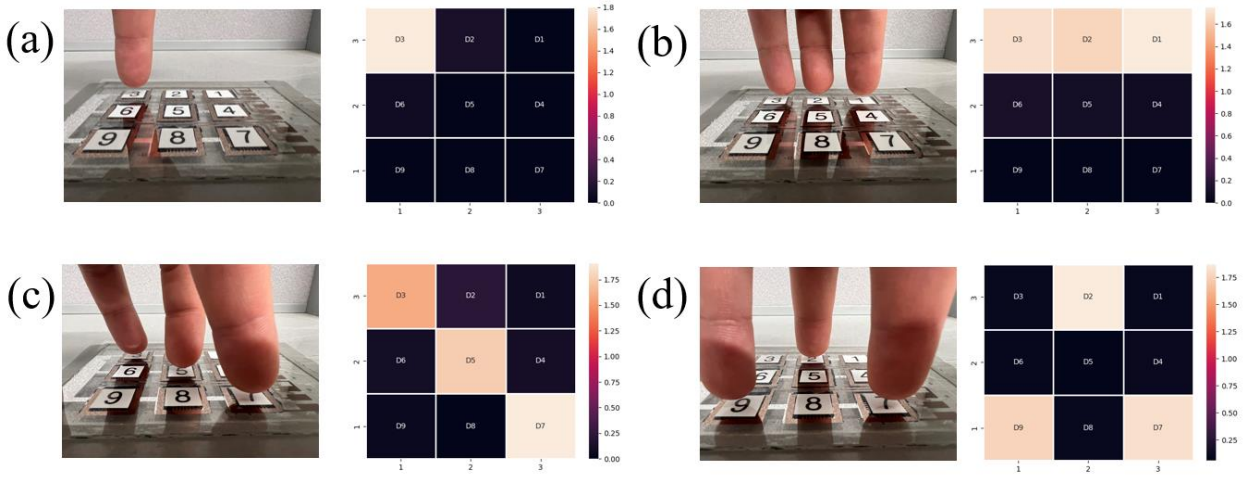

Figure 5-10. (a) , (b), (c), (d) Fingertips are placed on the top of "D3", "D3, D2, D1", "D3, D5, D7", and "D2, D7, D9", respectively. The fingertips are placed 2 mm away from the glass layer. The color bar indicates the intensity of the photovoltage. The "D1", "D2", "D3", "D4", "D5", "D6", "D7", "D8", and "D9" labels match the device number from 1 to 9.

human-machine interactions.

The human fingertip response is tested and recorded the photovoltage change of nine pixels by inserting a 2001-TCSCAN card into a Keithley DMM-6500 to achieve a multichannel measurement. As seen in **Figure 5-10 (a)-(d)**, different positions are tested and the fingertip radiation measurement are performed. Different shapes demonstrated the noncontact radiation tracking viability of this detector.

5.7. Conclusion

This chapter presents a scalable broadband PTE detector based on MXene and a polymer composite and discusses its PTE mechanism. The morphology and photoresponse performance of the composite are proposed. The strong absorption and excellent percolation conductive network

of the Ti_3C_2/PEDOT:PSS composite are beneficial for the PTE effect. As a result, this PTE detector shows broadband absorption varying from 2.5 μm to 25.0 μm, with a peak detectivity of 3.5 Jones at a 773 K blackbody temperature. Additionally, some key factors of PTE engineering are explored, such as electrodes and substrates. The results demonstrate that the electrodes using aluminum and sputtering methods showed a higher photocurrent. The larger thermal conductivity significantly suppressed the PTE response. The device sealed in a high-vacuum environment exhibits better optical performance. To further enhance the photoresponse in this vertical PTE configuration, the gold metamaterials is integrated into the detector utilizing the MXene/PEDOT:PSS composite. Finally, the noncontact fingertip response application is verified. Although this research is only a proof-of-concept model, it can be foreseen that this instructional material and structural engineering design will play a prominent role in wearable applications. Furthermore, PTE detectors take advantage of noncontact monitoring properties, so real-time human gestures utilizing PTE detectors can be effectively monitored. Additionally, typical radiation regimes, such as terahertz radiation, exhibit nondestructive properties, and thus, future active or passive nondestructive tracking for airport security may also utilize PTE detectors.

Chapter 6 Packaged PTE detectors

5.1. Background and motivation

With the development of artificial intelligence and interactive technology, smart sensors and the IoT enter the mainstream markets because of their excellent chemical and physical properties[58], [175]–[178]. Typically, IR-based technology attracted significant attention because the corresponding spectrum of matter (including transmission and reflection spectra) contains rich physical and chemical information[179]. As an emerging IR thermal detector, the PTE detectors combining photothermal and thermoelectric conversion can ignore the bandgap limitations and achieve effective IR detection[8], [38]. They can operate at ambient conditions without bias, and show convenient and safe manufacturing processes[180].

Composed of metal electrodes and active layers, the research of PTE detectors mostly focuses on several fixed structures utilizing various active materials. Previously, the researcher explores traditional silicon-based nanowires but shows a relatively long response time and poor infrared absorption[53], [181]. The PTE detectors based on multi-layer graphene also show similar issues[15]. Additionally, the unstable ambient properties of black phosphorus and the toxic Pb element of perovskite also limit extended research[182]. Polymer-based composites face the challenges of low infrared absorption and temperature endurance[104]. Since the discovery of MXene by Yury Gogotsi in 2011[81], numerous research about the related synthesis and applications have been demonstrated[183]–[186]. Typically, MXenes show typical optoelectrical properties because of their competitive photonic phenomenon and high carrier mobility[187], [188] as well as the thermoelectric capacity of MXene demonstrated by Kim et al.[189], which can be utilized as an advantageous active PTE material or electrodes. As the most comprehensively

studied PTE materials, types of CNTs show ordered growth control, facile synthesis methods, and excellent PTE properties[9], [73], [76], [80].

However, there exist some other challengings with current PTE detectors. First, current vertical PTE detectors mainly use metals as top electrodes. However, the thickness of metal electrodes usually is smaller than 100 nm on account of the skin effect. Such thin thicknesses of metal electrodes may significantly influence the conductivity. Additionally, the existence of top metal electrodes will reduce infrared absorption[68]. Thus, the alternative electrode materials of vertical PTE detectors wait to be explored. Second, PTE detectors inside the vacuum environment have demonstrated enhanced PTE response[47]. The vacuum conditions may potentially reduce the degradation and increase the stability and durability of devices. However, current vacuum systems of PTE detectors depend on cumbersome vacuum chambers, and integrated vacuum PTE detectors are urgently required. Third, current PTE detectors based on low-dimensional materials like CNTs, graphene and black phosphorus, are sensitive to light polarization[38], [103], [190]. Some of the PTE detectors that are insensitive to light polarization make use of random internal atom orders of the composite film[15], [80], [191]. However, it is challenging to control the size of the detectors and achieve sensor miniaturization, eventually hindering their future smart wearable integration.

In this chapter, a self-powered sensitive PTE detector is fabricated to solve the abovementioned problems utilizing the vertical CNTF as the active layer and MXenes as the top electrodes. The non-metal electrodes are first reported to be applied for PTE detectors. The photoresponse using Ti_3C_2 and Mo_2C top electrodes are investigated, respectively. The electrode thickness of top MXene electrodes is also studied. A thinner MXene electrode using the drop-cast method will match a better PTE response. The potential reasons may attribute to the electromagnetic shielding effect with a thicker electrode. Thus, the control of reasonable electrode types and thickness may

be important. PTE detector also encapsulates with polytetrafluoroethylene (PTFE), suppressing the degradation and enhancing the PTE response. The packaged system is also applied to NDT imaging. A photovoltage imaging pattern is illustrated, which demonstrates the imaging capacity of PTE detectors.

5.2. Device design and fabrication

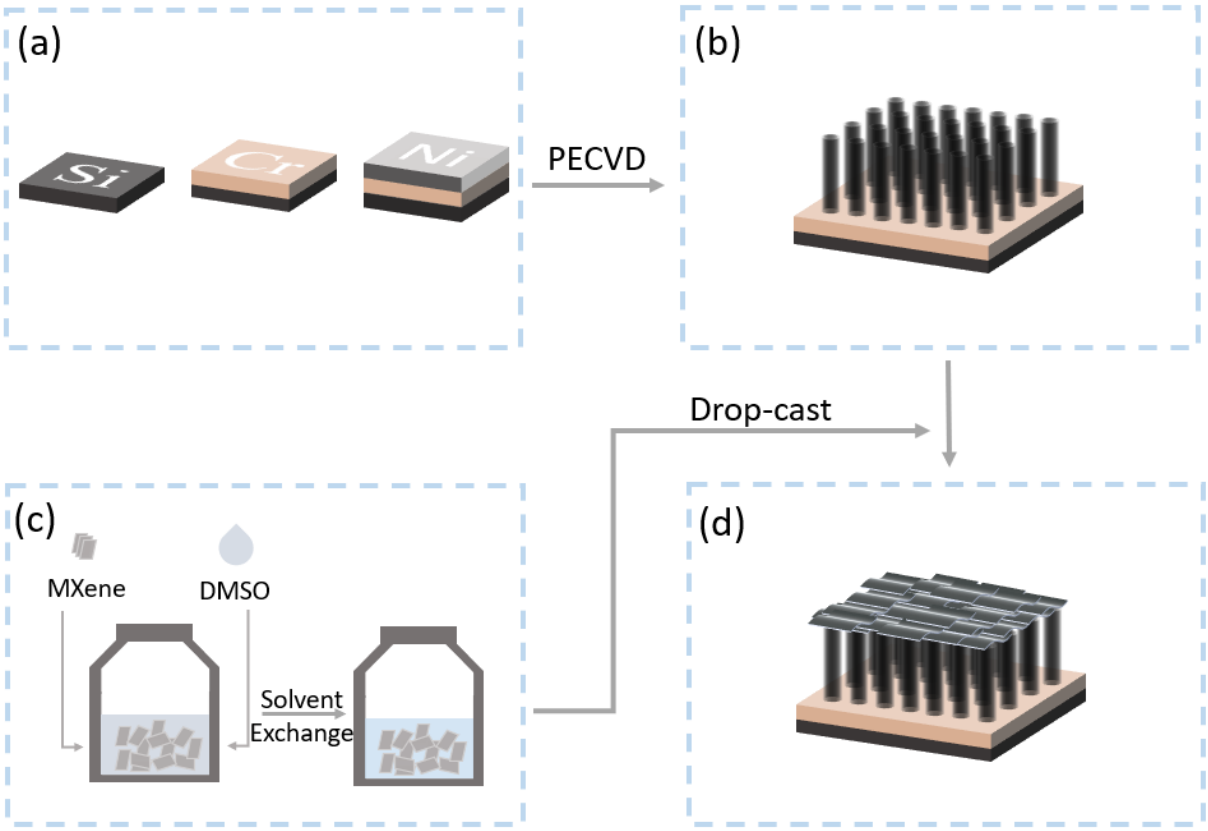

Figure 6-1. Fabrication process of PTE detector. (a) Prepare for Cr buffer layer and Ni catalyst layer on Si substrate. (b) CNT growth on Si substrate. (c) Preparation of MXene solution. (d) Detector illustration.

Ti_3C_2 solution: the solvent exchange method is adopted to obtain the uniform Ti_3C_2 solution. A 0.15 g of Ti_3C_2 or Mo_2C powder is firstly added into 6.0 mL DMSO solution, followed by 24 hrs

magnetron stirring of 1500 rpm. Then, the solution will be centrifuged at 5000 rpm for 5 min. The top clear solution is removed and replaced by DI water. This replacement process will repeat five times until the pH value of the Ti_3C_2 solution reaches about 7.0. The Ti_3C_2 or Mo_2C solution is stored under nitrogen conditions.

CNTF Fabrication: First, prepare a 4-inch Si prime wafer and clean it by RCA method. In each pixel area, the Cr buffer layer of 100.2 nm and Ni catalyst layer of 19.7 nm is deposited using maskless lithography and the lift-off method in order. Next, CNTF grows using PECVD with C_2H_2 and NH_3 of 200:50 volume ratio at 700 °C and 100 W plasma for 15 min.

The fabrication process of the Si-based vertical PTE detector is illustrated in **Figure 6-1**. **Figure 6-1 (a)** shows the layer preparation of CNT growth, including the Si substrate, Cr buffer layer, and Ni catalyst layer. The metal Cr plays ternary roles in the PTE cooler, bottom electrode and a catalyst supporting layer, i.e. buffer layer, which can help prevent the diffusion of catalyst particles[192]. The metal Ni acts as the catalyst for CNT growth. The vertical channel of CNTF is designed based on several reasons. According to the internal polarization, the optical absorption of CNTs can be maximized or minimized in different wavelengths. The CNTs grown by CVD show high mobilities and the Seebeck coefficient of semiconducting CNTs can reach 300 μV/K[63]. Also, the coulomb interaction and large binding energy of 1-D materials contribute to the potentially enhanced PTE response[26]. Additionally, the height of CNTs can be controlled similarly to the cooling length of PTE devices, which can maximize the device's performance (**Figure 6-1 (b)**). The MXenes are processed using the low-cost and facile solvent exchange method to exfoliate and delaminate, which can produce better conductivity (**Figure 6-1 (c)**)[193]. After the delamination, the drop-cast MXene electrode can be thinner down to about 0.9 μm measured by Bruker profilometer. The MXenes (Ti_3C_2 or Mo_2C) are drop-casted and dried as the

top electrodes instead of traditional metal electrodes, and then the basic detector structure is illustrated in **Figure 6-1 (d)**.

5.3. Material characterization

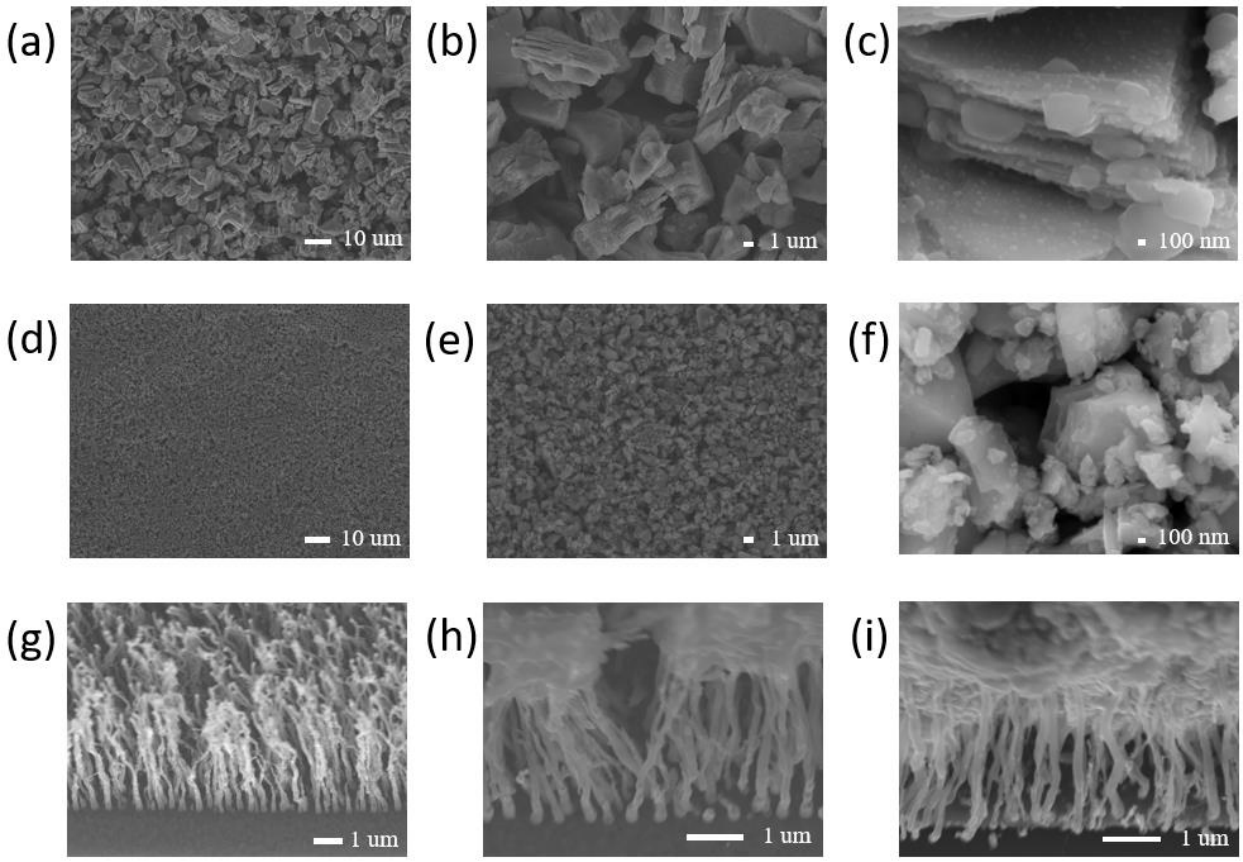

Figure 6-2. Top view of Ti_3C_2 with the scale bar of (a) 10 um, (b) 1 um, and (c) 100 nm. Top view of Mo_2C electrodes with (d) 10 um, (e) 1 um, and (f) 100 nm. (g) The side view of CNTF. The side view of PTE detector with (h) Ti_3C_2 electrodes and (i) Mo_2C electrodes.

Figure 6-2 (a)-(c) shows the scanning electron microscope (SEM) images of the Ti_3C_2 electrode, and **Figure 6-2 (d)-(f)** shows the SEM images of the Mo_2C electrode. MXenes usually present a crossed atomic structure, and their surfaces are usually modified by all types of terminations like -OH and -F, which depend on the synthesis etching method. Both Ti_3C_2 and Mo_2C show layered

stacks and their films are relatively uniform. The thickness of the MXene electrode can be controlled by adjusting the solution concentration or volume. Specific PTE responses related to MXene types and electrodes will be listed in section 2.4. The excellent conductivity of MXene may contribute to the inherent excellent conductivity of the MXene flake and good contact among flakes. The tip-growth CNTF method is used by PECVD, the metal Ni will remain in the tip parts, resulting in a hydrophobic top region[194], [195] (**Figure 6-2 (g)**). Water molecules will evaporate and may not flow into the CNTF, so the alignment of CNTF may not change. This drop-cast method will produce a random orientation distribution and relatively rough MXene surface, which may potentially enhance infrared absorption (**Figure 6-2 (h) and (i)**).

5.4. Photoresponse mechanism and characterization

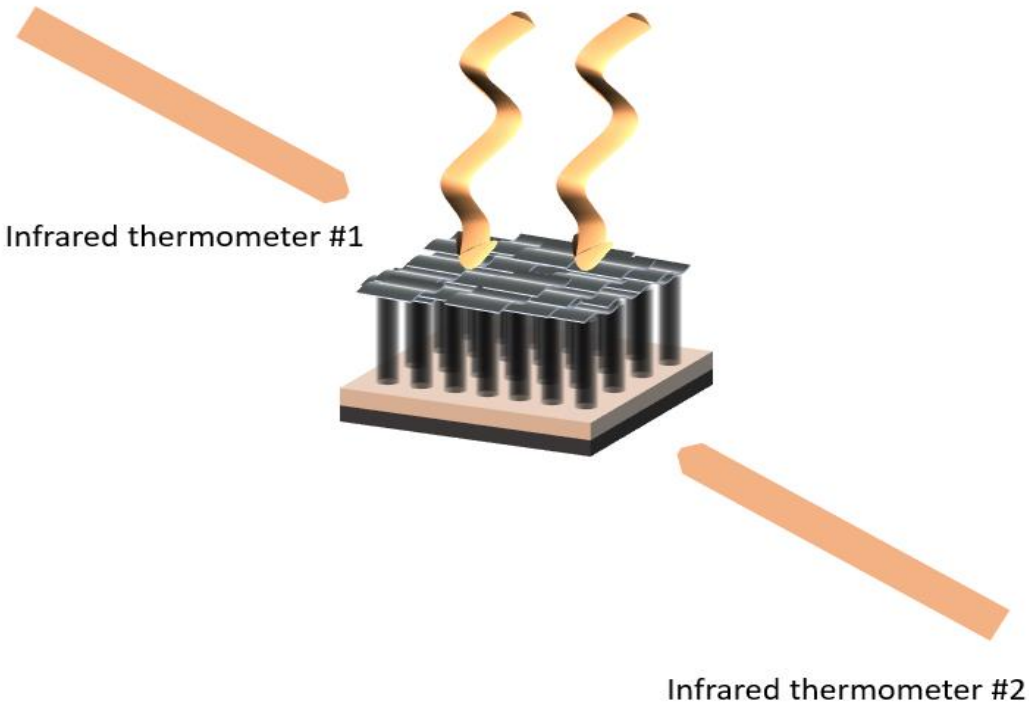

Figure 6-3. The illustration of temperature measurement by infrared thermometer.

When the illumination irradiates on the top of the MXene electrodes. The infrared radiation is mainly absorbed by the top MXene electrode. The remaining parts may be absorbed by CNTF. The top electrode of n-type MXene is heated and acts as the heat source. A temperature difference is created through the vertical direction. The bottom Cr electrode acts as the heat sink. The n-type carriers (electrons) transport to the cold bottom Cr electrode and the p-type carriers (holes) transport from the bottom to the top heated electrode.

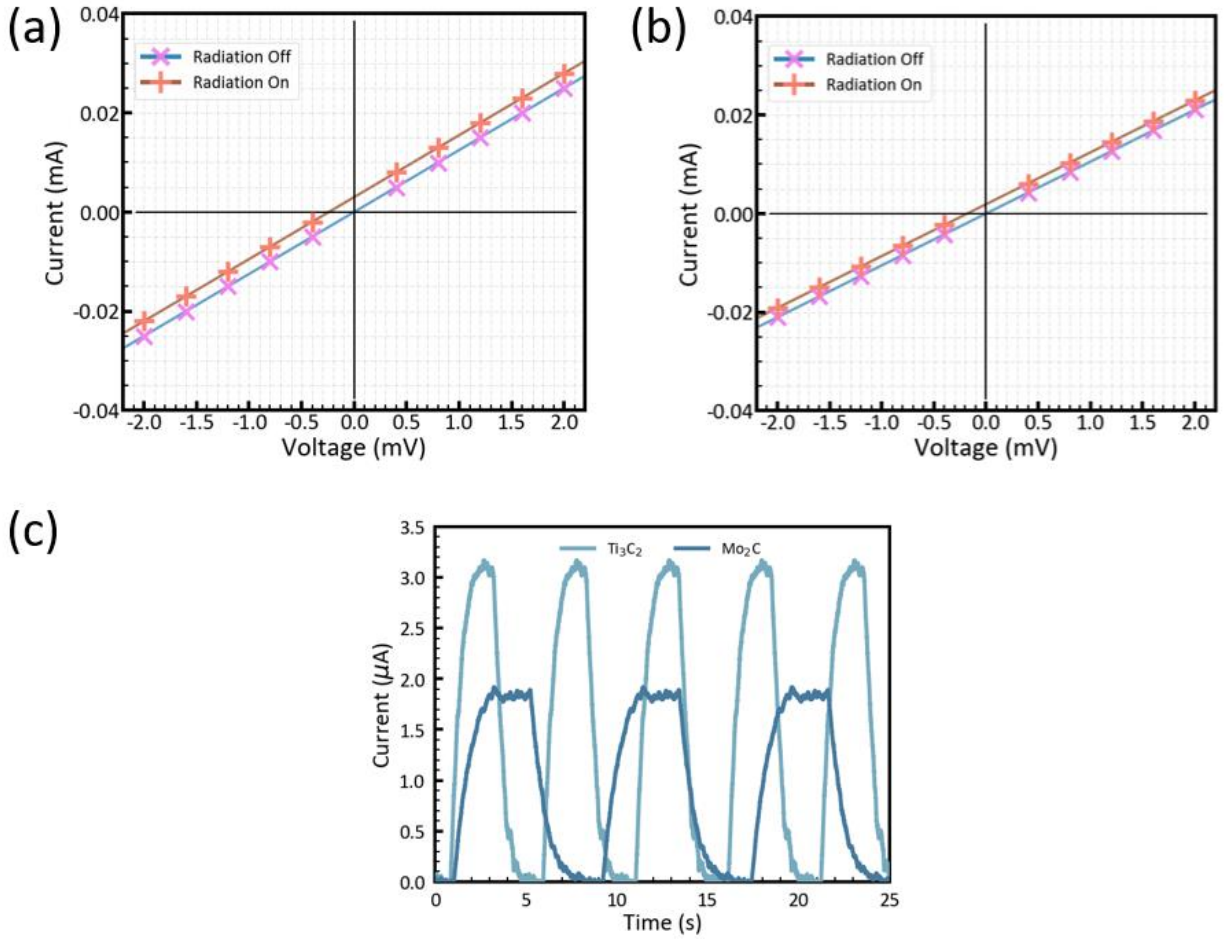

Figure 6-4. I-V curve of PTE detectors with (a) Ti_3C_2 electrode and (b) Mo_2C electrode. (c) Response time.

In this measurement in **Figure 6-3**, the PTE detector is used with Ti_3C_2 electrode of 0.9 μm. With the 873 K blackbody radiation, the temperature of top MXene electrode and bottom Si substrate is 29.6 °C and 22.5 °C. The ambient temperature is 22.5 °C. The temperature difference is 7.1 °C. According to the PTE voltage calculation equation, $V_{PTE} = S_{eff}\Delta T$, where S_{eff} the effective Seebeck coefficient of the detector and ΔT is the temperature difference between two electrodes. The estimated S_{eff} should be 33.8 μV/K.

Then the optoelectrical measurements are performed, and the experiment is performed under an 873 K blackbody radiation source. Both **Figure 6-4 (a)** and **(b)** show a linear I-V curve and demonstrate an excellent ohmic contact among MXene electrodes and CNTF. **Figure 6-4 ©** shows a reproducible curve of the response time. The fall/decay time of the Ti_3C_2 or Mo_2C electrode is 2.4/2.3 s or 2.8/2.7 s, respectively. The possible reason for Mo_2C with a longer response time may be that the Mo_2C electrode shows a stronger electromagnetic shielding effect with an increasing thickness. There are several reasons that Ti_3C_2 exhibits a stronger response current and a faster response than Mo_2C. Firstly, Mo_2C electrodes may show a stronger electromagnetic shielding effect with an increasing thickness. Secondly, the difference in the MXene particle size may cause the thermoelectric properties, leading to different PTE responses[171].

Figure 6-5 (a) shows the responsivity of the PTE detector with different blackbody radiation temperatures. The responsivity can be expressed as $R_V = \frac{V_{ph}}{P_{in}}$, where V_{ph} means the photovoltage and P_{in} means the incident power. Both PTE detectors with 0.9 μm Ti_3C_2 and 1.2 μm Mo_2C electrode show a responsivity of over 3.5 V/W, which demonstrate excellent mid-IR (MIR) PTE conversion. **Figure 6-5** (**b)** shows the detectivity of the PTE detector with different radiation temperatures. The detectivity can be expressed as $D^* = \frac{\sqrt{R_V A_d}}{V_n}$, where A_d is the effective area. The

noise of PTE detectors mainly comes from Johnson-Nyquist noise that can be expressed as $V_n = \sqrt{4k_BTR}$[10], where the Boltzmann constant is 1.9×10^{-23} J·K^{-1}, T is the temperature and R is the

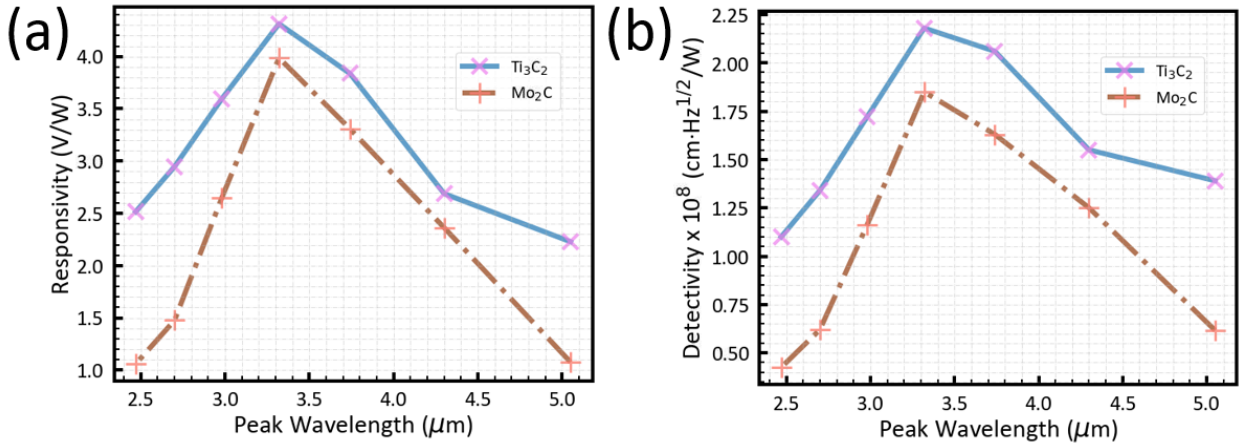

Figure 6-5. (a) Responsivity and (b) detectivity correlate with the power intensity of blackbody radiation.

device resistance. The trends of responsivity match with the responsivity. The detector indicates a maximum detectivity of 2.2×10^8 Jones. The maximum detectivity of 2.2×10^8 Jones locates the blackbody peak wavelength of 3.3 μm. Generally, the thermoelectric properties of the materials do not change with the ambient radiation peak wavelength. Thus, the reason may be that both drop-cast MXenes films show an internal infrared absorption at around 3.3 μm. The competitive PTE response may attribute to several reasons. Firstly, the reduced CNT channel may approximate the cooling length of hot carriers, which mostly maximizes the performance. Secondly, the top MXene electrode may absorb most of the infrared radiation and achieves a rapid and effective PTE conversion. Compared with our previous work, although traditional CNTF can almost absorb all infrared radiation, the heating process may happen in the whole CNTF channel instead of the CNT tip region[68]. Thirdly, without the introduction of polymers, the thermal loss may be reduced and the effective thermoelectric conversion may be increased[191]. Fourthly, the CNTF grown by

PECVD may mainly compose of MWCNTs with a positive Seebeck coefficient of about 30 μV[74]. The CNTF grown by low-pressure CVD may be mixed p-/n-type SWCNTs, which may significantly hinder the thermoelectric capacity and even reduce the PTE conversion efficiency[68]. Furthermore, with a larger gap among CNTs, the PECVD-grown CNTF can be easier to quantify and be designed as the typical number according to specific requirements.

5.5. Top electrode influence

The influence of electrode thickness is measured by adjusting the dropped volume of 25 mg/mL MXene solution. When the dropped solution volume is 10/20/30 μL, the thickness of Ti_3C_2 or Mo_2C film is 0.9/1.8/2.7 μm or 1.2/2.4/3.6 μm, respectively (**Figure 6-6**). Such thin MXene

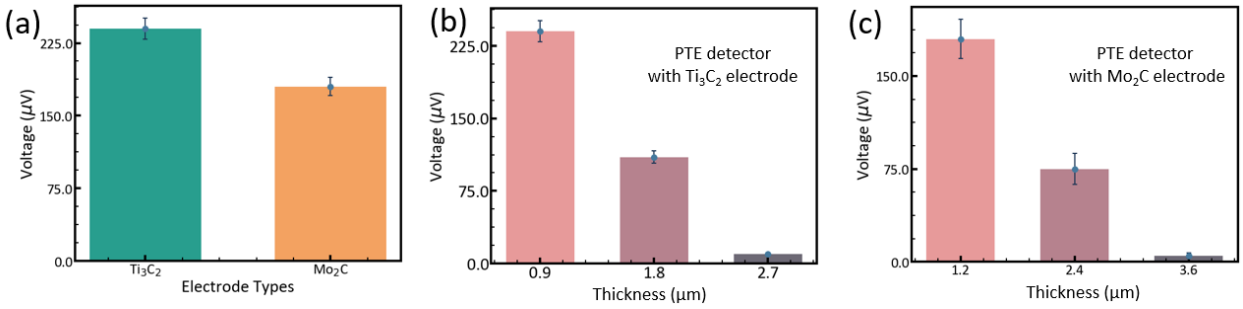

Figure 6-6. The relationship between Photovoltage and (a) Electrode types, (b) Electrode thickness of Ti_3C_2 film and (c) Mo_2C film.

thicknesses indicate the dense deposition and excellent dispersion of MXene solution. With the 873 K blackbody radiation temperature, the photovoltage of both PTE detectors shows a decreasing trend with the increasing electrode thickness. It contribute to the PTE conversion limitations, which means the MXene electrode of typical thickness can achieve a photothermal conversion. Once the top electrode thickness exceeds the typical value, the MXene of extra thickness may act as a heat sink and significantly reduces the thermal energy utilization efficiency

of CNTF. MXene films have been investigated as electromagnetic radiation shielding. For the thick films, the MXene may act as the radiation shielding material and cannot achieve effective photothermal conversion. Thus, only the MXene with typical thickness can realize effective photothermal conversion. Once the top MXene electrode thickness exceeds the typical value, the MXene of extra thickness may act as a heat sink and significantly reduces the thermal energy utilization efficiency of CNTF.

5.6. PTE detector system and NDT imaging

Then NDT imaging test is performed by the measurement setup (**Figure 6-7 (a)**). The blackbody

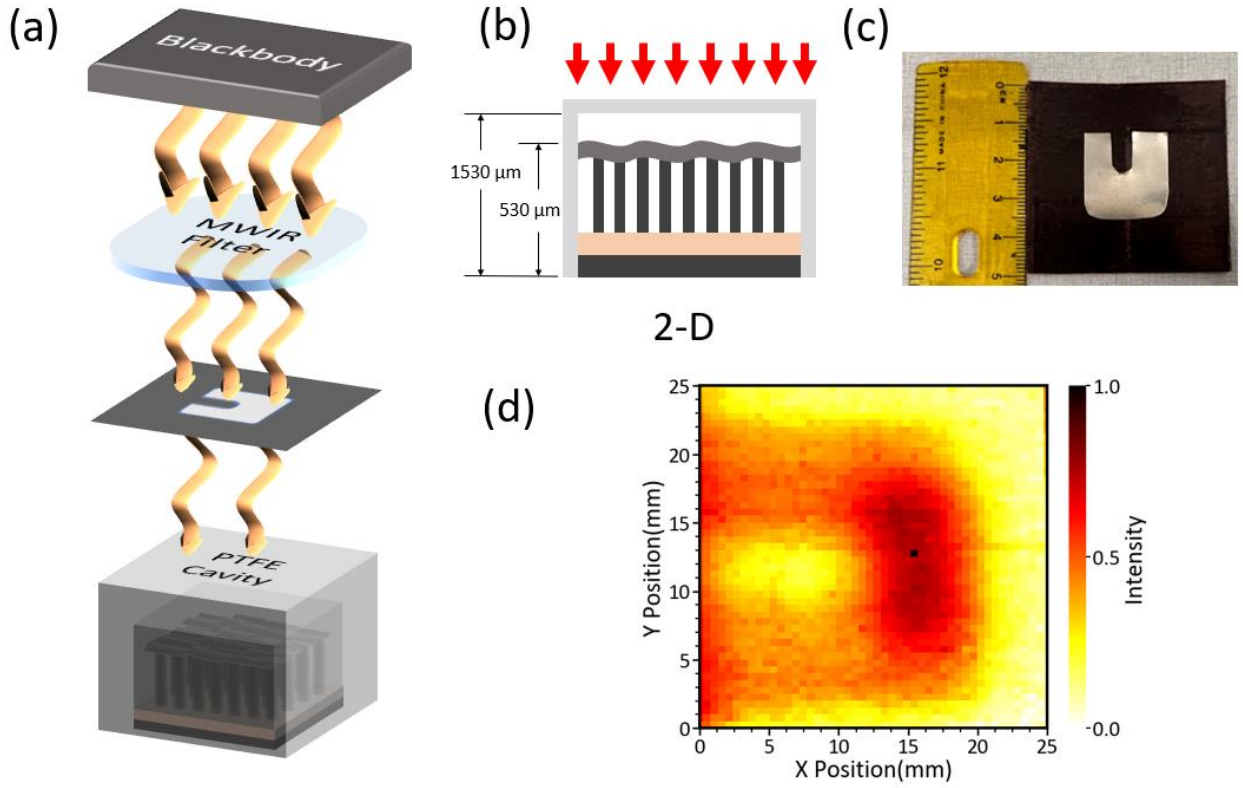

Figure 6-7. (a) The illustration of measurement setup. (b) 2-D illustration of packing detector. The red arrows are the illumination source. (c) Photograph of the real object. (d) NDT PTE imaging. The schematic figures are not illustrated to scale.

radiation passes the MIR filter. The single-pixel packaged PTE detector is fixed in a table. The MC-200 equipment will control the aluminum arrow object to move, where the step length is 500 μm. Typically, the PTFE cavity is manufactured by fill-mode laser cutting. With a full of nitrogen gas environment, the PTE detector can be sealed in the PTFE cavity using vacuum glue. According to Ref. [196], [197], most of the MIR radiation can be transmitted through the PTFE materials, and thus PTFE can act as an excellent packaging and MIR filter material for PTE detectors. Here, the accumulated height of the PTE detector can be calculated as 525× (1±10%) μm (Si substrate) + 100.2 nm (Bottom Cr electrode) + 5 μm (CNTF) + 1 μm (Top MXene electrode) ≈ 530 μm. The cut depth of the PTFE cavity by laser is 1530 μm (**Figure 6-7 (b)**). Then the PTE response of the packed detector is measured using the blackbody radiation and the same experimental conditions, The photovoltage will be recorded and finally, the photovoltage will be patterned according to the relative intensity (**Figure 6-7 (d)**). This experiment demonstrates the capacity of NDT imaging. Furthermore, the resolution can be further optimized by reducing the single-pixel size of the PTE detector and this design idea paves the way for packaging wearable sensors.

5.7. Stability

Given the industrial and product application in the future, the long-term stability for the PTE detectors is also crucial. Thus, the PTE detectors with Ti_3C_2 and Mo_2C top electrodes are tested under the 873 K blackbody radiation. The PTE responses of both detectors show a relatively large degradation. The reason may be that the surface terminations are oxidized and influence infrared absorption and conductivity[198]. The other reason may be that the contact resistance increases between MXene and conductive silver glue because of the degradation of silver glue. The PTE responses of both detectors show a relatively large degradation. The reason may be that the surface terminations are oxidized and influence infrared absorption. Additionally, the device resistance

increases and the potential reason is attributed to the increasing contact resistance between MXene and conductive silver glue. Another reason may be that the conductivity of MXene decreases[198]. Then the PTE response of the encapsulated device with PTFE is tested (**Figure 6-8**). In

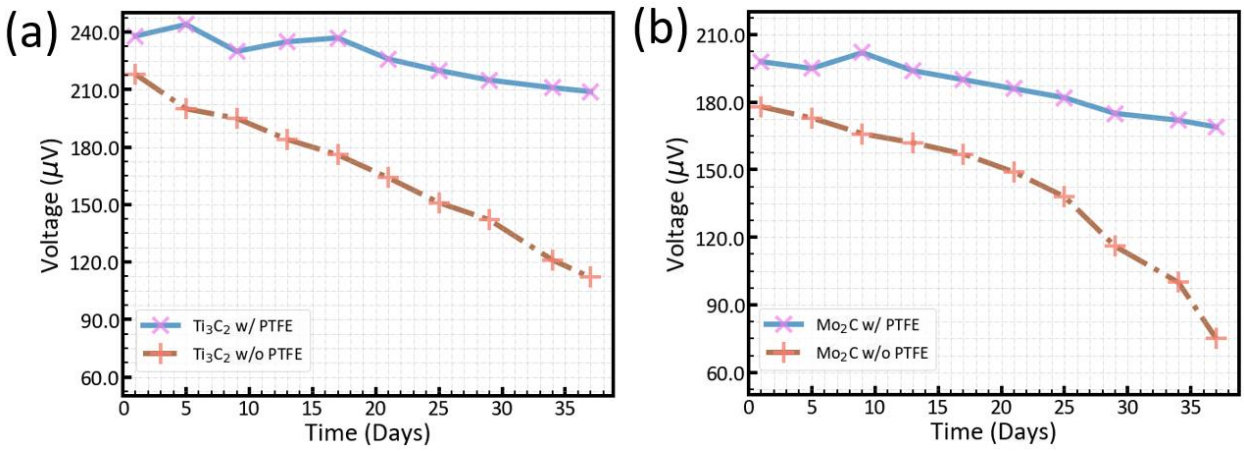

Figure 6-8. With or without PTFE packaging, it shows the relationship between the time and the photovoltage of (a) Ti_3C_2 electrode and (b) Mo_2C electrode.

comparison, the degradation is significantly suppressed after 35 days. This result demonstrates that the packaging will benefit further mass production industrial applications.

To assess our detector performance, our detectors are compared with other MIR detectors. Although our detectors do not show a superior response, they have shown a competitive advantage as the self-powered detectors (**Table 6-1**). Optimizing the CNTF channel may potentially enhance the PTE response according to the thermal decay length theory[199]. Additionally, patterning the MXene top electrodes toward the metamaterials may be another optimization solution.

Table 6-1. Performance Comparison of PTE detectors.

Detection Spectrum	**Active layer**	**Electrodes**	**Response time**	**Detectivity ($\times 10^8$ Jones)**	**Ref.**
MIR	CNTF	MXene/Metal	2.3 s	2.2	This work
MIR	Graphene/PEDOT:PSS	Metal/Metal	>10 s	0.14	[31]
MIR	Graphene/polyaniline	Metal/Metal	>5 s	0.68	[15]
MIR	CNT/(Polyvinyl alcohol)	Metal/Metal	/	0.049	[13]
Terahertz (THz)	CNT	Metal/Metal	/	1.2	[72]
THz	$EuBiTe_3$	Metal/Metal	0.1 s	2.3	[48]

5.8. Conclusion

This chapter reports a self-powered vertical PTE detector working in the MIR regime. This detector adopts CNTF as the PTE channel as well as MXenes as the top electrode. The PTE response related to the two types of MXene electrodes and their electrode thickness are tested. The MXene electrodes show an excellent stable ohmic contact with the CNTF. With a blackbody

temperature of 873 K, the detector demonstrates a detectivity of 2.2×10^8 Jones. Ultimately, our PTE detector is packed into a PTFE system and perform the NDT test, which indicates a response degradation delay and competitive imaging capacity.

Overall, this PTE detector that is integrated with a vertical CNTF channel and MXene electrodes achieves broadband infrared detection. Unlike the laser source, the blackbody radiation source will illuminate a relatively large range, which provides a higher response challenge for the device. Our scalable detector can accept large-area radiation because the top MXene electrodes will absorb the infrared radiation and convert it to thermal energy, forming a temperature difference along with the long-axis direction of CNT and inducing thermoelectric conversion. Compared with the PTE detector using an in-plane asymmetric structure or the p-n junction, this configuration makes use of steric space and provides opportunities for the device miniaturization, where the in-plane absorber area is needed to consider. Additionally, the number and height of CNT can be accurately controlled and the device performance can be quantified. The 1-D CNTF also paves the path to other 1-D materials, such as the nanowire array. Furthermore, the CNTF or nanowire array can be patterned into a metamaterial structure and achieve an in-plane and vertical PTE optimization. The self-powered packaged PTE detectors provide new insights for the industrial long-term monitoring system and daily smart wearable sensors. Typically, the front and back sides of the smartwatch can integrate the PTE detector and achieve an energy harvester of the human body and environmental thermal radiation.

Chapter 7 Summary and Future Work

7.1. Summary of contributions

As a thermal detector, PTE detectors beyond the bandgap limitations of materials can achieve the room-temperature self-powered broadband response. They provide lots of possibilities for civilian and industrial applications like non-destructive tracking (NDT) and wearable sensors. However, there are still some issues with the current PTE materials and design. The infrared absorption of most two-dimensional materials is low. High-performance PTE detectors are usually achieved in the single-layer or single-sheet surface, which requires accurate delamination methods or expensive electron-beam lithography (EBL) pattern technique. The degradation is significant and current PTE structures cannot meet the demands for long-term durability and stability. In this dissertation, I have proposed some systematic solutions, which are dedicated to addressing the abovementioned issues. Below are my summary of contributions.

My first contribution is to design a novel one-step grown process to create the PTE structure based on CNTF. By configuring the different growth conditions, CNTFs of different lengths are obtained and connected by the introduction of DMSO. Utilize the capillary phenomenon in the PTE structure design. This structure could potentially achieve a scalable detector because of the changeable junction width and length. Obtain a competitive response of 40 ms and a high detectivity up to 1.38×10^{8} Jones by the capillary-induced CNT PTE structure. The detectivity is 10 times more sensitive than mainstream PTE detectors. Additionally, this detector utilizes the cleanroom fabrication processes and paves the path toward industrial applications. This part of the work is shown in Chapter 3.

My second contribution is to develop an individual flexible membrane for PTE detectors based

on the SWCNT/PEDOT:PSS composite material. By adjusting and optimizing the SWCNT loading in the nanocomposite, the photoresponse can be enhanced with a peak detectivity of 1.9×10^7 Jones. The first PTE-based sensor is demonstrated for monitoring ocular surface behaviour. The ocular monitoring experiments can clearly distinguish the blinking cycles and times. I also fabricate a CNTF/PEDOT:PSS vertical PTE detector, verify the thermal imaging tracking capacity of this detector and obtain a rough crossing pattern. This part of the work is shown in Chapter 4.

My third contribution is to first adopt the two-dimensional material MXene in a mid-infrared PTE detector with high responsivity and detectivity. The engineering strategies of vertical PTE detectors are investigated comprehensively, including substrate, electrodes and vacuum conditions. The metamaterial structure is integrated into the PTE detector. Here, the metamaterial is simulated, fabricated, and characterized. Finally, the 3×3 array pixel panel is fabricated and the simultaneous non-contact fingertip signal tracking capacity of the detector array is verified. This part of the work is shown in Chapter 5.

My fourth contribution is to apply non-metal MXene electrodes instead of traditional metal electrodes for PTE detectors. Here, MXene top electrodes can act as MIR material and PTE heat source. PTFE is encapsulated into the PTE detector to suppress the degradation and enhance the PTE response. the crossing pattern thermal imaging is obtained using the packaged PTE system, which is shown to extend the lifetime of the detector. This part of the work is shown in Chapter 6.

7.2. Future work

Currently, PTE detectors are emerging but there still exist some challengings. They are still on the way toward practical applications. Here, I propose some potential optimization strategies.

7.2.1. Material optimization

1) Flexible materials

Current PTE detectors are mainly composed of solid materials and substrates. For future wearable and flexible e-skin applications, how to configure inherent flexible sensors become important. Here two potentially viable paths are proposed. One is to integrate the current flexible sensors into the liquid environment and increase biocompatibility with the human body. The other one is to fabricate flexible PTE detectors based on the photothermal and ionic thermoelectric mechanism, where all components are hydrogel or related composites with excellent bending or curved properties.

2) CNTs

The chirality of CNT growth is key but remains challenging to control because the related metallic and semiconducting properties are related to the PTE responses[74]. Improving CNT quality as well as reducing defects and impurities is also of prime importance. For the PTE detectors, the adhesion and interaction between CNT and electrodes also need to be optimized.

3) Device stability

For the PTE detectors, long-time stability and durability are expected. Low-dimensional nanomaterials generally suffer from degradation issues, like BP. Except that the device is packed into a vacuum environment. The modification and optimization of materials should be emphasized without decreasing the device's performance.

7.2.2. System design strategies

1) Miniaturization

Any competitive sensors will lead to the path toward miniaturization and low cost. For PTE

detectors based on low-dimensional nanomaterials, a set of their miniaturization system should be created. How to manipulate and pattern the low-dimensional materials effectively is still a challenge. It is of importance because the array size or the integration with meta structures or circuits requires accurate location and reproducibility.

For current PTE detectors, most of them only focus on one way. For example, if the detectors are fabricated with miniaturization and high sensitivity, the EBL or other expensive technologies will be utilized. Especially for low-dimensional nanomaterials, the pursuit of high performance and the ignorance of practical manufacturing cannot be accepted. Thus, achieving inexpensive mass production of PTE detectors with stable and durable functions is desired.

2) Circuit

For a complete detector system design, the circuit cannot be separated. Like traditional transistors, achieving relatively high performance and starting the next-generation circuit integration early are critical steps. Flexible or silicon-based PTE detectors should be divided into two different integration directions but both ways should work toward the application-specific integrated circuit.

7.2.3. Application probabilities

1) Non-contact sensors

In this thesis, many applications are proposed like non-contact fingertip/eyeball responses and NDT. However, they are just infant periods of application, and the PTE response of infrared detectors is still lower than that of present ultraviolet detectors, which cannot meet practical demands. High sensitivity and quick response are the keys to civilian or medical applications. The high-performance sensors of contact mode have succeeded for many years. Thus, to dominate part

of the markets, stable and sensitive PTE detectors are required and applied for augmented reality and virtual reality or non-contact touch screens.

2) Smart wearable devices

There exists a large difference between the human body temperature and ambient surroundings. The broadband PTE detectors can play the PTE or thermoelectric role and act as energy harvesters. Especially in the cold area with a temperature of <30 °C, the temperature difference can be larger than 70 °C. The smart textile integrated with PTE detectors can make sense.

References

[1] Q. Shen *et al.*, "Bioinspired Infrared Sensing Materials and Systems," *Adv. Mater.*, vol. 30, no. 28, p. 1707632, 2018, DOI: 10.1002/adma.201707632.

[2] D. Palaferri *et al.*, "Room-temperature nine-μm-wavelength photodetectors and GHz-frequency heterodyne receivers," *Nature*, vol. 556, no. 7699, pp. 85–88, 2018, DOI: 10.1038/nature25790.

[3] E. D. Walsh *et al.*, "Josephson junction infrared single-photon detector," *Science*, vol. 372, no. 6540, pp. 409–412, 2021, DOI: 10.1126/science.abf5539.

[4] C. Besikci, "Nature Allows High Sensitivity Thermal Imaging with Type-I Quantum Wells without Optical Couplers: A Grating-Free Quantum Well Infrared Photodetector with High Conversion Efficiency," *IEEE J. Quantum Electron.*, vol. 57, no. 2, p. 4300112, 2021, DOI: 10.1109/JQE.2021.3052188.

[5] V. Devarakonda *et al.* , "Enhanced optoelectronic properties of a mercury cadmium telluride based double heterojunction photodetector for terahertz applications," *Optik*, vol. 247, p. 167947, 2021, DOI: 10.1016/j.ijleo.2021.167947.

[6] M. S. El_Tokhy and I. I. Mahmoud, "Detectivity analysis of infrared photodetector devices under nonuniform distribution of quantum well and wire," *Optik (Stuttg).*, vol. 227, p. 166113, 2021, DOI: 10.1016/j.ijleo.2020.166113.

[7] X. Lu *et al.*, "Phonon-enhanced photothermoelectric effect in $SrTiO_3$ ultra-broadband photodetector," *Nat. Commun.*, vol. 10, no. 1, pp. 1–7, 2019, DOI: 10.1038/s41467-018-07860-0.

[8] X. Cai *et al.*, “Sensitive room-temperature terahertz detection via the photothermoelectric effect in graphene,” *Nat. Nanotechnol.*, vol. 9, no. 10, pp. 814–819, 2014, DOI: 10.1038/nnano.2014.182.

[9] R. Yuasa *et al.*, “Robot-assisted, source-camera-coupled multi-view broadband imagers for ubiquitous sensing platform,” *Nat. Commun.*, vol. 12, p. 3009, 2021, DOI: 10.1038/s41467-021-23089-w.

[10] W. Wu *et al.*, “Thermal Localization Enhanced Fast Photothermoelectric Response in a Quasi-One-Dimensional Flexible NbS_3 Photodetector,” *ACS Appl. Mater. Interfaces*, vol. 12, no. 12, pp. 14165–14173, 2020, DOI: 10.1021/acsami.0c00764.

[11] X. Lu *et al.*, “Progress of Photodetectors Based on the Photothermoelectric Effect,” *Adv. Mater.*, vol. 31, no. 50, pp. 1–26, 2019, DOI: 10.1002/adma.201902044.

[12] Y. Chen *et al.*, “Highly efficient hot electron harvesting from graphene before electron-hole thermalization,” *Sci. Adv.*, vol. 5, no. 11, p. eaax9958, 2019, DOI: 10.1126/sciadv.aax9958.

[13] M. Zhang and J. T. W. Yeow, “Flexible Polymer - Carbon Nanotube Composite with High Response Stability for Wearable Thermal Imaging,” *ACS Appl. Mater. Interfaces*, vol. 10, no. 31, pp. 26604–26609, 2018, DOI: 10.1021/acsami.8b06482.

[14] J. Gosciniak *et al.*, “Ultrafast Plasmonic Graphene Photodetector Based on the Channel Photothermoelectric Effect,” *ACS Photonics*, vol. 7, no. 2, pp. 488–498, 2020, DOI: 10.1021/acsphotonics.9b01585.

[15] Z. Xie *et al.*, “Doped Polyaniline/Graphene Composites for Photothermoelectric Detectors,” *ACS Appl. Nano Mater.*, vol. 5, no. 6, pp. 7967-7973, 2022, DOI: 10.1021/acsanm.2c01039.

[16] M. Chen *et al.*, “Annealing Temperature-Dependent Terahertz Thermal–Electrical Conversion Characteristics of Three-Dimensional Microporous Graphene,” *ACS Appl. Mater. Interfaces*, vol. 11, no. 6, pp. 6411–6420, 2019, DOI: 10.1021/acsami.8b20095.

[17] B. Fang *et al.*, “Bidirectional mid-infrared communications between two identical macroscopic graphene fibres,” *Nat. Commun.*, vol. 11, no. 1, p. 6368, 2020, DOI: 10.1038/s41467-020-20033-2.

[18] L. Wang *et al.*, “Toward Sensitive Room-Temperature Broadband Detection from Infrared to Terahertz with Antenna-Integrated Black Phosphorus Photoconductor,” *Adv. Funct. Mater.*, vol. 27, no. 7, 2017, DOI: 10.1002/adfm.201604414.

[19] A. Rogalski, *Infrared and Terahertz Detectors, Third Edition*. 2019.

[20] A. Rogalski, “Scaling infrared detectors—status and outlook,” *Reports Prog. Phys.*, vol. 85, no. 12, 2022, DOI: 10.1088/1361-6633/ac97a8.

[21] H. Zhou *et al.*, “MOF/Polymer-Integrated Multi-Hotspot Mid-Infrared Nanoantennas for Sensitive Detection of CO_2 Gas,” *Nano-Micro Lett.*, vol. 14, no. 1, 2022, DOI: 10.1007/s40820-022-00950-1.

[22] Y. Wu *et al.*, “Ultrabroad Microwave Absorption Ability and Infrared Stealth Property of Nano-Micro CuS@rGO Lightweight Aerogels,” *Nano-Micro Lett.*, vol. 14, no. 1, 2022, DOI: 10.1007/s40820-022-00906-5.

[23] D. Klocke *et al.* , “Infrared receptors in pyrophilous (‘fire loving’) insects as model for new un-cooled infrared sensors,” *Beilstein J. Nanotechnol.*, vol. 2, no. 1, pp. 186–197, 2011, DOI: 10.3762/bjnano.2.22.

[24] J.-J. Yon *et al.*, “Latest amorphous silicon microbolometer developments at LETI-LIR,” *SPIE Proceedings*, vol. 6940, pp. 631–638, 2008, DOI: 10.1117/12.780538.

[25] R. Lu *et al.*, “Suspending single-wall carbon nanotube thin film infrared bolometers on microchannels,” *Appl. Phys. Lett.*, vol. 94, no. 16, p. 163110, 2009, DOI: 10.1063/1.3124651.

[26] X. He, F. Léonard, and J. Kono, “Uncooled Carbon Nanotube Photodetectors,” *Adv. Opt. Mater.*, vol. 3, no. 8, pp. 989–1011, 2015, DOI: 10.1002/adom.201500237.

[27] S. A. Kuznetsov *et al.*, “Selective Pyroelectric Detection of Millimetre Waves Using Ultra-Thin Metasurface Absorbers,” *Sci. Rep.*, vol. 6, no. 1, p. 21079, 2016, DOI: 10.1038/srep21079.

[28] A. Thakre *et al.*, “Pyroelectric Energy Conversion and Its Applications—Flexible Energy Harvesters and Sensors,” *Sensors*, vol. 19, no. 9. 2019, DOI: 10.3390/s19092170.

[29] X. Z. Jin *et al.*, “Polypyrrole/helical carbon nanotube composite with marvelous photothermoelectric performance for longevous and intelligent internet of things application,” *ACS Appl. Mater. Interfaces*, vol. 13, no. 7, pp. 8808–8822, 2021, DOI: 10.1021/acsami.0c22123.

[30] C. Voisin and B. Plaçais, “Hot carriers in graphene,” *J. Phys. Condens. Matter*, vol. 27, no. 16, 2015, DOI: 10.1088/0953-8984/27/16/160301.

[31] M. Zhang and J. T. W. Yeow, “A flexible, scalable, and self-powered mid-infrared detector based on transparent PEDOT: PSS/graphene composite,” *Carbon N. Y.*, vol. 156, pp. 339–345, 2020, DOI: 10.1016/j.carbon.2019.09.062.

[32] X.-L. Shi *et al.*, “Advanced Thermoelectric Design: From Materials and Structures to Devices,” *Chem. Rev.*, vol. 120, no. 15, pp. 7399–7515, 2020, DOI: 10.1021/acs.chemrev.0c00026.

[33] J. Zhou *et al.*, “Ab initio optimization of phonon drag effect for lower-temperature thermoelectric energy conversion,” *Proc. Natl. Acad. Sci.*, vol. 112, no. 48, pp. 14777–14782, 2015, DOI: 10.1073/pnas.1512328112.

[34] Y. J. Zeng *et al.*, “Nanoscale Organic Thermoelectric Materials: Measurement, Theoretical Models, and Optimization Strategies,” *Adv. Funct. Mater.*, vol. 30, no. 8, pp. 1–25, 2020, DOI: 10.1002/adfm.201903873.

[35] C. Gayner and Y. Amouyal, “Energy Filtering of Charge Carriers: Current Trends, Challenges, and Prospects for Thermoelectric Materials,” *Adv. Funct. Mater.*, vol. 30, no. 18, p. 1901789, 2020, DOI: 10.1002/adfm.201901789.

[36] Y. Li *et al.*, “Structural semiconductor-to-semimetal phase transition in two-dimensional materials induced by electrostatic gating,” *Nat. Commun.*, vol. 7, no. 1, p. 10671, 2016, DOI: 10.1038/ncomms10671.

[37] T. Koga *et al.*, “Carrier pocket engineering to design superior thermoelectric materials using GaAs/AlAs superlattices,” *Appl. Phys. Lett.*, vol. 73, no. 20, pp. 2950–2952, 1998, DOI: 10.1063/1.122640.

[38] W. Guo *et al.*, “Sensitive Terahertz Detection and Imaging Driven by the Photothermoelectric Effect in Ultrashort-Channel Black Phosphorus Devices,” *Adv. Sci.*, vol. 7, no. 5, 2020, DOI: 10.1002/advs.201902699.

[39] I. J. Luxmoore *et al.*, “Graphene-Metamaterial Photodetectors for Integrated Infrared Sensing,” *ACS Photonics*, vol. 3, no. 6, pp. 936–941, 2016, DOI: 10.1021/acsphotonics.6b00226.

[40] X. He *et al.*, “Photothermoelectric p-n junction photodetector with intrinsic broadband polarimetry based on macroscopic carbon nanotube films,” *ACS Nano*, vol. 7, no. 8, pp. 7271–7277, 2013, DOI: 10.1021/nn402679u.

[41] K. Li *et al.*, “Series Photothermoelectric Coupling Between Two Composite Materials for a Freely Attachable Broadband Imaging Sheet,” *Adv. Photonics Res.*, vol. 2, no. 3, p. 2000095, 2021, DOI: 10.1002/adpr.202000095.

[42] T. Hong *et al.*, “Polarized photocurrent response in black phosphorus field-effect transistors,” *Nanoscale*, vol. 6, no. 15, pp. 8978–8983, 2014, DOI: 10.1039/c4nr02164a.

[43] Y. Li *et al.*, “A fast response, self-powered and room temperature near infrared-terahertz photodetector based on a $MAPbI_3$/PEDOT:PSS composite,” *J. Mater. Chem. C*, vol. 8, no. 35, pp. 12148–12154, 2020, DOI: 10.1039/d0tc02399j.

[44] J. Li *et al.*, “Enhanced room-temperature terahertz detection and imaging derived from anti-reflection 2D perovskite layer on $MAPbI_3$ single crystals,” *Nanoscale*, vol. 14, no. 16, pp. 6109–6117, 2022, DOI: 10.1039/d2nr00497f.

[45] M. Li *et al.*, “Synergistic optimization of photothermoelectric performance of a perovkite/graphene composite,” *Ceram. Int.*, vol. 48, no. 3, pp. 4366–4370, 2022, DOI: 10.1016/j.ceramint.2021.10.175.

[46] X. Guo, X. Lu, P. Jiang, and X. Bao, “$SrTiO_3$/CuNi-Heterostructure-Based Thermopile for

Sensitive Human Radiation Detection and Noncontact Human–Machine Interaction," *Adv. Mater.*, vol. 34, no. 35, p. 2204355, 2022, DOI: 10.1002/adma.202204355.

[47] Y. Wang *et al.*, "Ultrabroadband, Sensitive, and Fast Photodetection with Needle-Like $EuBiSe_3$ Single Crystal," *ACS Photonics*, vol. 6, no. 4, pp. 895–903, 2019, DOI: 10.1021/acsphotonics.8b01527.

[48] Y. Niu *et al.*, " Efficient room-temperature terahertz detection via bolometric and photothermoelectric effects in $EuBiTe_3$ crystal ," *Opt. Mater. Express*, vol. 10, no. 4, p. 952, 2020, DOI: 10.1364/ome.387795.

[49] B. Varghese *et al.*, "Photothermoelectric effects in localized photocurrent of individual VO_2 nanowires," *J. Phys. Chem. C*, vol. 114, no. 35, pp. 15149–15156, 2010, DOI: 10.1021/jp1051936.

[50] N. Erhard *et al.*, "Ultrafast Photodetection in the Quantum Wells of Single AlGaAs/GaAs-Based Nanowires," *Nano Lett.*, vol. 15, no. 10, pp. 6869–6874, 2015, DOI: 10.1021/acs.nanolett.5b02766.

[51] F. Léonard *et al.*, "Simultaneous Thermoelectric and Optoelectronic Characterization of Individual Nanowires," *Nano Lett.*, vol. 15, no. 12, pp. 8129–8135, 2015, DOI: 10.1021/acs.nanolett.5b03572.

[52] X. Wang *et al.*, "Photothermoelectric Detection of Gold Oxide Nonthermal Decomposition," *Nano Lett.*, vol. 18, no. 10, pp. 6557–6562, 2018, DOI: 10.1021/acs.nanolett.8b03153.

[53] K. Zhang *et al.*, "Coupling Enhancement of Photo-Thermoelectric Conversion in a Lateral ZnO Nanowire Array," *ACS Appl. Energy Mater.*, vol. 2, no. 10, pp. 7647–7654, 2019, DOI:

10.1021/acsaem.9b01633.

[54] R. Wang *et al.*, "Manipulating Nanowire Structures for an Enhanced Broad-Band Flexible Photothermoelectric Photodetector," *Nano Lett.*, vol. 22, no. 14, pp. 5929-5935, 2022, DOI: 10.1021/acs.nanolett.2c01957.

[55] Y. Liu *et al.*, "Organic/Inorganic Hybrid Boosting Energy Harvesting Based on the Photothermoelectric Effect," *ACS Appl. Mater. Interfaces*, vol. 13, no. 36, pp. 43155-54162, 2021, DOI: 10.1021/acsami.1c10990.

[56] N. Komatsu *et al.*, "Macroscopic weavable fibers of carbon nanotubes with giant thermoelectric power factor," *Nat. Commun.*, vol. 12, no. 1, p. 4931, 2021, DOI: 10.1038/s41467-021-25208-z.

[57] Y. Wang *et al.*, "Fixture-free omnidirectional prestretching fabrication and integration of crumpled in-plane micro-supercapacitors," *Sci. Adv.*, vol. 8, no. 21, 2022, DOI: 10.1126/sciadv.abn8338.

[58] K. R. Jinkins *et al.*, "Aligned 2D carbon nanotube liquid crystals for wafer-scale electronics," *Sci. Adv.*, vol. 7, no. 37, 2021, DOI: 10.1126/sciadv.abh0640.

[59] X. Ma *et al.*, "6 nm super-resolution optical transmission and scattering spectroscopic imaging of carbon nanotubes using a nanometer-scale white light source," *Nat. Commun.*, vol. 12, no. 1, 2021, DOI: 10.1038/s41467-021-27216-5.

[60] S. Liang *et al.*, "Microcavity-Integrated Carbon Nanotube Photodetectors," *ACS Nano*, vol. 10, no. 7, pp. 6963–6971, 2016, DOI: 10.1021/acsnano.6b02898.

[61] Y. Feng *et al.*, "Drastically reduced thermal conductivity of self-bundled single-walled

carbon nanotube," *Carbon N. Y.*, vol. 201, pp. 433–438, 2023, DOI: 10.1016/j.carbon.2022.09.024.

[62] Y. Zheng *et al.*, "Photochemical spin-state control of binding configuration for tailoring organic color center emission in carbon nanotubes," *Nat. Commun.*, vol. 13, no. 1, p. 4439, 2022, DOI: 10.1038/s41467-022-31921-0.

[63] S.-J. Choi *et al.*, "Short-Channel Transistors Constructed with Solution-Processed Carbon Nanotubes," *ACS Nano*, vol. 7, no. 1, pp. 798–803, 2013, DOI: 10.1021/nn305277d.

[64] M. Kumar, "Carbon Nanotube Synthesis and Growth Mechanism," 2011, DOI: 10.5772/19331.

[65] T. De los Arcos *et al.*, "Strong influence of buffer layer type on carbon nanotube characteristics," *Carbon N. Y.*, vol. 42, no. 1, pp. 187–190, 2004, DOI: 10.1016/j.carbon.2003.10.020.

[66] Y. J. Jung *et al.*, "Mechanism of Selective Growth of Carbon Nanotubes on SiO_2/Si Patterns," *Nano Lett.*, vol. 3, no. 4, pp. 561–564, 2003, DOI: 10.1021/nl034075n.

[67] H. Sato *et al.*, "Effect of catalyst oxidation on the growth of carbon nanotubes by thermal chemical vapor deposition," *J. Appl. Phys.*, vol. 100, no. 10, p. 104321, 2006, DOI: 10.1063/1.2364381.

[68] M. Zhang *et al.*, "Large-Area and Broadband Thermoelectric Infrared Detection in a Carbon Nanotube Black-Body Absorber," *ACS Nano*, vol. 13, no. 11, pp. 13285–13292, 2019, DOI: 10.1021/acsnano.9b06332.

[69] B. C. St-Antoine *et al.*, "Position sensitive photothermoelectric effect in suspended single-

walled carbon nanotube films," *Nano Lett.*, vol. 9, no. 10, pp. 3503–3508, 2009, DOI: 10.1021/nl901696j.

[70] B. C. St-Antoine *et al.*, "Single-walled carbon nanotube thermopile for broadband light detection," *Nano Lett.*, vol. 11, no. 2, pp. 609–613, 2011, DOI: 10.1021/nl1036947.

[71] B. C. St-Antoine *et al.* , "Photothermoelectric effects in single-walled carbon nanotube films: Reinterpreting scanning photocurrent experiments," *Nano Res.*, vol. 5, no. 2, pp. 73–81, 2012, DOI: 10.1007/s12274-011-0186-x.

[72] D. Suzuki *et al.*, "A flexible and wearable terahertz scanner," *Nat. Photonics*, vol. 10, no. 12, pp. 809–813, 2016, DOI: 10.1038/nphoton.2016.209.

[73] D. Suzuki *et al.*, "Thermal Device Design for a Carbon Nanotube Terahertz Camera," *ACS Omega*, vol. 3, no. 3, pp. 3540–3547, 2018, DOI: 10.1021/acsomega.7b02032.

[74] D. Suzuki *et al.*, "Fermi-level-controlled semiconducting-separated carbon nanotube films for flexible terahertz imagers," *ACS Appl. Nano Mater.*, vol. 1, no. 6, pp. 2469–2475, 2018, DOI: 10.1021/acsanm.8b00421.

[75] D. Suzuki *et al.*, "Improvement in laser-based micro-processing of carbon nanotube film devices," *Appl. Phys. Express*, vol. 15, no. 2, p. 026503, 2022, DOI: 10.35848/1882-0786/ac4d06.

[76] D. Suzuki *et al.*, "Carbon nanotube-based , serially connected terahertz sensor with enhanced thermal and optical efficiencies," *Sci. Technol. Adv. Mater.*, vol. 23, no. 1, pp. 424–433, 2022, DOI: 10.1080/14686996.2022.2090855.

[77] K. Ruan *et al.*, "Significant Reduction of Interfacial Thermal Resistance and Phonon

Scattering in Graphene/Polyimide Thermally Conductive Composite Films for Thermal Management," *Research*, vol. 2021, p. 8438614, 2021, DOI: 10.34133/2021/8438614.

[78] S. Hida *et al.*, "Thermal resistance and phonon scattering at the interface between carbon nanotube and amorphous polyethylene," *Int. J. Heat Mass Transf.*, vol. 67, pp. 1024–1029, 2013, DOI: 10.1016/j.ijheatmasstransfer.2013.08.068.

[79] J. Park and Y. G. Jeong, "Thermoelectric and Photothermoelectric Properties of Nanocomposite Films Based on Polybenzimidazole and Carbon Nanotubes," *ACS Appl. Electron. Mater.*, vol. 4, no. 1, pp. 386–393, 2022, DOI: 10.1021/acsaelm.1c01056.

[80] X. Jin *et al.*, "Ultraflexible PEDOT : PSS / Helical Carbon Nanotubes Film for All-in-One Photothermoelectric Conversion," *ACS Appl. Mater. Interfaces*, vol. 14, no. 23, pp. 27083-27095, 2022, DOI: 10.1021/acsami.2c05875.

[81] M. Naguib *et al.*, "Two-Dimensional Nanocrystals Produced by Exfoliation of Ti_3AlC_2," *Adv. Mater.*, vol. 23, no. 37, pp. 4248–4253, 2011, DOI: 10.1002/adma.201102306.

[82] A. Vahidmohammadi, "The world of two-dimensional carbides and nitrides (MXenes)," *Science*, vol. 372, no. 6547, 2021, DOI: 10.1126/science.abf1581.

[83] Y. Yang *et al.*, "Plasmonic Transition Metal Carbide Electrodes for High-Performance InSe Photodetectors," *ACS Nano*, vol. 13, no. 8, pp. 8804–8810, 2019, DOI: 10.1021/acsnano.9b01941.

[84] J. K. El-Demellawi *et al.*, "Tunable Multipolar Surface Plasmons in 2D Ti_3C_2 Tx MXene Flakes," *ACS Nano*, vol. 12, no. 8, pp. 8485–8493, 2018, DOI: 10.1021/acsnano.8b04029.

[85] D. B. Velusamy *et al.*, "MXenes for Plasmonic Photodetection," *Adv. Mater.*, vol. 31, no.

32, pp. 1–10, 2019, DOI: 10.1002/adma.201807658.

[86] G. Li *et al.*, "Two-Dimensional MXenes $Mo_2Ti_2C_3T_z$ and $Mo_2TiC_2T_z$: Microscopic Conductivity and Dynamics of Photoexcited Carriers," *ACS Appl. Energy Mater.*, vol. 3, no. 2, pp. 1530–1539, 2020, DOI: 10.1021/acsaem.9b01966.

[87] G. Li *et al.*, "Equilibrium and non-equilibrium free carrier dynamics in 2D $Ti_3C_2T_x$ MXenes: THz spectroscopy study," *2D Mater.*, vol. 5, no. 3, p. 035043, 2018, DOI: 10.1088/2053-1583/aacb9e.

[88] S. Gan *et al.*, "Highly Sensitive Surface Plasmon Resonance Sensor Modified with 2D TiC MXene for Solution Detection," *IEEE Sens. J.*, vol. 21, no. 1, pp. 347–352, 2021, DOI: 10.1109/JSEN.2020.3015574.

[89] Y. I. Jhon *et al.*, "First-principles study of a MXene terahertz detector," *Nanoscale*, vol. 10, no. 1, pp. 69–75, 2018, DOI: 10.1039/c7nr05351g.

[90] J. Wei *et al.*, "Free-standing p-Type SWCNT/MXene composite films with low thermal conductivity and enhanced thermoelectric performance," *Chem. Eng. J.*, vol. 439, no. December 2021, p. 135706, 2022, DOI: 10.1016/j.cej.2022.135706.

[91] J.-H. Kim *et al.*, "Highly strain-tolerant, disposable gas sensor on plastic wrap using two-dimensional hybrid nanomaterials," *Mater. Chem. Phys.*, vol. 292, p. 126820, 2022, DOI: 10.1016/j.matchemphys.2022.126820.

[92] R. C. Rohit *et al.*, "MXene ($Ti_3C_2T_x$) modified α-$Co(OH)_2$ battery-type cathode and highly capacitive binder-free $Ti_3C_2T_x$ anode for high-performance electrochemical hybrid capacitor," *2D Mater.*, vol. 9, no. 4, p. 045031, 2022, DOI: 10.1088/2053-1583/ac9191.

[93] L. Feng *et al.*, “Study of MXene $Ti_3C_2T_x$ quantum dot thin film on quartz bulk acoustic wave uncooled infrared sensors,” *Opt. Express*, vol. 30, no. 19, pp. 34129–34139, 2022, DOI: 10.1364/OE.468458.

[94] I. Ali *et al.*, “MXenes Thin Films: From Fabrication to Their Applications,” *Molecules*, vol. 27, no. 15, p. 4925, 2022, DOI: 10.3390/molecules27154925.

[95] Y. Zhang *et al.*, “Smart and flexible CNTs@MXene heterostructure-decorated cellulose films with excellent electrothermal/photothermal conversion and EMI shielding performances,” *Carbon N. Y.*, vol. 200, pp. 491–499, 2022, DOI: 10.1016/j.carbon.2022.08.040.

[96] C. Xie *et al.*, “Flexible, conductive and multifunctional cotton fabric with surface wrinkled MXene/CNTs microstructure for electromagnetic interference shielding,” *Colloids Surfaces A Physicochem. Eng. Asp.*, vol. 651, p. 129713, 2022, DOI: 10.1016/j.colsurfa.2022.129713.

[97] F. Jia *et al.*, “Robust, flexible, and stable CuNWs/MXene/ANFs hybrid film constructed by structural assemble strategy for efficient EMI shielding,” *Chem. Eng. J.*, vol. 452, p. 139395, 2023, DOI: 10.1016/j.cej.2022.139395.

[98] R. Thankappan *et al.*, “MXene-coated flexible PVDF membrane as wearable strain sensor,” *J. Mater. Sci. Mater. Electron.*, vol. 33, no. 32, pp. 24542–24549, 2022, DOI: 10.1007/s10854-022-09165-x.

[99] L. Tian *et al.*, “Sweat cortisol determination utilizing MXene and multi-walled carbon nanotube nanocomposite functionalized immunosensor,” *Microchem. J.*, vol. 185, p. 108172, 2023, DOI: 10.1016/j.microc.2022.108172.

[100] K. Li *et al.*, "4D printing of MXene hydrogels for high-efficiency pseudocapacitive energy storage," *Nat. Commun.*, vol. 13, no. 1, p. 6884, 2022, DOI: 10.1038/s41467-022-34583-0.

[101] Y. I. Jhon *et al.*, "First-principles study of a MXene terahertz detector," *Nanoscale*, vol. 10, no. 1, pp. 69–75, 2018, DOI: 10.1039/c7nr05351g.

[102] H. Zhou *et al.*, "A flexible in-plane p–n heterojunction nano- generator with phonon-enhanced photothermoelectric effect to harvest solar energy," *J. Mater. Chem. A*, vol. 9, pp. 14958–14968, 2021, DOI: 10.1039/d1ta02946k.

[103] X. He *et al.*, "Carbon nanotube terahertz detector," *Nano Lett.*, vol. 14, no. 7, pp. 3953–3958, 2014, DOI: 10.1021/nl5012678.

[104] M. Zhang and J. T. W. Yeow, "Flexible Polymer-Carbon Nanotube Composite with High-Response Stability for Wearable Thermal Imaging," *ACS Appl. Mater. Interfaces*, vol. 10, no. 31, pp. 26604–26609, 2018, DOI: 10.1021/acsami.8b06482.

[105] A. Sharma *et al.*, "A carbon nanotube optical rectenna," *Nat. Nanotechnol.*, vol. 10, no. 12, pp. 1027–1032, 2015, DOI: 10.1038/nnano.2015.220.

[106] M. Barkelid and V. Zwiller, "Photocurrent generation in semiconducting and metallic carbon nanotubes," *Nat. Photonics*, vol. 8, no. 1, pp. 47–51, 2014, DOI: 10.1038/nphoton.2013.311.

[107] P. Avouris *et al.*, "Carbon-nanotube photonics and optoelectronics," *Nat. Photonics*, vol. 2, no. 6, pp. 341–350, 2008, DOI: 10.1038/nphoton.2008.94.

[108] K. J. Erikson *et al.*, "Figure of Merit for Carbon Nanotube Photothermoelectric Detectors," *ACS Nano*, vol. 9, no. 12, pp. 11618–11627, 2015, DOI: 10.1021/acsnano.5b06160.

[109] Y. Zhang *et al.*, “Carbon and carbon composites for thermoelectric applications,” *Carbon Energy*, vol. 2, no. 3, pp. 408–436, 2020, DOI: 10.1002/cey2.68.

[110] S. Nanot *et al.*, “Broadband, polarization-sensitive photodetector based on optically-thick films of macroscopically long, dense, and aligned carbon nanotubes,” *Sci. Rep.*, vol. 3, pp. 1–7, 2013, DOI: 10.1038/srep01335.

[111] A. O. Goushcha and B. Tabbert, “On response time of semiconductor photodiodes,” *Opt. Eng.*, vol. 56, no. 09, p. 1, 2017, DOI: 10.1117/1.oe.56.9.097101.

[112] K. Czuba *et al.*, “The role of noise in specific detectivity of inas/gasb superlattice mwir bariodes,” *Sensors*, vol. 21, no. 21. 2021, DOI: 10.3390/s21217005.

[113] Z. Bao and X. Chen, “Flexible and Stretchable Devices,” *Adv. Mater.*, vol. 28, no. 22, pp. 4177–4179, 2016, DOI: 10.1002/adma.201601422.

[114] N. Valliappan *et al.*, “Accelerating eye movement research via accurate and affordable smartphone eye tracking,” *Nat. Commun.*, vol. 11, no. 1, p. 4553, 2020, DOI: 10.1038/s41467-020-18360-5.

[115] W. Dai *et al.*, “Giant photothermoelectric effect in silicon nanoribbon photodetectors,” *Light Sci. Appl.*, vol. 9, no. 1, pp. 11–13, 2020, DOI: 10.1038/s41377-020-00364-x.

[116] Y. Niu *et al.*, “Ultrabroadband, Fast, and Flexible Photodetector Based on $HfTe_5$ Crystal,” *Adv. Opt. Mater.*, vol. 2000833, pp. 1–8, 2020, DOI: 10.1002/adom.202000833.

[117] J. Wang *et al.*, “Review—State-of-the-Art Organic Solar Cells based on Carbon Nanotubes and Graphene,” *ECS J. Solid State Sci. Technol.*, vol. 9, no. 10, p. 105004, 2020, DOI: 10.1149/2162-8777/abc3cd.

[118] J. Li *et al.*, “Infrared and THz thermal detection based on an all polymer device,” *Sensors Actuators, A Phys.*, vol. 309, p. 112021, 2020, DOI: 10.1016/j.sna.2020.112021.

[119] G.-H. Kim *et al.*, “Engineered doping of organic semiconductors for enhanced thermoelectric efficiency,” *Nat. Mater.*, vol. 12, no. 8, pp. 719–723, 2013, DOI: 10.1038/nmat3635.

[120] X. Fan *et al.*, “PEDOT:PSS for Flexible and Stretchable Electronics: Modifications, Strategies, and Applications,” *Adv. Sci.*, vol. 6, no. 19, 2019, DOI: 10.1002/advs.201900813.

[121] J. Wang *et al.*, “Two-dimensional materials applied for room-temperature thermoelectric photodetectors,” *Mater. Res. Express*, vol. 7, no. 11, 2020, DOI: 10.1088/2053-1591/abc6cc.

[122] J. H. Kim and T. J. Kang, “Composite films of poly(3,4-ethylenedioxythiophene) polystyrene sulfonate incorporated with carbon nanotube sheet for improved power factor in thermoelectric conversion,” *Mater. Today Commun.*, vol. 25, p. 101568, 2020, DOI: 10.1016/j.mtcomm.2020.101568.

[123] S. Liu *et al.*, “Simultaneous enhancement of electrical conductivity and seebeck coefficient in organic thermoelectric SWNT/PEDOT:PSS nanocomposites,” *Carbon N. Y.*, vol. 149, pp. 25–32, 2019, DOI: 10.1016/j.carbon.2019.04.007.

[124] J. Y. Kim *et al.*, “Wet-spinning and post-treatment of CNT/PEDOT:PSS composites for use in organic fiber-based thermoelectric generators,” *Carbon N. Y.*, vol. 133, pp. 293–299, 2018, DOI: 10.1016/j.carbon.2018.03.041.

[125] S. Wei *et al.*, “SWCNT network evolution of PEDOT:PSS/SWCNT composites for thermoelectric application,” *Chem. Eng. J.*, vol. 428, p. 131137, 2022, DOI:

10.1016/j.cej.2021.131137.

[126] C. Xu *et al.*, “Wet-spun PEDOT:PSS/CNT composite fibers for wearable thermoelectric energy harvesting,” *Compos. Commun.*, vol. 32, p. 101179, 2022, DOI: 10.1016/j.coco.2022.101179.

[127] X. Cao *et al.*, “Thermoelectric PEDOT:PSS Sheet/SWCNTs composites films with layered structure,” *Compos. Commun.*, vol. 27, p. 100869, 2021, DOI: 10.1016/j.coco.2021.100869.

[128] M. R. Watt and R. A. Gerhardt, “Factors that Affect Network Formation in Carbon Nanotube Composites and their Resultant Electrical Properties,” *J. Compos. Sci.*, vol. 4, no. 3, p. 100, 2020, DOI: 10.3390/jcs4030100.

[129] J. Li *et al.*, “On the mechanism of conductivity enhancement in PEDOT/PSS film doped with multi-walled carbon nanotubes,” *J. Polym. Res.*, vol. 17, no. 5, pp. 713–718, 2010, DOI: 10.1007/s10965-009-9360-1.

[130] J. F. Sierra *et al.*, “Hot-Carrier Seebeck Effect: Diffusion and Remote Detection of Hot Carriers in Graphene,” *Nano Lett.*, vol. 15, no. 6, pp. 4000–4005, 2015, DOI: 10.1021/acs.nanolett.5b00922.

[131] A. I. Hochbaum *et al.*, “Enhanced thermoelectric performance of rough silicon nanowires,” *Nature*, vol. 451, no. 7175, pp. 163–167, 2008, DOI: 10.1038/nature06381.

[132] F. H. L. Koppens *et al.*, “Photodetectors based on graphene, other two-dimensional materials and hybrid systems,” *Nat. Nanotechnol.*, vol. 9, no. 10, pp. 780–793, 2014, DOI: 10.1038/nnano.2014.215.

[133] X. Zhao *et al.*, “Evaluation of energy filtering effect from first principles calculations,” *Phys.*

Status Solidi Appl. Mater. Sci., vol. 213, no. 12, pp. 3250–3253, 2016, DOI: 10.1002/pssa.201600546.

[134] D. Narducci *et al.*, "Impact of energy filtering and carrier localization on the thermoelectric properties of granular semiconductors," *J. Solid State Chem.*, vol. 193, pp. 19–25, 2012, DOI: 10.1016/j.jssc.2012.03.032.

[135] G. H. Kim *et al.*, "Thermoelectric properties of nanocomposite thin films prepared with poly(3,4-ethylenedioxythiophene) poly(styrenesulfonate) and graphene," *Phys. Chem. Chem. Phys.*, vol. 14, no. 10, pp. 3530–3536, 2012, DOI: 10.1039/C2CP23517J.

[136] T. Inomata *et al.*, "Clinical and prodromal ocular symptoms in coronavirus disease: A systematic review and meta-analysis," *Investig. Ophthalmol. Vis. Sci.*, vol. 61, no. 10, pp. 1–4, 2020, DOI: 10.1167/IOVS.61.10.29.

[137] I. Rigas *et al.*, "Photosensor Oculography: Survey and Parametric Analysis of Designs Using Model-Based Simulation," *IEEE Trans. Human-Machine Syst.*, vol. 48, no. 6, pp. 670–681, 2018, DOI: 10.1109/THMS.2018.2807244.

[138] K. Sakurai and H. Tamura, "A study on the gaze range calculation method during an actual car driving using eyeball angle and head angle information," *Sensors (Switzerland)*, vol. 19, no. 21, 2019, DOI: 10.3390/s19214774.

[139] S. Matteoli *et al.*, "Ocular surface temperature in patients with evaporative and aqueous-deficient dry eyes: A thermographic approach," *Physiol. Meas.*, vol. 38, no. 8, pp. 1503–1512, 2017, DOI: 10.1088/1361-6579/aa78bd.

[140] F. D. Perez Reynoso *et al.*, "A Custom EOG-Based HMI Using Neural Network Modeling

to Real-Time for the Trajectory Tracking of a Manipulator Robot," *Front. Neurorobot.*, vol. 14, 2020, DOI: 10.3389/fnbot.2020.578834.

[141] X. Zeng *et al.*, "The preparation of a high performance near-infrared shielding Cs_xWO_3/SiO_2 composite resin coating and research on its optical stability under ultraviolet illumination," *J. Mater. Chem. C*, vol. 3, no. 31, pp. 8050–8060, 2015, DOI: 10.1039/C5TC01411E.

[142] S.-M. Jeong *et al.*, "Development of a wearable infrared shield based on a polyurethane–antimony tin oxide composite fiber," *NPG Asia Mater.*, vol. 12, no. 1, p. 32, 2020, DOI: 10.1038/s41427-020-0213-z.

[143] A. Skouroliakou *et al.*, "Infrared Thermography Imaging: Evaluating surface emissivity and skin thermal response to IR heating," *e-Journal Sci. Technol.*, vol. 3, pp. 9–14, Jan. 2014.

[144] E. P. Osuobeni and M. H. Al-Mijalli, "Association between eyelid thickness and corneal astigmatism," *Clin. Exp. Optom.*, vol. 80, no. 1, pp. 35–39, 1997, DOI: 10.1111/j.1444-0938.1997.tb04845.x.

[145] T. Ye *et al.*, "Thin film cracking and the roles of substrate and interface," *Int. J. Solids Struct.*, vol. 29, no. 21, pp. 2639–2648, 1992, DOI: 10.1016/0020-7683(92)90227-K.

[146] D. Li *et al.*, *Recent Progress of Two-Dimensional Thermoelectric Materials*, vol. 12, no. 1. 2020.

[147] W. Shi *et al.*, "Tuning Thermal Transport in Chain-Oriented Conducting Polymers for Enhanced Thermoelectric Efficiency: A Computational Study," *Adv. Funct. Mater.*, vol. 27, no. 40, pp. 1–8, 2017, DOI: 10.1002/adfm.201702847.

[148] V. J. H. *et al.*, “Broadband infrared photodetection using a narrow bandgap conjugated polymer,” *Sci. Adv.*, vol. 7, no. 24, p. eabg2418, 2022, DOI: 10.1126/sciadv.abg2418.

[149] H. Wang *et al.*, “Emerging Single-Photon Detectors Based on Low-Dimensional Materials,” *Small*, vol. 18, no. 5, p. 2103963, 2022, DOI: 10.1002/smll.202103963.

[150] S. Liu *et al.*, “A bioinspired broadband self-powered photodetector based on photo-pyroelectric-thermoelectric effect able to detect human radiation,” *Nano Energy*, vol. 93, p. 106812, 2022, DOI: 10.1016/j.nanoen.2021.106812.

[151] S. Magdi *et al.*, “Broadband MIR harvester using silicon nanostructures,” *Sci. Rep.*, vol. 9, p. 5829, 2019, DOI: 10.1038/s41598-019-42022-2.

[152] Y. Wang *et al.*, “Fast Uncooled Mid-Wavelength Infrared Photodetectors with Heterostructures of van der Waals on Epitaxial HgCdTe,” *Adv. Mater.*, vol. 34, no. 6, p. 2107772, 2022, DOI: 10.1002/adma.202107772.

[153] E. Martínez Castellano *et al.*, “Self-assembled metal-oxide nanoparticles on GaAs: Infrared absorption enabled by localized surface plasmons,” *Nanophotonics*, vol. 10, no. 9, pp. 2509–2518, 2021, DOI: 10.1515/nanoph-2021-0167.

[154] M. Shafa *et al.*, “Flexible infrared photodetector based on indium antimonide nanowire arrays,” *Nanotechnology*, vol. 32, no. 27, 2021, DOI: 10.1088/1361-6528/abe965.

[155] I. Lagraa *et al.*, “Study and optimization of structure InAs/InGaAs quantum dot in-a-well long-wave infrared photodetector,” *Optik (Stuttg).*, vol. 251, 2022, DOI: 10.1016/j.ijleo.2021.168494.

[156] P. Sohr *et al.*, “Strong Coupling in Semiconductor Hyperbolic Metamaterials,” *Nano Lett.*,

vol. 21, no. 23, pp. 9951–9957, 2021, DOI: 10.1021/acs.nanolett.1c03290.

[157] H. B. Kwok and R. H. Bube, “Thermoelectric and photothermoelectric effects in semiconductors: CdS single crystals,” *J. Appl. Phys.*, vol. 44, no. 1, pp. 138–144, 1973, DOI: 10.1063/1.1661848.

[158] J. G. Harper *et al.*, “Two-carrier photothermoelectric effects in GaAs,” *J. Appl. Phys.*, vol. 41, no. 7, pp. 3182–3184, 1970, DOI: 10.1063/1.1659387.

[159] B. Chen *et al.*, “Highly polarization-sensitive far infrared detector based on an optical antenna integrated aligned carbon nanotube film,” *Nanoscale*, vol. 12, no. 22, pp. 11808–11817, 2020, DOI: 10.1039/d0nr01243b.

[160] V. Shautsova *et al.*, “Plasmon induced thermoelectric effect in graphene,” *Nat. Commun.*, vol. 9, no. 1, pp. 1–9, 2018, DOI: 10.1038/s41467-018-07508-z.

[161] D. Suzuki *et al.*, “Terahertz and infrared response assisted by heat localization in nanoporous graphene,” *Carbon N. Y.*, vol. 173, pp. 403–409, 2021, DOI: 10.1016/j.carbon.2020.10.059.

[162] L. Viti *et al*, “Thermoelectric terahertz photodetectors based on selenium-doped black phosphorus flakes,” *Nanoscale*, vol. 11, no. 4, pp. 1995–2002, 2019, DOI: 10.1039/C8NR09060B.

[163] D. Wang *et al.*, “Enhancing the graphene photocurrent using surface plasmons and a p-n junction,” *Light Sci. Appl.*, vol. 9, no. 1, pp. 1–10, 2020, DOI: 10.1038/s41377-020-00344-1.

[164] M. Buscema *et al*, “Fast and broadband photoresponse of few-layer black phosphorus field-

effect transistors," *Nano Lett.*, vol. 14, no. 6, pp. 3347–3352, 2014, DOI: 10.1021/nl5008085.

[165] A. Venkataraman *et al*, "Carbon Nanotube Assembly and Integration for Applications," *Nanoscale Res. Lett.*, vol. 14, no. 1, 2019, DOI: 10.1186/s11671-019-3046-3.

[166] J. Wang *et al*, "Two-dimensional materials applied for room-temperature thermoelectric photodetectors," *Mater. Res. Express*, vol. 7, no. 11, p. 112001, 2020, DOI: 10.1088/2053-1591/abc6cc.

[167] C. Xin *et al.*, "Flexible and wearable plasmonic-enabled organic/inorganic hybrid photothermoelectric generators," *Mater. Today Energy*, vol. 22, 2021, DOI: 10.1016/j.mtener.2021.100859.

[168] Y. Li *et al.*, "A fast response, self-powered and room temperature near infrared-terahertz photodetector based on a $MAPbI_3$/PEDOT:PSS composite," *J. Mater. Chem. C*, vol. 8, no. 35, pp. 12148–12154, 2020, DOI: 10.1039/d0tc02399j.

[169] F. Shahzad *et al.*, "Electromagnetic interference shielding with 2D transition metal carbides (MXenes)," *Science*, vol. 353, no. 6304, pp. 1137–1140, 2016, DOI: 10.1126/science.aag2421.

[170] R. Li *et al*, "MXene Ti_3C_2: An Effective 2D Light-to-Heat Conversion Material," *ACS Nano*, vol. 11, no. 4, pp. 3752–3759, 2017, DOI: 10.1021/acsnano.6b08415.

[171] X. Guan *et al.*, "Significant Enhancement in the Seebeck Coefficient and Power Factor of p-Type Poly(3,4-ethylenedioxythiophene):Poly(styrenesulfonate) through the Incorporation of n-Type MXene," *ACS Appl. Mater. Interfaces*, vol. 12, no. 11, pp. 13013–

13020, 2020, DOI: 10.1021/acsami.9b21185.

[172] P. D. Keathley *et al.*, “Vanishing carrier-envelope-phase-sensitive response in optical-field photoemission from plasmonic nanoantennas,” *Nat. Phys.*, vol. 15, no. 11, pp. 1128–1133, 2019, DOI: 10.1038/s41567-019-0613-6.

[173] N. Tajima *et al.*, “Stress control in optical thin films by sputtering and electron beam evaporation,” *Appl. Opt.*, vol. 56, no. 4, pp. C131–C135, 2017, DOI: 10.1364/AO.56.00C131.

[174] J. Cai *et al.*, “Indirect Virus Transmission in Cluster of COVID-19 Cases, Wenzhou, China, 2020,” *Emerg. Infect. Dis. J.*, vol. 26, no. 6, p. 1343, 2020, DOI: 10.3201/eid2606.200412.

[175] M. Dai *et al.*, “On-chip mid-infrared photothermoelectric detectors for full-Stokes detection,” *Nat. Commun.*, vol. 13, no. 1, 2022, p. 4560, DOI: 10.1038/s41467-022-32309-w.

[176] X. Du and K. Zhang, “Recent progress in fibrous high-entropy energy harvesting devices for wearable applications,” *Nano Energy*, vol. 101, p. 107600, 2022, DOI: 10.1016/j.nanoen.2022.107600.

[177] D. Kireev *et al.*, “Continuous cuffless monitoring of arterial blood pressure via graphene bioimpedance tattoos,” *Nat. Nanotechnol.*, vol. 17, no. 8, pp. 864–870, 2022, DOI: 10.1038/s41565-022-01145-w.

[178] S. Gehr *et al.*, “Shaping the future of cardiovascular medicine in the new era of wearable devices,” *Nat. Rev. Cardiol.*, vol. 19, no. 8, pp. 501–502, 2022, DOI: 10.1038/s41569-022-00729-2.

[179] D. A. Bandurin *et al.*, "Cyclotron resonance overtones and near-field magnetoabsorption via terahertz Bernstein modes in graphene," *Nat. Phys.*, vol. 18, no. 4, pp. 462–467, 2022, DOI: 10.1038/s41567-021-01494-8.

[180] W. Lu *et al.*, "Ultrafast photothermoelectric effect in Dirac semimetallic Cd_3As_2 revealed by terahertz emission," *Nat. Commun.*, vol. 13, no. 1, p. 1623, 2022, DOI: 10.1038/s41467-022-29168-w.

[181] Y. Cao *et al.*, "Ultra-Broadband Photodetector for the Visible to Terahertz Range by Self-Assembling Reduced Graphene Oxide-Silicon Nanowire Array Heterojunctions," *Small*, vol. 10, no. 12, pp. 2345–2351, Jun. 2014, DOI: 10.1002/smll.201303339.

[182] J. Li *et al.*, "Enhanced room-temperature terahertz detection and imaging derived from anti-reflection 2D perovskite layer on $MAPbI_3$ single crystals," *Nanoscale*, vol. 14, no. 16, pp. 6109–6117, 2022, DOI: 10.1039/d2nr00497f.

[183] M. Ghidiu *et al.*, "Conductive two-dimensional titanium carbide 'clay' with high volumetric capacitance," *Nature*, vol. 516, no. 7529, pp. 78–81, 2015, DOI: 10.1038/nature13970.

[184] T. Tan *et al.*, "2D Material Optoelectronics for Information Functional Device Applications: Status and Challenges," *Adv. Sci.*, vol. 7, no. 11, 2020, DOI: 10.1002/advs.202000058.

[185] A. Sarycheva *et al.*, "2D titanium carbide (MXene) for wireless communication," *Sci. Adv.*, vol. 4, no. 9, pp. 1–9, 2018, DOI: 10.1126/sciadv.aau0920.

[186] W. Tian *et al.*, "Layer-by-layer self-assembly of pillared two-dimensional multilayers," *Nat. Commun.*, vol. 10, no. 1, pp. 1–10, 2019, DOI: 10.1038/s41467-019-10631-0.

[187] J. Jeon *et al.*, "MXenes for future nanophotonic device applications," *Nanophotonics*, vol.

9, no. 7, pp. 1831–1853, 2020, DOI: 10.1515/nanoph-2020-0060.

[188] L. Li *et al.*, “Flexible $Ti_3C_2T_x$/PEDOT:PSS films with outstanding volumetric capacitance for asymmetric supercapacitors,” *Dalt. Trans.*, vol. 48, no. 5, pp. 1747–1756, 2019, DOI: 10.1039/c8dt04374d.

[189] H. Kim *et al.*, “Thermoelectric Properties of Two-Dimensional Molybdenum-Based MXenes,” *Chem. Mater.*, vol. 29, no. 15, pp. 6472–6479, 2017, DOI: 10.1021/acs.chemmater.7b02056.

[190] T. J. Echtermeyer *et al.*, “Photothermoelectric and photoelectric contributions to light detection in metal-graphene-metal photodetectors,” *Nano Lett.*, vol. 14, no. 7, pp. 3733–3742, 2014, DOI: 10.1021/nl5004762.

[191] J. Wang *et al.*, “Design of room-temperature infrared photothermoelectric detectors based on CNT/PEDOT:PSS composites,” *J. Mater. Chem. C*, vol. 10, pp. 15105-15113, 2022, DOI: 10.1039/d2tc03159k.

[192] A. Szabó *et al.*, “Growth of CNT Forests on Titanium Based Layers, Detailed Study of Catalysts,” *Frontiers in Chemistry*, vol. 6. 2018, DOI: 10.3389/fchem.2018.00593.

[193] S. Seyedin *et al.*, “Facile Solution Processing of Stable MXene Dispersions towards Conductive Composite Fibers,” *Glob. Challenges*, vol. 3, no. 10, p. 1900037, 2019, DOI: 10.1002/gch2.201900037.

[194] V. Jourdain and C. Bichara, “Current understanding of the growth of carbon nanotubes in catalytic chemical vapour deposition,” *Carbon N. Y.*, vol. 58, pp. 2–39, 2013, DOI: 10.1016/j.carbon.2013.02.046.

[195] J. Liu *et al.*, “Carbon nanotubes for electronics manufacturing and packaging: From growth to integration,” *Adv. Manuf.*, vol. 1, no. 1, pp. 13–27, 2013, DOI: 10.1007/s40436-013-0007-4.

[196] A. M. S. Galante *et al.*, “Study on application of PTFE, FEP and PFA fluoropolymers on radiation dosimetry,” *Nucl. Instruments Methods Phys. Res. Sect. A Accel. Spectrometers, Detect. Assoc. Equip.*, vol. 619, no. 1, pp. 177–180, 2010, DOI: 10.1016/j.nima.2009.10.103.

[197] J.-Y. Park *et al.*, “Fabrication of polytetrafluoroethylene nanofibrous membranes for guided bone regeneration,” *RSC Adv.*, vol. 8, no. 60, pp. 34359–34369, 2018, DOI: 10.1039/C8RA05637D.

[198] A. Iqbal *et al.*, “Improving oxidation stability of 2D MXenes: synthesis, storage media, and conditions,” *Nano Converg.*, vol. 8, no. 1, p. 9, 2021, DOI: 10.1186/s40580-021-00259-6.

[199] S. Nanot *et al.*, “Broadband, Polarization-Sensitive Photodetector Based on Optically-Thick Films of Macroscopically Long, Dense and Aligned Carbon Nanotubes,” *Sci. Rep.*, vol. 3, no. 1, p. 1335, 2013, DOI: 10.1038/srep01335.